

# PERFORMANCE ENHANCEMENT OF SWITCHED RELUCTANCE MOTOR DRIVE USING DIRECT TORQUE CONTROL STRATEGIES

Thesis

Submitted in partial fulfillment of the requirement for the award of degree of  
DOCTOR OF PHILOSOPHY

by  
PITTAM KRISHNA REDDY



DEPARTMENT OF ELECTRICAL AND ELECTRONICS ENGINEERING,  
NATIONAL INSTITUTE OF TECHNOLOGY KARNATAKA,  
SURATHKAL, MANGALORE - 575025

March, 2023

# DECLARATION

*by the Ph.D. Research Scholar*

I hereby *declare* that the Research Thesis entitled “**Performance Enhancement of Switched Reluctance Motor Drive using Direct Torque Control Strategies**” which is being submitted to the **National Institute of Technology Karnataka, Surathkal** in partial fulfillment of the requirement for the award of the Degree of **Doctor of Philosophy** in **Department of Electrical and Electronics Engineering** is a *bonafide report of the research work carried out by me*. The material contained in this Research Thesis has not been submitted to any University or Institution for the award of any degree.



.....  
Pittam Krishna Reddy, 177122EE010

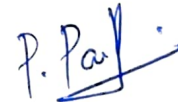
Department of Electrical and Electronics Engineering

Place: NITK-Surathkal

Date: 13-03-2023

## CERTIFICATE

This is to *certify* that the Research Thesis entitled “**Performance Enhancement of Switched Reluctance Motor Drive using Direct Torque Control Strategies** ” submitted by Pittam Krishna Reddy (Register Number: 177122EE010) as the record of the research work carried out by him, is *accepted as the Research Thesis submission* in partial fulfillment of the requirements for the award of degree of **Doctor of Philosophy**.



Dr. P. Parthiban  
(Research Guide)



Dr. D. N. Gaonkar  
(Chairman DRPC, E & E dept.)  
13/3/2023  
ASSOC. PROFESSOR & HEAD  
DEPT. OF ELECTRICAL & ELECTRONICS ENGINEERING  
NATIONAL INSTITUTE OF TECHNOLOGY KARNATAKA  
SURATHKAL SRINIVASNAGAR P.O., MANGALORE-575025

# ACKNOWLEDGEMENTS

It gives me immense pleasure and great sense of satisfaction to express my heartfelt gratitude to those who made this dissertation possible.

I would like to express my sincere gratitude to Dr. P. Parthiban for his guidance, unending support, encouragement, and for having been my Ph.D. supervisor. He has been a constant source of inspiration throughout this journey. I feel proud to have worked under his guidance.

I thank National Institute of Technology Karnataka (NITK) for giving me an opportunity for doing research and Ministry of Human Resource Department-Government of India for awarding research scholarship.

I wish to thank my research progress assessment committee (RPAC) members Dr. Nagendrappa H, and Dr. Biju R. Mohan for their constructive feedback and guidance.

I am grateful to Prof. B. Venkatesaperumal, Prof. Shubhanga K N, Prof. G. S. Punekar former HODs and Dr. D. N. Gaonkar, HOD of EEE department for providing the necessary facilities in the department to carry out my research.

I sincerely thank to Dr. Deepak Ronanki, IIT Roorkee for his continuous guidance, support and being part of my research works.

I sincerely thank to Dr. Apparao Dekka, Dr. Abdul R. Beig, Prof. Sheldon S. Williamson for supporting and being part of my research works.

A very special gratitude goes to all other teaching and non teaching staff in the Department of E & E, for their immense support and help.

Without my friends in and out of NITK Surathkal, life would have been dull. I am indebted to all of them for their support, valuable inputs and constant encouragement.

I would like to express my deepest gratitude towards my family members for their love and patience which kept me going in this journey. Their faith and unconditional love towards me are the reason for whatever I have achieved in my life.

Finally, I thank God Almighty for giving me strength at all times.



# Abstract

Due to rare earth permanent magnets (PM) price volatility, there is a significant interest in developing magnet free motor drive configurations that are more efficient, highly dense and ruggedness to the harsh environment in electrified vehicles. Switched reluctance motor (SRM) is considered to be one of the promising alternatives to the traditional AC motors due to distinctive features of the robust structure, high starting torque, wide constant power region, no shoot-through current in the inverter, low cost and low maintenance. However, it suffers from severe torque ripple, acoustic noise and the requirement of a position sensor for control, which limits the wide usage of SRM in vehicular applications. Moreover, smooth torque control is difficult to achieve due to inherent torque pulsations generated due to the doubly salient structure.

Over the past years, significant research is carried out to minimize the aforementioned concerns in SRM by improving the design aspects of the motor and/or employing appropriate control strategies. Most of the work related to the motor design is devoted to optimizing machine parameters and developing the multi-phase machines. Later one is achieved by developing advanced optimized control techniques such as current profiling techniques (CPT), and torque sharing functions (TSF), where the torque is an indirect control variable. However, these approaches require intensive computation to store machine non-linear characteristics, long settling time and require optimal tuning of control parameters.

Alternatively, controlling torque as a direct control variable led to overcome some of the aforementioned shortcomings through direct instantaneous torque control (DITC), advanced DITC, direct torque and flux control (DTFC) and model predictive control strategies. The performance comparison of different control strategies such as CPT, TSF, DITC, and DTFC is studied and the merits and demerits of each method are well established in the literature. Among them, the DTFC scheme which utilizes the philosophy of direct torque control (DTC) of conventional AC machines draws more attention due to automatic control, reduced acoustic noise, fast dynamic response, insensitive to motor parameters & does not require rotor position information. In this scheme, the phase torque is directly controlled by accelerating or decelerating the flux

linkage vector, where the magnitude of flux linkage is kept constant within a hysteresis band. However, the active phase has to produce higher positive torque during commutation of outgoing phase, thereby draws higher source current. As a result, there is a reduction in overall torque per ampere, thereby reducing the efficiency of the traction drives.

In the present thesis, two new DTC algorithms are proposed with optimized voltage vector selection and appropriate sector partition based on the inductance profile to enhance torque/ampere ratio (T/A) and minimize torque ripple in four-phase (8/6) SRM. A 16 sixteen sector approach is developed to select the vectors more precisely, thereby effectively eliminates the existence of phase current in the zero torque region which leads to increase in T/A and torque ripple minimization. However, negative phase torque is still generated in this method due to existence of phase current in negative inductance slope region. To overcome this issue, a 16 sector 16 vector DTC algorithm is proposed. MATLAB simulations and real time simulations with OPAL-RT are performed to verify the effectiveness of the proposed DTC algorithms in terms of torque ripple, T/A and source current ripple. Moreover, copper losses, switching losses and number of commutations required for one cycle are calculated to show the efficacy of the proposed algorithm over conventional DTC algorithm. In general, four phase SRM requires four current sensors to measure phase currents that increases the cost of the drive. To overcome this issue, a new phase current reconstruction algorithm is developed to detect the four phase currents more accurately using only three sensors under proposed DTC algorithm.

# Contents

<b>Abstract</b>	i
<b>Table of Contents</b>	iii
<b>List of Figures</b>	vii
<b>List of Tables</b>	xi
<b>List of Abbreviations</b>	xii
<b>List of Symbols</b>	xiv
<b>1 Introduction</b>	1
<b>1.1 Switched Reluctance Motor</b>	2
<b>1.1.1 Construction of Four-Phase SRM</b>	2
<b>1.1.2 Derivation of the Relationship between Inductance and Rotor Position</b>	3
<b>1.1.3 Speed-Torque Characteristics</b>	5
<b>1.2 Torque Ripple in SRM</b>	6
<b>1.2.1 The Origin of Torque Ripple</b>	6
<b>1.2.2 Design Effects on Torque Ripple</b>	7
<b>1.2.3 Importance of Torque Ripple</b>	7
<b>1.2.4 Possible Ways to Torque Ripple Minimization</b>	7
<b>1.2.5 Basic Control of SRM for Torque Ripple Minimization</b>	8
<b>1.3 Literature on Torque Ripple Minimization for SRM</b>	8
<b>1.3.1 Torque Ripple Minimization with Improvements in Motor Design</b>	8
<b>1.3.2 Commutation Angle Optimization and Current Control Methods for Torque Ripple Minimization</b>	9
<b>1.3.3 Torque Ripple Minimization with Torque Sharing Functions (TSF)</b>	9
<b>1.4 Literature on Direct Torque Control for SRM</b>	12
<b>1.5 Literature on Phase Current Reconstruction Algorithms for SRM</b>	12
<b>1.6 Motivation in the Present Work</b>	14



1.7	Research Objectives	14
1.8	Thesis Organization	15
<b>2</b>	<b>Direct Torque Control of Switched Reluctance Motor Drive</b>	<b>19</b>
2.1	Introduction	19
2.2	Dynamic Modeling of Four-Phase SRM	19
2.2.1	Experimental Determination of Magnetization & Static Torque Characteristics	19
2.2.2	Flux Linkage and Torque Characteristics	21
2.2.3	Mathematical Modeling of Four Phase SRM	22
2.3	Asymmetrical Half-Bridge Converter (AHBC)	23
2.4	Direct Torque Control (DTC)	24
2.4.1	Conventional Direct Torque Control of Four-Phase SRM	25
2.4.2	Sector Partition & Selection of Voltage Vectors	26
2.4.3	Simulation Results of Conventional DTC	28
2.5	Summary	31
<b>3</b>	<b>Proposed Direct Torque Control Algorithms</b>	<b>33</b>
3.1	Introduction	33
3.2	Proposed DTC - 8 Vector 16 Sector Partition Method	33
3.2.1	Simulation Results	35
3.3	Proposed DTC - 16 Vectors 16 Sectors Partition Method	39
3.3.1	Simulation Results	43
3.3.2	Real Time Simulations with OPAL-RT	48
3.4	Performance Analysis of DTC Schemes	49
3.4.1	Torque Ripple Analysis	49
3.4.2	T/A and Copper Loss	49
3.4.3	Current Stress on Power Devices and the Number of Commutations	50
3.4.4	Power Loss Analysis	53
3.4.5	Input Power Fluctuations	56
3.4.6	Comparison Summary of the Proposed DTC Scheme with Conventional DTC	57
3.5	Summary	58
<b>4</b>	<b>Proposed Phase Current Reconstruction Algorithm</b>	<b>59</b>
4.1	Introduction	59
4.2	Phase Current Reconstruction Methods	60

4.2.1	Phase Current Reconstruction from DC-Link Current using High-Frequency Pulse Injection	60
4.2.2	Split Dual Bus Method for Phase Current Detection	63
4.2.3	Phase Current Reconstruction using Improved Converter Topology	65
4.2.4	Multiplexed Current Sensors Based Phase Current Detection Scheme	66
4.3	Proposed Phase Current Reconstruction Algorithm	67
4.4	Results and Discussions	70
4.5	Real-Time Validation	74
4.6	Summary	76
<b>5</b>	<b>Hardware Implementation of Hysteresis Current Control for Four-Phase SRM Drive</b>	<b>77</b>
5.1	Introduction	77
5.2	Phase Inductance Profile Relative to position Sensor Output	77
5.3	Hardware Implementation	79
5.3.1	Voltage Control Algorithm	79
5.3.2	Hysteresis Current Control Algorithm	81
5.4	Summary	82
<b>6</b>	<b>Conclusion &amp; Future Scope</b>	<b>85</b>
6.1	Conclusion	85
6.2	Research Contributions of the Thesis	87
6.3	Future Scope	87
<b>A</b>	<b>Software Details</b>	<b>89</b>
A.1	STM32 Microcontroller Pin Configuration using CUBEMX Software	89
A.2	Embedded Code Development using Keil $\mu$ Vision Software	90
<b>B</b>	<b>Hardware Specifications</b>	<b>91</b>
B.1	Specification of SRM	91
B.2	Specification of Eddy Current Brake	91
B.3	Specification of Rectifier and Asymmetric H- Bridge Converter	92
B.4	Specification of Power Supplies	93
B.5	Specification of ARM Cortex M4 32-bit Microcontroller Development Board	94
B.6	Specification of Voltage and Current Sensor Boards	95
B.7	Specification of DSO Tektronix TPS 2024B	97
	<b>Bibliography</b>	<b>103</b>

**List of Publications Based on Research Work**

105

# List of Figures

1.1	Cross sectional view of four-phase (8/6) SRM	3
1.2	Basic rotor position definition in a two pole SRM	4
1.3	Inductance profile	4
1.4	Speed-torque characteristics of SRM.	6
1.5	Hysteresis current control and single pulse operation of SRM	8
1.6	Typical TSF profile for a three-phase SRM	10
1.7	Thesis organization	17
2.1	Block diagram of experimental setup for determination of magnetization and static torque characteristics	20
2.2	SRM characteristics plotted from experimental data (a) Flux-linkage characteristics, (b) Torque characteristics	21
2.3	Phase model of SRM	23
2.4	Four phase model of SRM	23
2.5	Asymmetric half-bridge converter (AHBC)	24
2.6	Modes of operation of AHBC	24
2.7	DTC block diagram of SRM	26
2.8	Definition of voltage vectors and partition of sectors for conventional DTC	27
2.9	Simulation results of electromagnetic torque $T_{em}$ , phase currents $i_a, i_b, i_c$ and $i_d$ , phase torques $T_a, T_b, T_c$ and $T_d$ , and sectors for conventional DTC at N = 500 rpm	29
2.10	Simulation results of phase voltage $V_a$ , phase current $i_a$ and corresponding gate signals of $S_1, S_2$ for Conventional DTC at N = 500 rpm	30
2.11	Interpretation of zero and negative torque regions in conventional DTC	31
3.1	Definition of voltage vectors and partition of sectors for proposed 16-sector 8-vector DTC	34

3.2	Simulation results of electromagnetic torque $T_{em}$ , phase currents $i_a, i_b, i_c$ and $i_d$ , phase torques $T_a, T_b, T_c$ and $T_d$ , and sectors for proposed 16-sector 8-vector DTC at N = 500 rpm	35
3.3	Simulation results of the phase voltage $V_a$ , phase current $i_a$ and the gate signals of $S_1, S_2$ for proposed DTC at N = 500 rpm	36
3.4	Interpretation of zero and negative torque regions in proposed DTC	36
3.5	Dynamic response comparison of conventional DTC and proposed DTC	37
3.6	Results at 500 rpm (a) Conventional DTC, (b) Proposed 8-vector 16-sector DTC. <b>Scope i:</b> CH1: Torque (Nm) and CH2: Sector number; <b>Scope ii:</b> CH1:Phase-A current (A) and CH2: Flux linkage; <b>Scope iii:</b> CH1: Gate signal for $S_1$ and CH2: Gate signal for $S_2$	38
3.7	Definition of voltage vectors and partition of sectors for proposed 16 vector 16 sector DTC (a) Torque increasing condition, (b) Torque decreasing condition	40
3.8	Flowchart of the conventional DTC	41
3.9	Flowchart of the proposed 16 vector 16 sector DTC	42
3.10	Steady-state simulation results of phase voltages $V_a$ & $V_c$ , phase currents $i_a$ & $i_c$ , phase torques $T_a$ & $T_c$ , and total electromagnetic torque $T_{em}$ for conventional DTC at 250 rpm	43
3.11	Steady-state simulation results of phase voltages $V_a$ & $V_c$ , phase currents $i_a$ & $i_c$ , phase torques $T_a$ & $T_c$ , and total electromagnetic torque $T_{em}$ for conventional DTC at 750 rpm	44
3.12	Steady-state simulation results of phase voltages $V_a$ & $V_c$ , phase currents $i_a$ & $i_c$ , phase torques $T_a$ & $T_c$ , and total electromagnetic torque $T_{em}$ for proposed 16 vector 16 sector DTC at 250 rpm	45
3.13	Steady-state simulation results of phase voltages $V_a$ & $V_c$ , phase currents $i_a$ & $i_c$ , phase torques $T_a$ & $T_c$ , and total electromagnetic torque $T_{em}$ for proposed 16 vector 16 sector DTC at 750 rpm	46
3.14	Dynamic performance of conventional DTC at 750 rpm	47
3.15	Dynamic performance of proposed DTC at 750 rpm	48
3.16	Real-time results at 750 rpm (a) Conventional DTC, (b) Proposed DTC : <b>Scope i:</b> CH1: Total torque (Nm), CH2: Sector number, CH3: Phase torque (Nm) and CH4: Phase current (A); <b>Scope ii:</b> CH1: Phase current (A), CH2: Phase voltage (V), CH3: Gate signal for $S_1$ and CH4: Gate signal $S_2$ .	49

3.17 Comparison of per-phase copper losses under the conventional and proposed DTC schemes . . . . .	50
3.18 Device stress under the conventional DTC scheme . . . . .	51
3.19 Device stress under the proposed DTC scheme . . . . .	52
3.20 Block diagram for evaluating the number of commutations . . . . .	52
3.21 Converter power loss analysis (a) Conventional DTC at 250 rpm, (b) Proposed DTC at 250 rpm . . . . .	55
3.22 Converter power loss analysis (a) Conventional DTC at 750 rpm, (b) Proposed DTC at 750 rpm . . . . .	55
3.23 Block diagram of power loss evaluation methodology (a) Conduction losses, (b) Switching losses, (c) Total losses . . . . .	56
3.24 Comparison of source current at 250 rpm (a) Conventional DTC, (b) Proposed DTC . . . . .	57
4.1 Conventional current measurement scheme with individual hall-effect sensors . . . . .	59
4.2 Single sensor based phase current measurement scheme . . . . .	60
4.3 Two phase currents non overlap in the turn-on region . . . . .	61
4.4 Two phase currents overlap in the turn-on region . . . . .	62
4.5 Two sensor based current measurement scheme with split dual bus line . . . . .	63
4.6 Single sensor based phase current measurement system with improved converter topology . . . . .	65
4.7 Multiplexed current detection scheme for four-phase SRM . . . . .	66
4.8 Two phase currents overlap in the turn-on region . . . . .	66
4.9 Block diagram of proposed phase current reconstruction algorithm . . . . .	68
4.10 Illustration of phase currents overlap in (a) Conventional DTC, (b) Proposed DTC . . . . .	69
4.11 Flowchart of the proposed phase current reconstruction algorithm. . . . .	70
4.12 Actual phase currents $i_a$ , $i_b$ , $i_c$ , and $i_d$ measured by sensor per phase at 750 rpm . . . . .	71
4.13 Sensor currents $I_{CS1}$ , $I_{CS2}$ , and $I_{CS3}$ at 750 rpm . . . . .	72
4.14 Reconstructed phase currents $i_{a.re}$ , $i_{b.re}$ , $i_{c.re}$ , and $i_{d.re}$ at 750 rpm . . . . .	73
4.15 Actual phase current $i_a$ , reconstructed current $i_{a.re}$ and error at 750 rpm . . . . .	74
4.16 Phase currents vs. sectors: (a) Phases B & D, (b) Phases A & C . . . . .	75

4.17 Test results of the proposed current reconstruction scheme: (a)	
Actual phase current $i_a$ , reconstructed phase current $i_{a,re}$ and	
error at 750 rpm, (b) Sensor currents $I_{CS1}$ , $I_{CS2}$ , and $I_{CS3}$ and	
corresponding reconstructed phase current $i_{a,re}$ . . . . .	75
4.18 Test results of actual phase current $i_a$ , reconstructed phase current	
$i_{a,re}$ and error at dynamic conditions during: (a) Acceleration, (b)	
Deceleration . . . . .	76
5.1 Rotor position sensor signals . . . . .	78
5.2 Phase inductance profile at eight different regions in one electric	
cycle. . . . .	78
5.3 Block diagram of voltage control implementation . . . . .	79
5.4 Experimental system of 2.2 kW SRM drive . . . . .	80
5.5 Voltage control : (a) No-load at 500 rpm, (b) No-load at 2000 rpm,	
and (c) 1000 rpm at 2 Nm load. . . . .	80
5.6 Block diagram of hysteresis current control implementation . . . . .	81
5.7 Hysteresis current control: (a) Hysteresis current control at $i_{ref} =$	
8A, (b) Phase currents at 10 kHz timer interrupt rate. . . . .	82

# List of Tables

1.1 Comparison of existing phase current reconstruction schemes . . . . .	14
2.1 Operating modes of AHBC . . . . .	24
2.2 Voltage vector selection for conventional DTC . . . . .	27
2.3 Specifications of four phase SRM . . . . .	28
3.1 Voltage vector selection for proposed 8 vector 16 sector DTC method	34
3.2 Comparison of conventional & proposed 8 vector 16 sector DTC methods . . . . .	38
3.3 Voltage vector selection for proposed 16 vector 16 sector DTC method	40
3.4 Comparison of conventional & proposed 16 vectors 16 sectors DTC methods . . . . .	58
3.5 Summary of comparative analysis of proposed and conventional DTC scheme . . . . .	58
4.1 Relationship between dc-link current and switching states . . . . .	62
4.2 Relationship between bus currents and switching states . . . . .	64
4.3 Relationship between sensor currents and phase currents . . . . .	67
4.4 Current sensor outputs corresponding to regions . . . . .	68
5.1 Voltage vs. speed for voltage control method . . . . .	81





# List of Abbreviations

PM	Permanent Magnet
IMs	Induction Machines
SRM	Switched Reluctance Motor
DZ	Dead Zone
EMF	Electro Motive Force
FEM	Finite Element Method
PWM	Pulse Width Modulation
TSF	Torque Sharing Function
DTC	Direct Torque Control
CPT	Current Profiling Techniques
DITC	Direct Instantaneous Torque Control
CCC	Current Chopping Control
DTFC	Direct Torque and Flux Control
FEA	Finite Element Analysis
AC	Alternating Current
DC	Direct Current
T/A	Torque/Ampere
MATLAB	Matrix Laboratory
AHBC	Asymmetrical Half Bridge Converter
DSO	Digital Signal Oscilloscope
IGBT	Insulated Gate Bipolar Transistor
GPIO	General Purpose Input Output
ADC	Analog to Digital Converter



# List of Symbols

$\tau$	Rotor pole pitch
$P_r$	Number of rotor poles
$P_s$	Number of stator poles
$\beta_s$	Stator pole arc
$\beta_r$	Rotor pole arc
$L_u$	Unaligned inductance
$L_a$	Aligned inductance
$\omega_b$	Base speed
$T_{\text{ripple}}$	Torque ripple
$T_{\text{max}}$	Maximum value of torque
$T_{\text{min}}$	Minimum value of torque
$T_{\text{avg}}$	Average value of torque
$T-i-\theta$	Torque-current-angle characteristics
$\theta_{on}$	Turn-on angle
$\theta_{off}$	Turn-off angle
$\theta_{ov}$	Overlap angle
$T_{\text{ref}}$	Reference torque
$R$	Phase winding resistance
$W_c$	Co-energy
$T_L$	Load torque
$B$	Frictional coefficient
$J$	Rotational inertia
$P_c$	Copper losses
$i_{rms}$	RMS value of phase current
$t_{on}$	Turn-on time
$t_{off}$	Turn-off time
$\psi$	Flux linkage



# Chapter 1

## Introduction

Induction and permanent magnet (PM) machines are ruling the motor drive systems in industrial, residential and transportation applications( [Bilgin and Emadi, 2014]). The self starting ability, low-cost manufacturing and matured control technology are the exceptional advantages for induction machines (IMs). IMs are very commonly used in variable speed drive applications with the emerge of power electronics and advanced control technology. In IMs, the rotor excitation current is drawn from the stator, thereby results in low-power factor, the losses involves in the rotor bars reduces the efficiency. However, careful design and optimised control are required to reduce losses to attain better efficiency. The heat dissipation due to the rotor copper losses is a significant issue in IMs. Alternatively PM machines are popular for the applications which demands higher efficiency at low and medium speed range. PM provides the higher torque density due to strong magnetic field by use of rare-earth magnets. Moreover, the temperature dependence of PM is the key disadvantage of PM machines.

Due to rare earth PMs price volatility, there is a significant interest in developing magnet free motor drives that are more efficient, highly dense and ruggedness to the harsh environment conditions. Switched reluctance motor (SRM) is considered to be one of the promising alternatives to the traditional motors due to distinctive features of the robust structure, high starting torque, wide constant power region, no shoot-through current in the inverter, low cost and low maintenance.

The simple and low cost construction due to lack of PMs or windings on the rotor makes the SRM, a potential candidate for variable speed drive applications over PMs and IMs. SRM is more reliable at high speed and high temperature operation due to absence of rotor excitation ( [Bilgin et al., 2018]). Supply chain

issues and environment concerns of rare-earth magnets involved in PM machines become a long run problem in producing high efficiency motors. However, absence of rare-earth magnets in SRM become advantage in this aspect. Rotor displacement and rotational stress, limits the performance of PM motor at high speed operation due to excessive centrifugal forces, which develops the stress in magnet slots and bridges. Therefore, lack of slots and bridges in the rotor makes the SRM better candidate for high speed operation. The field weakening of PMs deteriorates the performance, where as in SRM, field weakening is a natural phenomenon at high speed. Moreover, SRM has wide constant power-speed range compared with PMs and IMs. IMs suffer from rotor copper losses due to the use of die-casting aluminum for rotor conductors that limits the high temperature operation, usually copper die-casting is used at high temperature that involves expensive and challenging manufacturing process. Moreover, the independent torque production capability of each phase due to electrical isolation of each phase acquires the fault tolerant nature to the SRM. In spite of all these advantages, SRM suffers from high torque ripple, noise and vibration. The comparative study of IM, PM machines and SRM is addressed in ( [Yang et al., 2015](#) ). The opportunities and challenges for SRM to vehicular application is presented in ( [Bostanci et al., 2017](#) ).

## 1.1 Switched Reluctance Motor

SRM is an electric motor in which torque is produced by the tendency of its movable part to move to a position where the inductance of the excited winding is maximized.

### 1.1.1 Construction of Four-Phase SRM

The SRM has a simplest, lowest cost, and most robust structure. The SRM stator is made up of a salient pole laminations core with concentrated windings, while the rotor also has a salient pole structure, but without windings or PMs.

The torque produced in SRM is reluctance torque. Due to the salient pole structure, the air gap length varies according to the relative position of rotor and stator poles. This results in varying inductance values in different rotor positions ( [Krishnan, 2017](#) ). The salient stator and rotor structure bring some advantages and also challenges in SRM drives. The cross sectional view of four-phase (8/6) SRM with 8 stator poles and 6 rotor poles is shown in Figure [1.1](#).

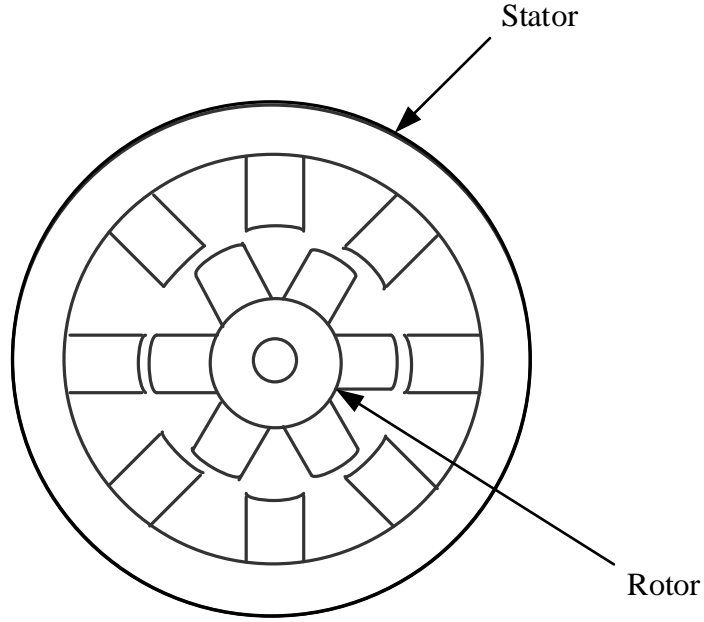


Figure 1.1: Cross sectional view of four-phase (8/6) SRM

### 1.1.2 Derivation of the Relationship between Inductance and Rotor Position

The basic rotor position definition is shown in Figure 1.2 and the corresponding phase inductance vs. rotor position for fixed current is shown in Figure 1.3. These curves are periodic in nature with a period of one rotor pole pitch ( $\tau$ ). If  $P_r$  is the number of rotor poles, the rotor pole pitch for SRM is given as

$$\tau = \frac{2\pi}{P_r} \quad (1.1)$$

The significant inductance profile changes are determined in terms of stator and rotor pole arcs and number of rotor poles. The rotor pole arc is considered to be greater than stator pole arc in this illustration shown in Figure 1.2.



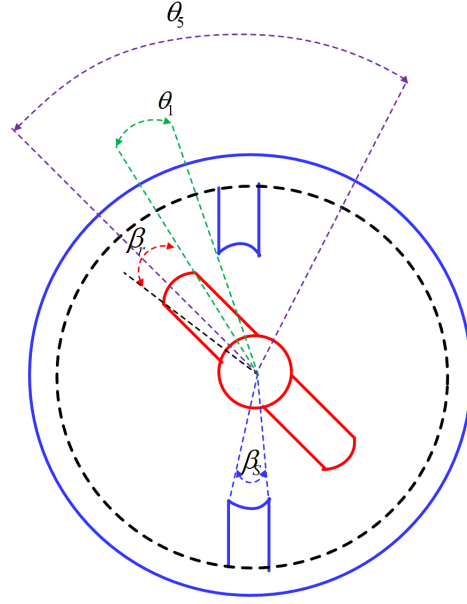


Figure 1.2: Basic rotor position definition in a two pole SRM

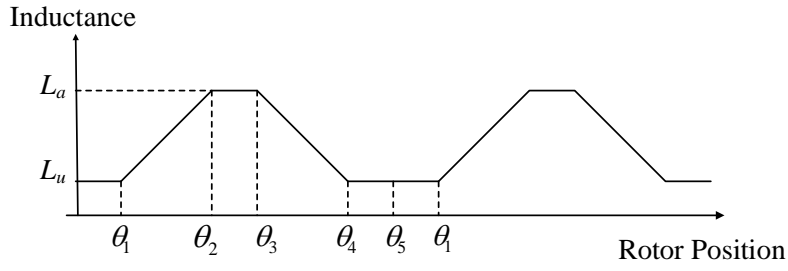


Figure 1.3: Inductance profile

$$\theta_1 = \frac{1}{2} \left[ \frac{2\pi}{P_r} - (\beta_s + \beta_r) \right] \quad (1.2)$$

$$\theta_2 = \theta_1 + \beta_s \quad (1.3)$$

$$\theta_3 = \theta_2 + (\beta_r - \beta_s) \quad (1.4)$$

$$\theta_4 = \theta_3 + \beta_s \quad (1.5)$$

$$\theta_5 = \frac{2\pi}{P_r} \quad (1.6)$$

Where  $\beta_s$  and  $\beta_r$  are the stator and rotor pole arcs.

The torque equation of SRM is given as

$$T = \frac{1}{2}i^2 \frac{dL}{d\theta} \quad (1.7)$$

The regions ‘0 -  $\theta_1$ ’ and ‘ $\theta_4$  -  $\theta_5$ ’ do not contribute any torque as the phase winding inductance is constant because stator and rotor poles are not overlapping. The inductance in this region is known as unaligned inductance  $L_u$ . The inductance increases with the positive slope in the region ‘ $\theta_1$  -  $\theta_2$ ’ as poles overlap. A current impressed in the winding during this region produces positive torque. The stator and rotor poles are completely overlapped in the region ‘ $\theta_2$  -  $\theta_3$ ’ thus makes inductance constant and do not produce any torque. The inductance in this region is called aligned inductance  $L_a$ . The operation of the machine in the region ‘ $\theta_3$  -  $\theta_4$ ’ produces negative torque as inductance has negative slope. The regions ‘0 -  $\theta_1$ ’, ‘ $\theta_2$  -  $\theta_3$ ’, and ‘ $\theta_4$  -  $\theta_5$ ’ are usually called as dead zones (DZ) because these regions do not contribute any torque.

### 1.1.3 Speed-Torque Characteristics

The speed-torque characteristics of SRM are shown in Figure 1.4 ( [Husain, 2010] ). The phase current of the SRM rises sharply when phase is turned on due to low back-EMF at low speed operating region. The current can be controlled by either hysteresis current control or voltage pulse width modulation control. The back-EMF increases with the speed and suppress the rise of current due to fixed excitation voltage at higher speed. So advancing of phase turn-on angle is required to maintain the desired current level for maximum torque production. SRM operating under constant torque region for speed range up to base speed ( $\omega_b$ ).

Above the base speed, if back-EMF exceeds the supply voltage, chopping control or PWM control is not possible due to decrease in current since pole overlap begins & thereby the SRM operates under single pulse mode at higher speeds. The decrease in current can be encountered by increasing the conduction angle that allows the required amperes to be delivered to the phase. So constant power can be supplied to the drive by increasing the conduction angle, hence this region is called constant power region. The constant power operation can be allowed up to maximum possible conduction angle at speed  $\omega_p$ . At higher speeds above  $\omega_p$ , no further increase in conduction angle is possible, thereby the torque fall rapidly with  $\frac{1}{\omega^2}$ .

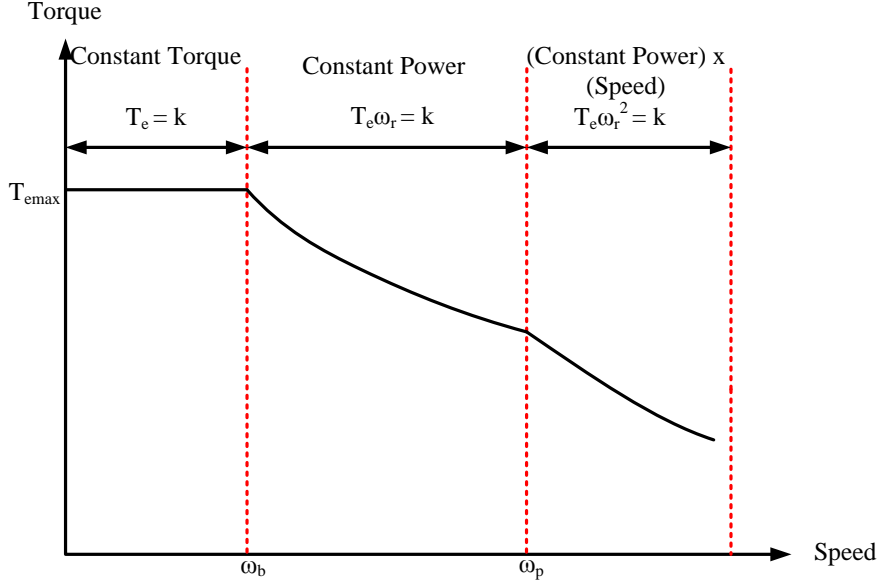


Figure 1.4: Speed-torque characteristics of SRM.

## 1.2 Torque Ripple in SRM

### 1.2.1 The Origin of Torque Ripple

The torque ripple is defined as the difference between the maximum and minimum instantaneous torque expressed as a percentage of the average torque during steady state operation.

$$T_{\text{ripple}} (\%) = \frac{T_{\text{max}} - T_{\text{min}}}{T_{\text{avg}}} \times 100\% \quad (1.8)$$

The torque pulsations are inherent in SRMs due to the double salient structure of the machine. The reluctance principle for torque production is utilised in these machines, where the phases operate independently and in succession. The majority of torque ripple is in the phase overlap region, where the torque producing responsibility is commutated from one phase to another. The amount of torque ripple is dictated by the magnetization pattern of individual phases and torque-current-rotor position ( $T-i-\theta$ ) characteristics of the motor.

The  $T-i-\theta$  characteristics of an SRM depend on the stator-rotor pole overlap angle, pole geometry, material properties, number of poles and number of phases. The torque dips in the  $T-i-\theta$  characteristics will decide the amount of torque ripple for a particular motor. The deficiency of incoming phase in supplying the

necessary torque at some rotor positions will lead to torque dips. Torque ripples can be minimized easily if torque dips are smaller.

### 1.2.2 Design Effects on Torque Ripple

By selecting a large number of rotor poles, the torque dips can be reduced by increasing number of strokes per revolution, but it will reduce the inductance ratio (ratio between maximum and minimum unsaturated inductance). The switching frequency increases with a large number of strokes that leads to high core losses. The regular choice for number of rotor poles in SRM is  $P_r = P_s - 2$ , where  $P_s$  is the number of stator poles and  $P_r$  is the number of rotor poles. ( [Husain, 2002](#) ).

The approach for reducing torque ripple is by increasing the number of phases without much decrease in inductance ratio. Selection of higher phase number will lead to increase of overlap region of phase torques during commutation. Three or less number of phases suffer from torque dips near the commutation region. In case of four and five phase machines, uniform torque can be achieved without boosting the phase current in low torque per ampere region. The drawback of a higher number of phases is that, the increase of one phase requires one additional phase leg in the converter which increases the cost of the converter.

### 1.2.3 Importance of Torque Ripple

The smoothness of torque is desired in direct drive applications, which requires high torque at low speeds. Direct drive electric power steering system demands very low torque ripples about 2% and robotics also desired to have very low torque ripple.

### 1.2.4 Possible Ways to Torque Ripple Minimization

There are two approaches to minimize torque ripple.

- By improving the magnetic design of the motor
- By using sophisticated electronic control

In the electronic control, torque pulsations can be reduced by selecting optimum combinations of operating parameters such as supply voltage, turn on & turn off angles, current level, and shaft load.

## 1.2.5 Basic Control of SRM for Torque Ripple Minimization

The inductance of a phase varies widely as a function of both rotor position and phase current. The phase inductance is the important factor for controlling the SRM. The hysteresis current control of SRM at low speed is shown in Figure 1.5.

Torque ripple can be reduced by improving inductance profile by modifying the geometry or by special control techniques. Especially at low speeds current control method is used as shown in Figure 1.5. At high speeds, the rate of change of flux linkage becomes so high that the maximum allowable voltage would not be enough to control the current. In this case, single pulse operation is usually applied, where only the conduction angle is controlled. In single pulse operation, the current waveform and peak current are depending on the conduction angle, inductance profile, and the winding resistance.

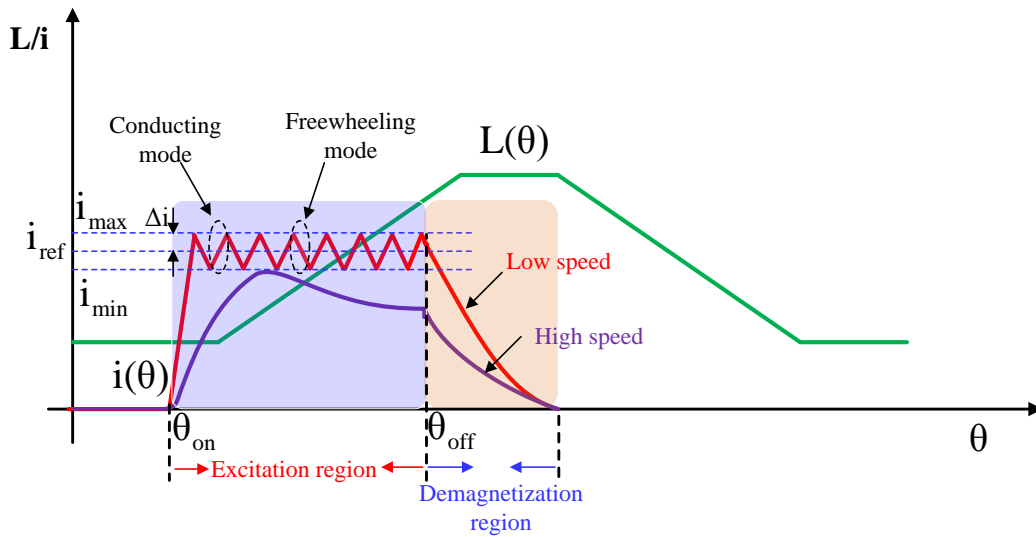


Figure 1.5: Hysteresis current control and single pulse operation of SRM

## 1.3 Literature on Torque Ripple Minimization for SRM

### 1.3.1 Torque Ripple Minimization with Improvements in Motor Design

The torque ripple can be reduced with pole-shape optimization. (Choi et al., 2007) proposed a new stator pole face that results in non-uniform airgap and a pole shoe is added to the lateral face of the rotor pole. These modifications reduce

the torque ripple. ( [Li et al., 2011](#) ) proposed a method to reduce torque ripple by altering the flux waveform and also modifying the waveform of  $\frac{dL}{d\theta}$  by punching holes in the rotor poles. Moreover, the torque ripple performance is analyzed for different dimension of holes in rotor pole. The review of performance optimization with geometry and topology modifications is presented in ( [Abdalmagid et al., 2022](#) ).

### 1.3.2 Commutation Angle Optimization and Current Control Methods for Torque Ripple Minimization

A new method to determine the optimal turn-on and turn-off angles in online is proposed in ( [Mademlis and Kioskeridis, 2003](#) ). From the flux linkage waveforms of two neighboring phases, formula for the optimal turn-off angle is developed in this work. The torque ripple minimization with pulse width modulation (PWM) current control is proposed in ( [Husain and Ehsani, 1996](#) ). In this method, the torque control strategy is developed such that the sum of all phase torques should be constant and equal to desired torque. During the commutation, the total torque required is shared between the two overlapping phases appropriately to achieve minimum torque ripple where as single phase is contributing to the total torque during the non overlapping of phase currents. [Mikail et al., 2013](#) proposed torque ripple minimization method with extending flat portion of the torque characteristics with design optimization in Finite Element Method (FEM) and required current profile is achieved through the fine tuning of control algorithm.

### 1.3.3 Torque Ripple Minimization with Torque Sharing Functions (TSF)

Torque ripple minimization can be achieved with the help of TSF denoted as  $f_k(\theta)$  by controlling the individual phase torques such that the total torque should be equal to the sum of the phase torques. The phase torque can be expressed as per Equation [1.9](#) in terms of TSF. The TSF profile for three phase SRM is shown in Figure [1.6](#).

$$\begin{cases} T_k = T_{ref} \times f_k(\theta) \\ \sum_{k=1}^n f_k(\theta) = 1 \end{cases} \quad (1.9)$$

Where  $T_{ref}$  is the desired torque command and  $T_k$  is torque of the phase ' $k$ '.

The TSF( $f_k(\theta)$ ) can be defined in terms of rotor position as per Equation [1.10](#).

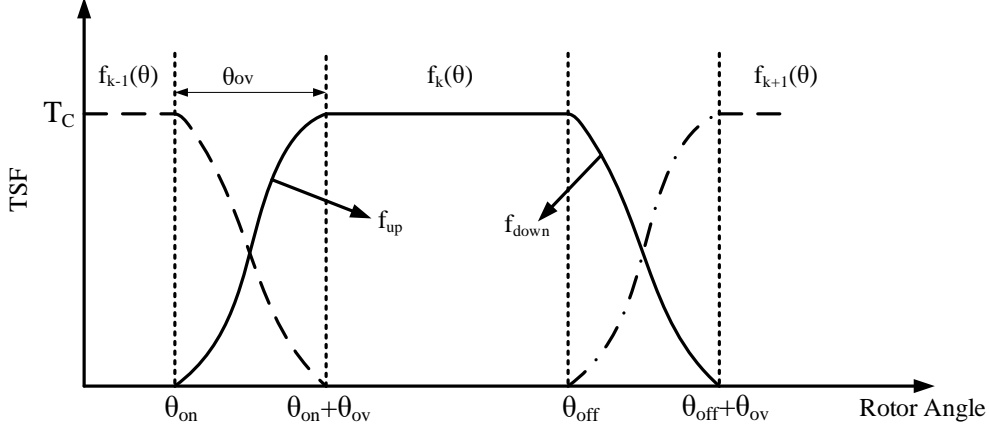


Figure 1.6: Typical TSF profile for a three-phase SRM

$$f_k(\theta) = \begin{cases} 0, & (0 \leq \theta < \theta_{on}) \\ f_{up}(\theta), & (\theta_{on} \leq \theta < \theta_{on} + \theta_{ov}) \\ T_{ref}, & (\theta_{on} + \theta_{ov} \leq \theta < \theta_{off}) \\ f_{down}(\theta), & (\theta_{off} \leq \theta < \theta_{off} + \theta_{ov}) \\ 0, & (\theta_{off} + \theta_{ov} \leq \theta < \theta_{off} + \theta_p) \end{cases} \quad (1.10)$$

where  $\theta_{ov}$  is the overlap angle between two adjacent phases and  $\theta_p$  denotes one rotor cycle.

The function for  $f_{up}(\theta)$  and  $f_{down}(\theta)$  for different TSF proposed in the literature ([Xue et al., 2009](#)) are as follows.

- Linear TSF

$$\begin{aligned} f_{up}(\theta) &= \frac{T_{ref}}{\theta_{ov}} (\theta - \theta_{on}) \\ f_{down}(\theta) &= T_{ref} - \frac{T_{ref}}{\theta_{ov}} (\theta - \theta_{on}) \end{aligned} \quad (1.11)$$

- Cubic TSF

$$\begin{aligned} f_{up}(\theta) &= \frac{3T_{ref}}{\theta_{ov}^2} (\theta - \theta_{on})^2 - \frac{2T_{ref}}{\theta_{ov}^3} (\theta - \theta_{on})^3 \\ f_{down}(\theta) &= T_{ref} - f_{up}(\theta - \theta_{off} + \theta_{on}) \end{aligned} \quad (1.12)$$

- Sinusoidal TSF

$$\begin{aligned} f_{up}(\theta) &= \frac{T_{ref}}{2} - \frac{T_{ref}}{2} \cos \frac{\pi}{\theta_{ov}} (\theta - \theta_{on}) \\ f_{down}(\theta) &= \frac{T_{ref}}{2} + \frac{T_{ref}}{2} \cos \frac{\pi}{\theta_{ov}} (\theta - \theta_{off}) \end{aligned} \quad (1.13)$$

- Exponential TSF

$$\begin{aligned} f_{up}(\theta) &= T_{ref} \left[ 1 - \exp \left( \frac{-(\theta - \theta_{on})^2}{\theta_{ov}} \right) \right] \\ f_{down}(\theta) &= T_{ref} \left[ \exp \left( \frac{-(\theta - \theta_{off})^2}{\theta_{ov}} \right) \right] \end{aligned} \quad (1.14)$$

[Kjaer et al., 1996] reported a high grade control of SRM using TSF. In this method, the commutation point is defined where two neighboring phases producing the equal torque at equal level of current. This paper reported different commutation angles for low speed high efficiency and high speed low flux operation for torque ripple minimization. [Xue et al., 2009] developed a improved TSF for torque ripple minimization. This paper stated that efficiency, losses, speed range and maximum speed are significantly affected by turn-on angle and overlap angle for a given torque. Therefore the proposed TSF are dependent on turn-on angle, overlap angle and desired torque. The authors used the genetic algorithm for optimizing turn-on and overlap angle for different torque levels. The authors stated that large speed range and low copper losses can be achieved by optimizing the TSF.

( [Choi et al., 2002] ) proposed a new TSF which extends TSF region to negative torque region to provide sufficient time for current rising and current falling under positive torque region, thereby improves the speed-torque performance. ( [Vujičić, 2011] ) proposed a new family of TSF for torque ripple minimization and optimization of TSF is carried out by considering the secondary objective as copper loss minimization. Further, improved TSFs are proposed by ( [Ye et al., 2015], [Sun et al., 2016], [Li et al., 2018] ) for torque ripple reduction. However, these methods necessitate accurate rotor position and high memory requirements to store machine characteristics which are undesirable features for the real-time implementation.



## 1.4 Literature on Direct Torque Control for SRM

Direct torque control (DTC) techniques are proposed for SRM to overcome the aforementioned shortcomings, namely direct instantaneous torque control, direct torque and flux control and advanced DTC strategies. Among them, the DTC scheme draws more attention which utilizes the principle of DTC applied to traditional AC machines. This method offers advantages such as automatic control (no turn-on/off angle control), fast dynamic response, reduced acoustic noise, insensitivity to motor parameters and does not require rotor position information. Moreover, this method does not require any winding arrangements and provides an easy extension to multi-phase SRMs. The detailed methodology of DTC is presented in Chapter 2. Direct torque control (DTC) for SRM is introduced by ( [Cheok and Fukuda, 2002] ). The voltage vector selection adopted in this method, results in negative phase torque generation. Therefore, the active phase has to develop more torque to compensate for the negative torque generated by the outgoing phase due to an extension of phase current in the negative inductance slope region. Therefore, it draws more current from the source, thereby reducing net torque per ampere (T/A) and the drive efficiency. Also, this negative torque generation results in large torque pulsations.

( [Inderka and De Doncker, 2003] ) proposed a on-line direct instantaneous torque control. In this method, torque is estimated as a function of flux linkages and currents, thereby need of rotor position is eliminated. Moreover this method uses hysteresis torque controller for torque regulation. The comparative study of DTFC and DITC is presented in ( [Ronanki and Williamson, 2017] ). The authors stated that DTFC requires more current to maintain constant flux linkages at different speeds. ( [Ai-de et al., 2018] ) proposed a sector reformation technique for three-phase SRM to select the vectors more precisely. In this method, 9 and 12 sectors are used instead of 6 sectors in conventional DTC.

## 1.5 Literature on Phase Current Reconstruction Algorithms for SRM

Acquisition of the accurate phase currents is indispensable for the control and protection of SRM drives. The concept of single-sensor current regulation for SRM is first introduced in ( [Kjaer and Gallegos-Lopez, 1998] ). The phase current detection methods for SRMs using one sensor is developed using a

double high-frequency pulse injection under current chopping control (CCC) and DITC schemes ( [Gan et al., 2014] ), ( [Gan et al., 2016a] ). These methods are further extended for position sensor less, fault-diagnosis and independent current control of dual-parallel SRM drives ( [Gan et al., 2015] , [Gan et al., 2016b] ). In these methods, two conducting currents are separated by injecting high-frequency pulses to corresponding gate signals. However, these methods cause the voltage penalty, increase the converter switching losses and complexity to implement the algorithm( [Ronanki et al., 2020] ). If the inverter brought to the state for sensing the current, which is contradict to the phase voltage specified by the current regulator, that sensing is associated with "voltage penalty". Moreover, these approaches cannot be extended to SRMs having phase number more than four. Alternatively, phase current can be estimated without pulse injection by changing sensor's placement, splitting the dc-bus and the converter topology. However, these methods need significant modifications in the conventional power converter topology ( [Sun et al., 2017] , [Song et al., 2017] , [Han et al., 2017] , [Gan et al., 2017] , [Cheng et al., 2021] ).

A multiplexed two-sensor current detection strategy is presented for multi-phase SRMs (four, five and six) to extract the phase currents by adjusting the converter structure and high-frequency pulse injection ( [Gan et al., 2018] ). However, voltage penalty, higher switching loss, and current distortion issues are inevitable due to the pulse injection. Furthermore, the demagnetization current cannot be detected and complexity in implementation. An advanced phase current reconstruction method with multiplexed current sensors is presented for multi-phase SRM systems without any converter change and pulse injection ( [Sun et al., 2018] ). An improved current-sensing scheme for TSF controlled three-phase SRM drive with two current sensors is introduced in ( [Gan et al., 2020] ). In this method, rotor position is detected by implementing a flux linkage-current-based method, which is used to instantaneous phase torque and current reconstruction. A summary of aforementioned phase current reconstruction approaches for SRM drives is listed in Table [1.1](#). These phase reconstruction techniques are designed for CCC, DITC and TSF techniques in which only two phases are active at the same time. The detailed methodology of theses phase current reconstruction are discussed in chapter 4.

Table 1.1: Comparison of existing phase current reconstruction schemes

Method	Phase Number	Control Scheme	Current Sensor Number	Pulse Injection	Converter Adjustment	Voltage Penalty	Control Complexity
Kjaer and Gallegos-Lopez, 1998	3	CCC	1	Yes	Required	Yes	Complicated
Gan et al., 2014	4	CCC	1	Yes	Required	Yes	Complicated
Gan et al., 2015 ; Gan et al., 2016b	3	CCC	1	Yes	Required	Yes	Complicated
Gan et al., 2016a	3	DITC	1	Yes	Required	Yes	Complicated
Sun et al., 2017	4	CCC	1	Yes	Required	No	Complicated
Song et al., 2017	3	CCC	1	No	Not Required	No	Medium
Han et al., 2017	3	CCC	2	No	Not Required	No	Medium
Gan et al., 2017	4	CCC	2	No	Required	No	Medium
Cheng et al., 2021	3	CCC	2	No	Required	No	Medium
Gan et al., 2018	Multi	CCC	2	Yes	Required	Yes	Complicated
Sun et al., 2018	Multi	CCC	2,3	No	Not Required	No	Simple
Gan et al., 2020	3	TSF	2	No	Not Required	No	Complicated

## 1.6 Motivation in the Present Work

Different control algorithms are proposed for SRM in the state-of-art literature for torque ripple minimization, copper loss minimization, T/A improvement such as angle optimization, phase current profiling and TSF based algorithms. These methods require accurate rotor position information, need for storing characteristic data and complex computations are involved in the implementation. To address this issue DTC method is developed for SRM. However, this conventional DTC method draws higher source current from the source and results in high torque pulsation due to the improper voltage selection. The reason behind the low T/A and high torque ripple is the generation of negative torque due to the excitation of the phase which is under negative inductance slope region. The minimization of negative phase torque to improve the performance of SRM in terms of torque ripple reduction, T/A improvement and source current ripple reduction is not addressed in the literature. Moreover, different phase reconstruction techniques are developed for the current control technique where only two-phases are conducting simultaneously. The phase current detection is complex due to the simultaneous conduction of all phases in DTC controlled drives, which is not addressed in the literature.

## 1.7 Research Objectives

- Dynamic modeling of four phase SRM using magnetic and torque characteristics.
- Analysis of DTC of four phase SRM in terms of torque ripple, T/A and source current ripple.

- Develop a new DTC strategy to enhance T/A ratio as well as torque ripple reduction based on sector reformation and optimized voltage vector selection for four phase SRM.
- Develop a low cost and reliable DTC strategy for four phase SRM by reducing number of current sensors required.

## 1.8 Thesis Organization

There are six chapters and two appendices in the thesis document. The outline of the thesis as follows. The overview of the thesis is shown in Figure [1.7](#).

**Chapter 1:** This chapter presents a brief introduction to switched reluctance motor drive, design aspects, source of high torque ripple, state-of-art control algorithms for torque ripple minimization, start-of-art direct torque control methods. In addition to that state-of-art phase current reconstruction methods are presented in this chapter.

**Chapter 2:** This chapter presents the dynamic modeling of four phase SRM using flux linkage and torque characteristics. Detailed simulation studies of conventional direct torque control algorithm constitutes 8-sectors 8-vectors are presented at different speeds. In addition to that the negative phase torque generation and existence of current in the dead zone and its impact on torque ripple and T/A are presented.

**Chapter 3:** This chapter presents the proposed 16-sector 8-vector DTC algorithm. The sector partition and optimized voltage vector selection are discussed in detail and the effectiveness of the proposed algorithm on torque ripple and T/A is evaluated and results are compared with Conventional DTC method. The negative torque generation still persists in this method due to long tail currents. To overcome this issue, 16 sector 16 vector is proposed to extinguish the current quickly before entering into negative torque region. The comparison studies of proposed DTC and Conventional DTC are presented under both steady state & dynamic conditions to highlight the superiority of proposed DTC methods.

**Chapter 4:** This chapter proposes a novel phase current reconstruction algorithm for direct torque controlled SRM drive with reduced number of current sensors compared with sensor per phase. The reconstructed phase current is used for flux linkage calculations. To validate the efficacy of

proposed phase current detection method, the reconstructed phase currents are compared with currents obtained by sensor per phase method. The method of phase current reconstruction and real time simulation results with OPAL-RT along with MATLAB simulation studies are presented in this chapter to validate the efficacy of proposed phase current reconstruction algorithm.

**Chapter 5:** This chapter presents hardware implementation of four phase SRM drive. The measurement of phase inductance, rotor position, and method for developing commutation for SRM are discussed. In addition to that, development of voltage control and hysteresis current control using STM32 microcontroller with the help of CUBEMX and Keil  $\mu$ Vision software is discussed and hardware results are presented.

**Chapter 6:** Summarizes the significant contributions of the thesis and include some discussions on future research.

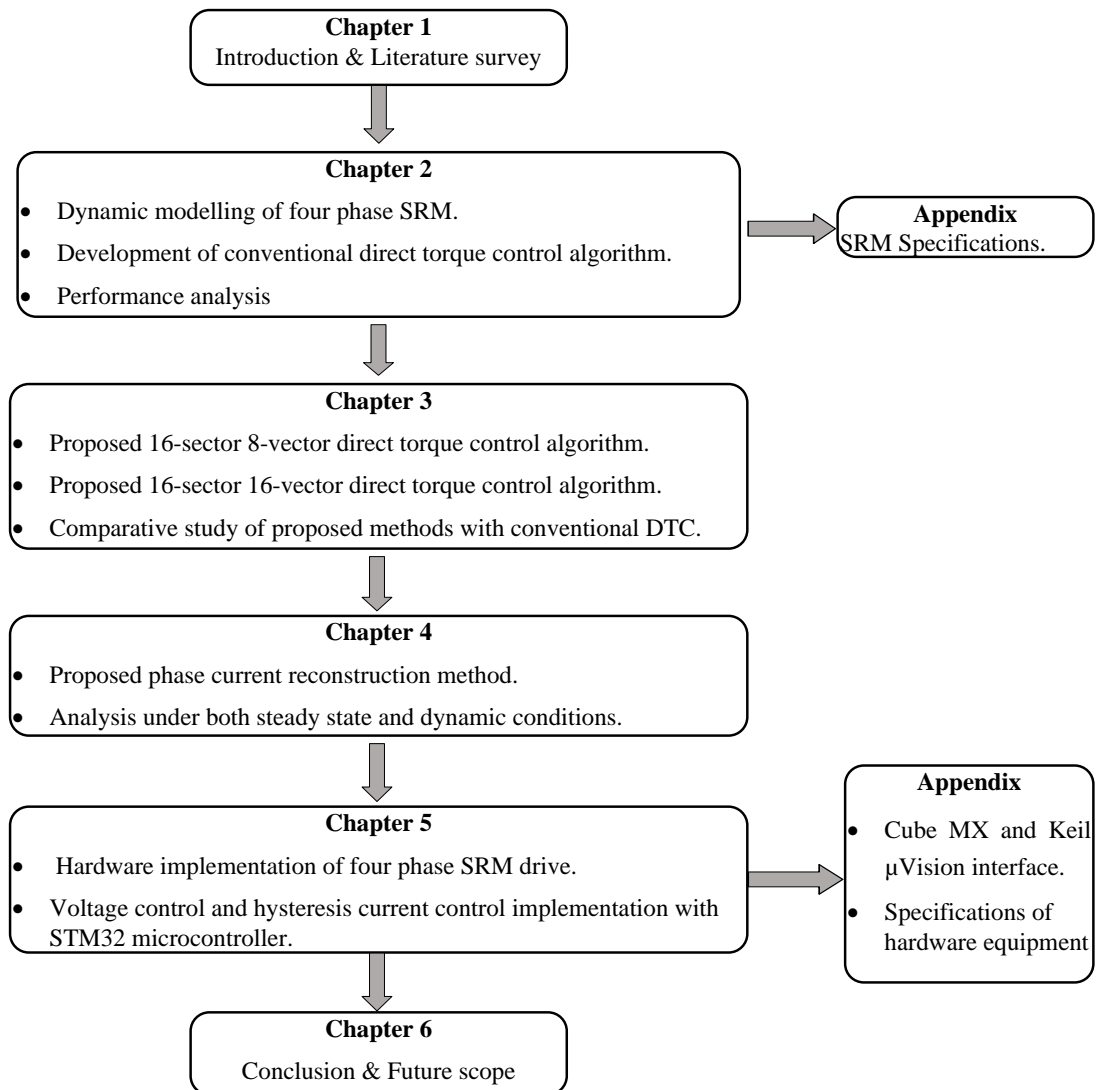


Figure 1.7: Thesis organization



# Chapter 2

## Direct Torque Control of Switched Reluctance Motor Drive

### 2.1 Introduction

The SRM has a doubly salient structure and operates in the saturation region in order to attain a high energy conversion rate, which makes it a highly non-linear machine. Therefore, it is necessary to develop an accurate and non-linear model for precise control of the SRM. Several modeling methods for the SRM are available in the literature, including finite element analysis (FEA) based techniques, analytical methods( [Le-Huy and Brunelle, 2005]) and lookup table approach. In this work, an interpolation and look-up table based approach is adopted using the torque and magnetic characteristics, which can be obtained either by FEA or experimental measurement. The characteristics obtained from experimental measurements are more suitable for modeling of SRM as it is more accurate than FEA because FEA excludes some complex secondary effects. In this study, a non-linear dynamic model of SRM is developed using method described in [Chancharoensook and Rahman, 2002]. The flux and torque characteristics obtained from the experimental studies of a real SRM in the form of two-dimensional (2D) lookup tables are used for modeling. The dynamic model of the four-phase SRM is developed in MATLAB/Simulink platform.

### 2.2 Dynamic Modeling of Four-Phase SRM

#### 2.2.1 Experimental Determination of Magnetization & Static Torque Characteristics

The block diagram of the experimental setup for the determination of magnetization and static torque characteristics is shown in Figure 2.1. The experimental procedure for obtaining these characteristics is described



in [Ramanarayanan et al., 1996](#). A dividing head is used to hold the rotor at a specified position precisely against the high torque produced due to applied voltage. In this experiment, H- Bridge consists of two switches and two diodes is used to control the excitation. The phase winding draws the rated current from excited square wave voltage. The voltage and current waveforms are captured and processed for flux linkage calculations.

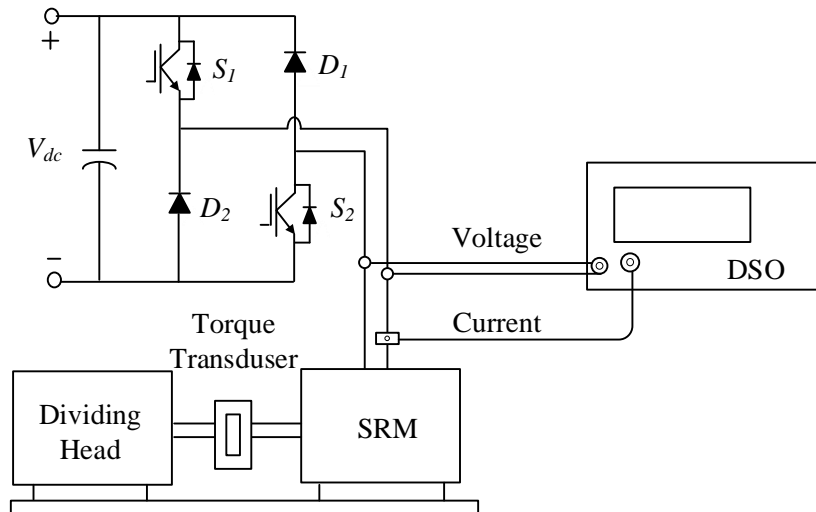


Figure 2.1: Block diagram of experimental setup for determination of magnetization and static torque characteristics

The steps involved in the experimental determination of motor characteristics are given below.

- Hold the rotor against high torque produced during the experiment.
- A voltage pulse is applied to one of the phases of SRM, with all the other phases open.
- The voltage and current waveforms are recorded in the digital signal oscilloscope (DSO).
- The rotor is rotated to a set of equally spaced rotor positions between unaligned to aligned position and procedure is repeated at each rotor position.
- The data recorded in DSO is transferred to the computer and numerical integration is performed using composite simpson's rule to calculate flux

linkages using the equation 2.1.

$$\psi = \int (v - ir) dt \quad (2.1)$$

- The validity of results is checked by evaluating the static torque with the above data and verifying the same by experiment.

## 2.2.2 Flux Linkage and Torque Characteristics

The flux linkage and torque characteristics of the 4 kW four-phase (8/6) SRM, which are obtained from the experimental studies are shown in Figures 2.2a & 2.2b. These experimental characteristics are taken from [Rajesh and Singh, 2014].

The parameters of the motor used for simulation studies are given as phase resistance ( $r_j$ ) = 0.7  $\Omega$ , unaligned inductance  $L_u$  = 12 mH and aligned inductance  $L_a$  = 110 mH, moment of inertia (J) = 0.016 kg-m<sup>2</sup>, and friction coefficient (B) = 0.0065 Nms.

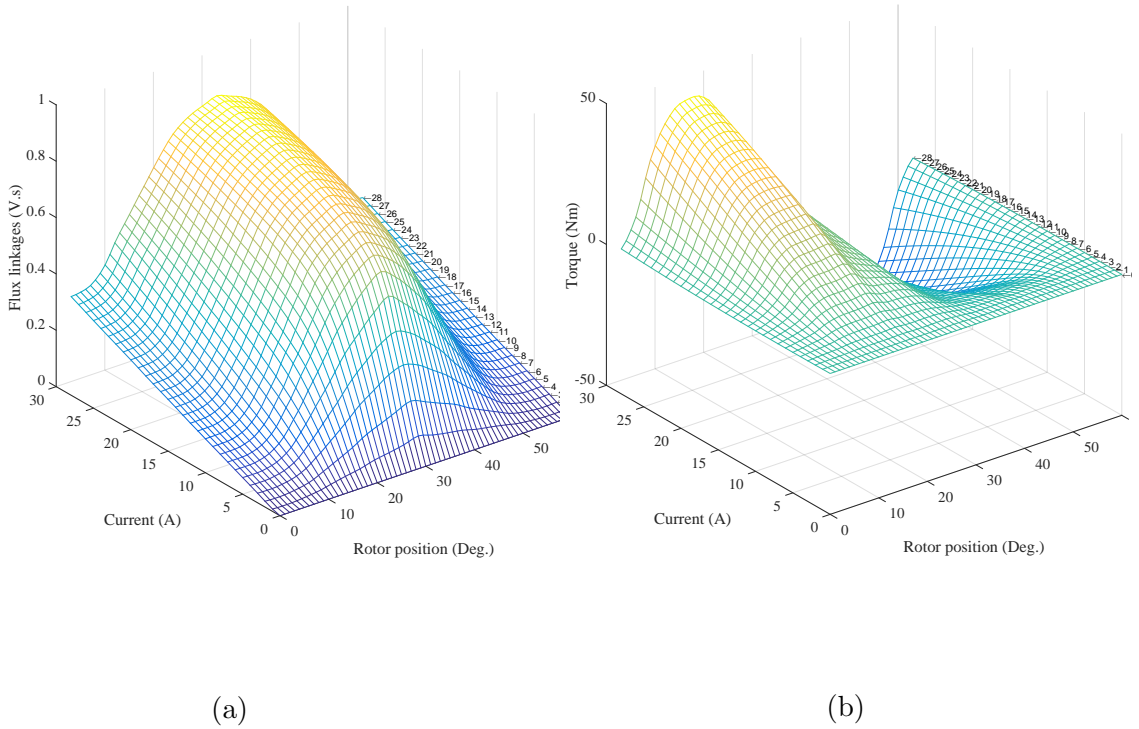


Figure 2.2: SRM characteristics plotted from experimental data (a) Flux-linkage characteristics, (b) Torque characteristics

### 2.2.3 Mathematical Modeling of Four Phase SRM

The dynamic model of an SRM comprises of a set of electrical equations for each phase and system dynamics. Neglecting mutual coupling, the phase voltage equation of SRM model for m-phase machine can be expressed as

$$v_j = (r_j \cdot i_j) + \frac{d\psi_j(i_j, \theta_j)}{dt}; \quad j = 1, 2, \dots, m \quad (2.2)$$

$$v_j = (r_j \cdot i_j) + \left( \frac{\partial \psi_j}{\partial i_j} \cdot \frac{di_j}{dt} \right) + \left( \frac{\partial \psi_j}{\partial \theta_j} \cdot \frac{d\theta_j}{dt} \right) \quad (2.3)$$

The dynamic equation of the phase current can be expressed as

$$\frac{di_j}{dt} = \left[ \frac{\partial \psi_j}{\partial i_j} \right]^{-1} \cdot \left[ v_j - (r_j \cdot i_j) - \left( \frac{\partial \psi_j}{\partial \theta_j} \cdot \omega \right) \right] \quad (2.4)$$

Where  $v_j$ ,  $i_j$ ,  $r_j$ ,  $\psi_j$  and  $\theta_j$  represent the terminal voltage, phase current, phase winding resistance, flux linkages, rotor position of 'j' phase respectively and  $\omega = d\theta/dt$  is the rotor speed. The general expression of the instantaneous torque by one phase at any rotor position can be expressed as

$$T_j = \left. \frac{\partial W_c(i_j, \theta)}{\partial \theta} \right|_{i_j = \text{constant}} \quad (2.5)$$

where  $W_c(i_j, \theta)$  denotes co-energy, which can be given by

$$W_c = \int_0^{i_j} \psi_j(i_j, \theta) \cdot di \quad (2.6)$$

The expression for instantaneous torque  $T_j$  can be given by

$$T_j \simeq i_j \cdot \frac{\partial \psi_j(i_j, \theta)}{\partial \theta} \quad (2.7)$$

The dynamics of the mechanical system is represented by

$$\frac{d\omega}{dt} = \frac{1}{J} \left[ \sum_{j=1}^m T_j(i_j, \theta_j) - T_L - B \cdot \omega \right] \quad (2.8)$$

The SRM model is developed using the above dynamic equations and the machine characteristics shown in Figure [2.2](#). The phase model of SRM is shown in Figure [2.3](#) and the complete four phase SRM model is shown in Figure [2.4](#).

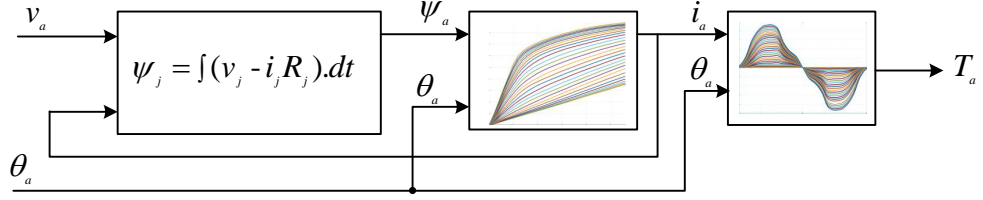


Figure 2.3: Phase model of SRM

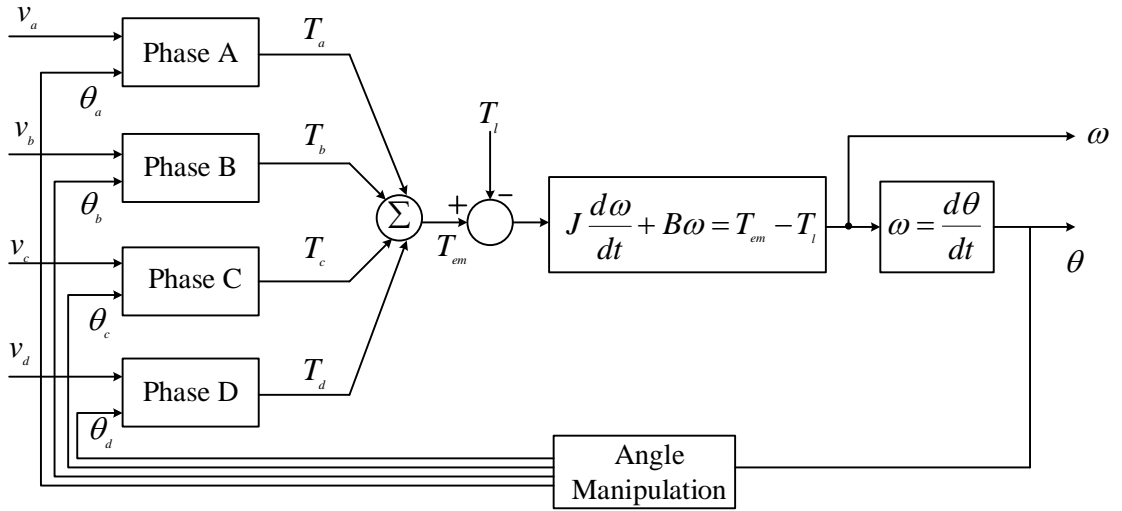


Figure 2.4: Four phase model of SRM

## 2.3 Asymmetrical Half-Bridge Converter (AHBC)

The AHBC is a widely used power converter topology to drive the SRM, as it allows independent control of each phase. The electric circuit diagram, along with their operating modes for the four phase SRM is shown in Figures 2.5 & 2.6. One H-bridge module is required to drive one-phase of the SRM, which comprises of two power switching devices  $[S_1, S_2]$ , and diodes  $[D_1, D_2]$  and the phase winding is connected in series with the power switches. There are three possible states that can be achieved through an AHBC to drive the SRM. The positive  $dc$  voltage ( $+V_{dc}$ ) is applied across the phase winding when both switches in the same phase leg are turned on as shown in Figure 2.6a, which represents the magnetization state and is denoted by '1'. The freewheeling state can be achieved by turning off one of the switches as shown in Figure 2.6b, that applies zero voltage across switch, which is denoted by '0'. To decrease the current abruptly, both switches are turned-off

as shown in Figure 2.6c. In this mode, negative  $dc$  voltage is applied across the winding leading to commutation of a phase. This state is called demagnetization mode and is represented as ‘ $-1$ ’. The summary of the possible voltage states for phase A is listed in Table 2.1.

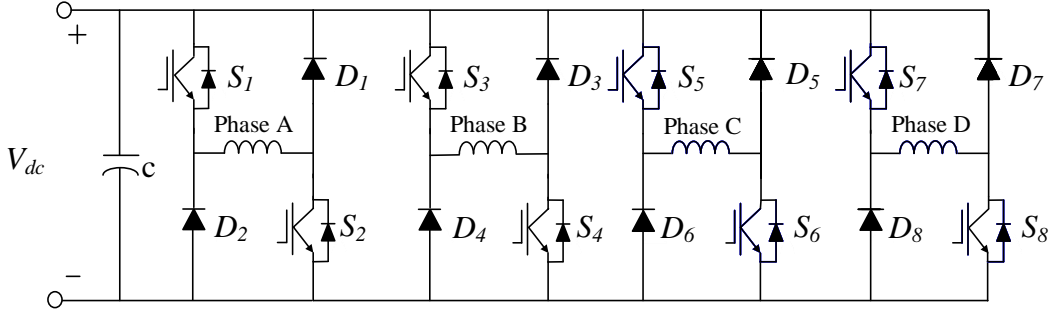
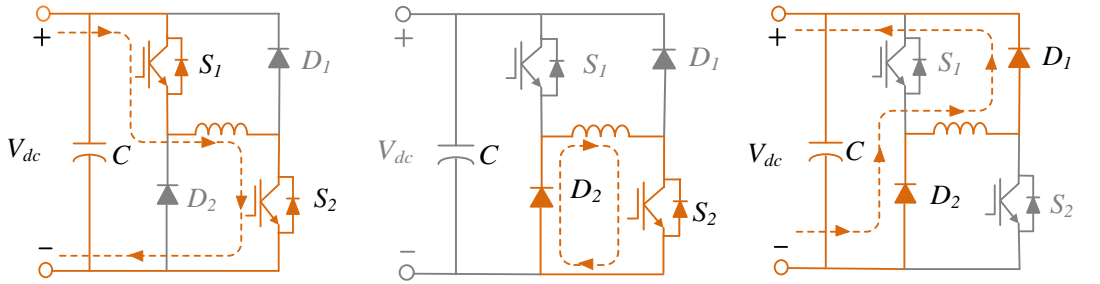


Figure 2.5: Asymmetric half-bridge converter (AHBC)



(a) Magnetizing state (+1) (b) Freewheeling state (0) (c) Demagnetizing state (-1)

Figure 2.6: Modes of operation of AHBC

Table 2.1: Operating modes of AHBC

$S_1$	$S_2$	$D_1$	$D_2$	State
1	1	0	0	magnetizing state (+1)
1	0	1	0	freewheeling state (0)
0	1	0	1	freewheeling state (0)
0	0	1	1	demagnetizing state (-1)

## 2.4 Direct Torque Control (DTC)

The DTC of SRM is developed from the philosophy of DTC used for AC machines. It has been shown to provide a simple solution to control the torque to minimize torque ripple. However, previously DTC has been almost exclusively

applied to AC motors which have linear characteristics and three phase balanced sinusoidal excitation. However, the SRM has a nonlinear model and non sinusoidal excitation. Furthermore, the excitation is normally not balanced between phases, as the phases are independently excited. Therefore, the SRM has not been seen as conducive to conventional AC machine DTC theory. In this scheme, torque is directly controlled by accelerating and decelerating the flux linkage vector.

The DTC scheme overcomes the problems associated with torque ripple control in the SRM. This is because the scheme directly regulates the torque output of the motor within a hysteresis band. So the torque ripple control is an inherent part of the DTC scheme. Hence this method does not require a mathematical model or knowledge of the motor parameters for torque ripple minimization, which overcomes the difficulties in applying conventional torque ripple control due to the highly nonlinear nature of the motor. Another advantage of the DTC scheme applied to the SRM is that the scheme is very simple and can be implemented with low cost microprocessor hardware.

### 2.4.1 Conventional Direct Torque Control of Four-Phase SRM

The DTC strategy is very popular for conventional AC machines and have been applied to the SRM. DTC control scheme works to achieve the following objectives.

- To maintain the constant magnitude (within hysteresis bands) of the stator flux linkage vector.
- To maintain the electromagnetic torque in the limits of hysteresis band by accelerating or decelerating the stator flux vector according to the requirement of torque increase or decrease.

The principle of vector selection in DTC involves acceleration and deceleration of the flux linkage vector to compensate torque and flux errors. Furthermore, the torque control of an SRM depends only on the stator flux vector's variation, thus no need for motor information. The control block diagram of the DTC scheme for an SRM is shown in Figure 2.7. The ' $v_{abcd}$ ' is the voltage across the four phases 'A', 'B', 'C', and 'D' and ' $i_{abcd}$ ' is the current flowing through the phases. The  $S_a, S_b, S_c, S_d$  are the gate signals for four phases. The flux linkages  $\psi_{abcd}$  are determined from the voltage, current and

phase winding resistance as per Equation 2.1. The DTC structure comprises of flux-linkage control, torque control and a flux-linkage vector's position information to choose voltage vector such that the desired torque control is achieved.

To evaluate the stator flux linkage vector, the flux vectors for four-phase SRM are transformed into the d-q reference axes

$$\left. \begin{aligned} \psi_s &= \psi_d + j\psi_q \\ |\psi_s| &= \sqrt{\psi_d^2 + \psi_q^2} \\ \theta &= \tan^{-1}\left(\frac{\psi_q}{\psi_d}\right) \end{aligned} \right\} \quad (2.9)$$

where  $\psi_s$ ,  $\theta$  represents the flux linkage vector's magnitude and angle, which is used to determine the sector  $N_k$  ( $k = 1, 2, \dots, 8$ ). The torque can be estimated through the measurements by torque sensor or pre-determined torque characteristics of the motor.

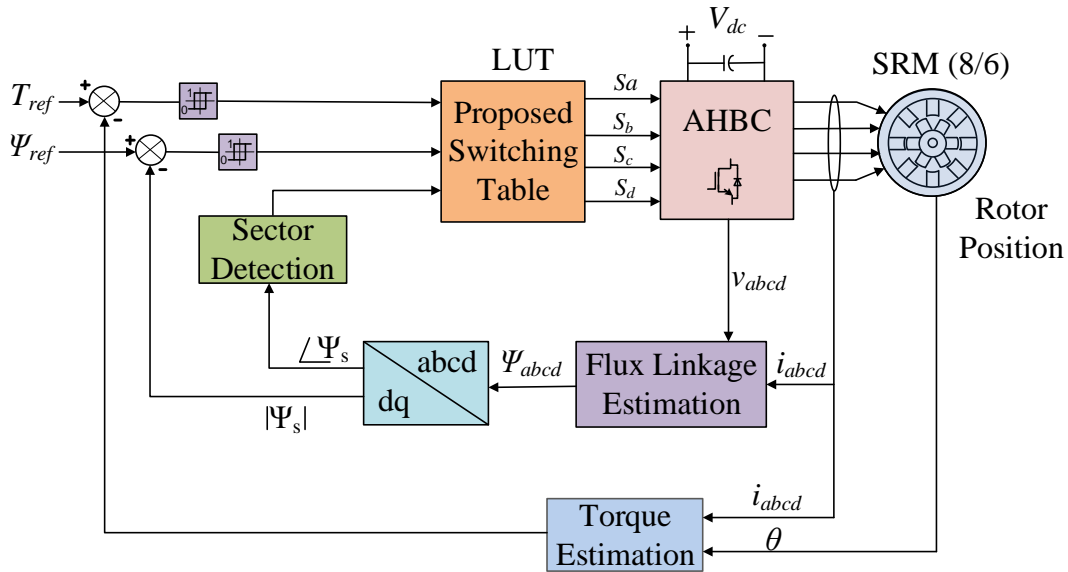


Figure 2.7: DTC block diagram of SRM

## 2.4.2 Sector Partition & Selection of Voltage Vectors

The definition of vectors and sector formation for conventional DTC is shown in Figure 2.8 and the corresponding switching table is presented in Table 2.2.

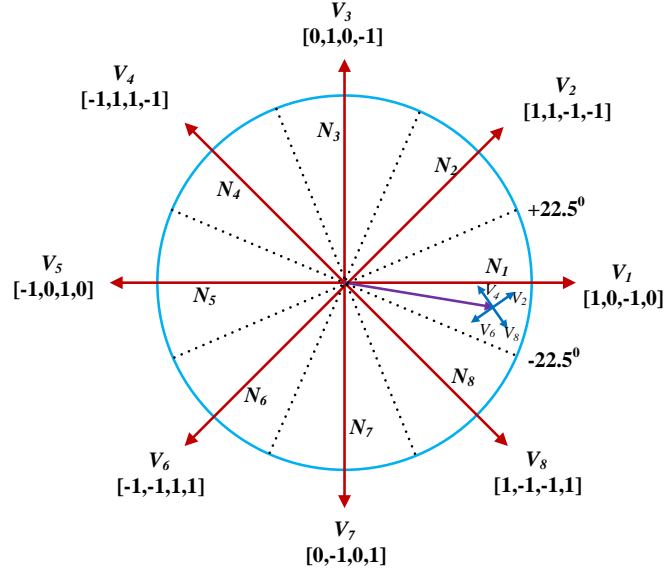


Figure 2.8: Definition of voltage vectors and partition of sectors for conventional DTC

Table 2.2: Voltage vector selection for conventional DTC

Sector	$T \uparrow \psi \uparrow$	$T \uparrow \psi \downarrow$	$T \downarrow \psi \uparrow$	$T \downarrow \psi \downarrow$
$N_1$	$V_2$	$V_4$	$V_8$	$V_6$
$N_2$	$V_3$	$V_5$	$V_1$	$V_7$
$N_3$	$V_4$	$V_6$	$V_2$	$V_8$
$N_4$	$V_5$	$V_7$	$V_3$	$V_1$
$N_5$	$V_6$	$V_8$	$V_4$	$V_2$
$N_6$	$V_7$	$V_1$	$V_5$	$V_3$
$N_7$	$V_8$	$V_2$	$V_6$	$V_4$
$N_8$	$V_1$	$V_3$	$V_7$	$V_5$

In the conventional DTC scheme, total electrical space is divided into eight sectors with an angle of  $45^\circ$ , as shown in Figure 2.8. The selection of the voltage vectors based on the increment and decrement of torque and flux for conventional DTC is tabulated in Table 2.2. The selection of the voltage vector is as follows.

- The voltage vector, which makes an angle that does not exceeds  $\pm 90^\circ$  with the stator flux vector is selected to increase the flux.
- The voltage vector, which makes an angle that exceeds  $\pm 90^\circ$  with the stator flux vector is selected to decrease the flux.



- The torque can be increased and decreased by accelerating and decelerating the stator flux vector respectively.

### 2.4.3 Simulation Results of Conventional DTC

The MATLAB simulations are carried out for four phase SRM having the specification listed in Table 2.3. The simulation results of conventional DTC at operating conditions of flux linkage  $\psi_{ref} = 0.6$  volt seconds, reference torque  $T_{ref} = 5$  Nm & speed  $N = 500$  rpm are presented in Figure 2.9. The simulation result shows that large torque ripple is presented in the electromagnetic torque  $T_{em}$ . The phase currents  $i_a$ ,  $i_b$ ,  $i_c$ , and  $i_d$  are conducting for entire cycle that results in negative torque generation which can be observed in the phase torque waveforms  $T_a$ ,  $T_b$ ,  $T_c$ , and  $T_d$ .

Table 2.3: Specifications of four phase SRM

Parameter	Rating
Rated Power ( $P$ )	4 kW
Rated Torque ( $T$ )	25 Nm
DC link voltage ( $V_{dc}$ )	280 V
Rated Speed ( $N_{rated}$ )	1500 rpm
Aligned Inductance ( $L_a$ )	110 mH
Unaligned Inductance ( $L_u$ )	12 mH
Phase Resistance ( $r$ )	0.7 $\Omega$
Moment of Inertia ( $J$ )	0.016 $kg - m^2$
Friction Coefficient ( $B$ )	0.0065 Nm.s

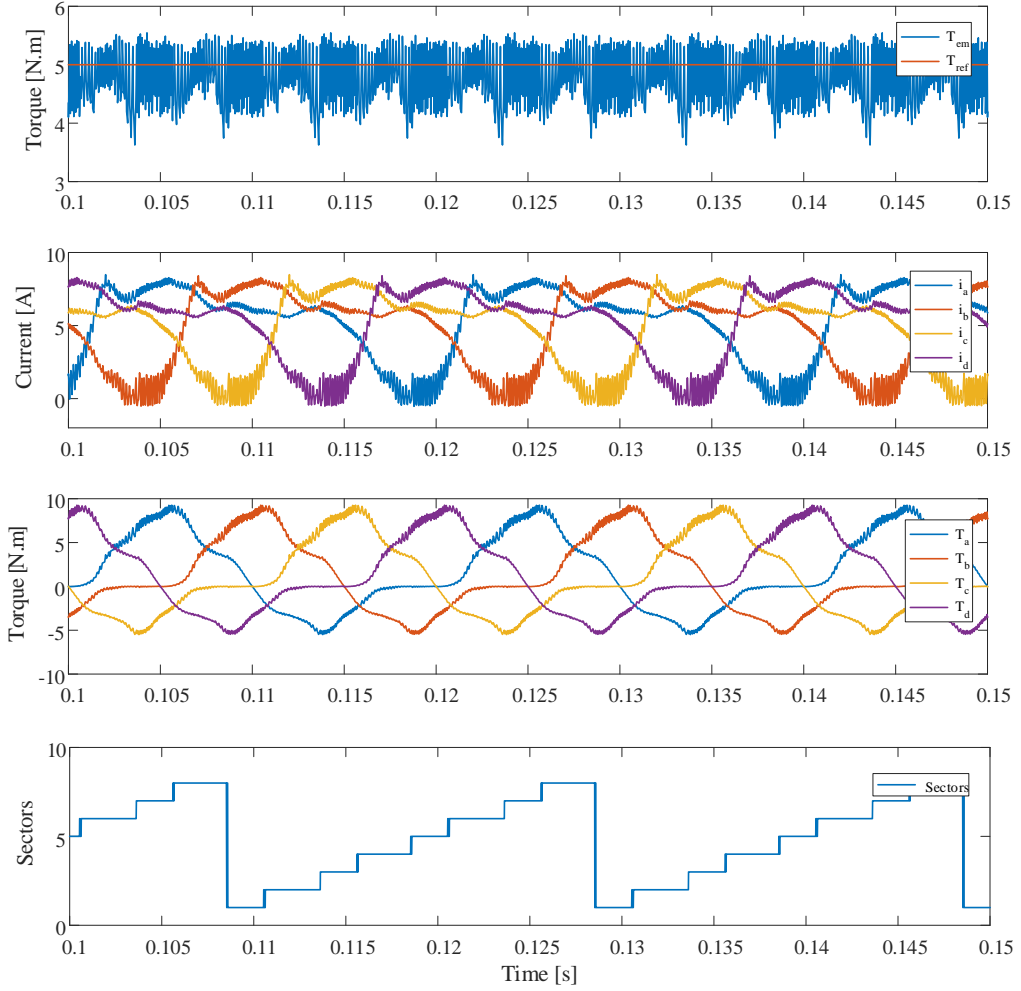


Figure 2.9: Simulation results of electromagnetic torque  $T_{em}$ , phase currents  $i_a$ ,  $i_b$ ,  $i_c$  and  $i_d$ , phase torques  $T_a$ ,  $T_b$ ,  $T_c$  and  $T_d$ , and sectors for conventional DTC at  $N = 500$  rpm

The voltage across & current through phase A winding along with the gating signals are presented in Figure 2.10. The result shows that the switches are switching at high frequency rate that results in more switching losses. Further, the phase current and phase torque waveforms are plotted in the same axis to interpret the phase torque generation with respect to phase current, which is shown in Figure 2.11. From this interpretation, it can be observed that motor phase winding carries the current during the negative torque region as well as zero torque region. The existence of current in negative and zero torque region decreases the T/A ratio and also results in high torque pulsations. The performance of the SRM drive can be determined in terms of torque ripple and T/A. The T/A ratio is given by

$$T/A = \frac{T_{rms}}{I_{dc-rms}} \quad (2.10)$$

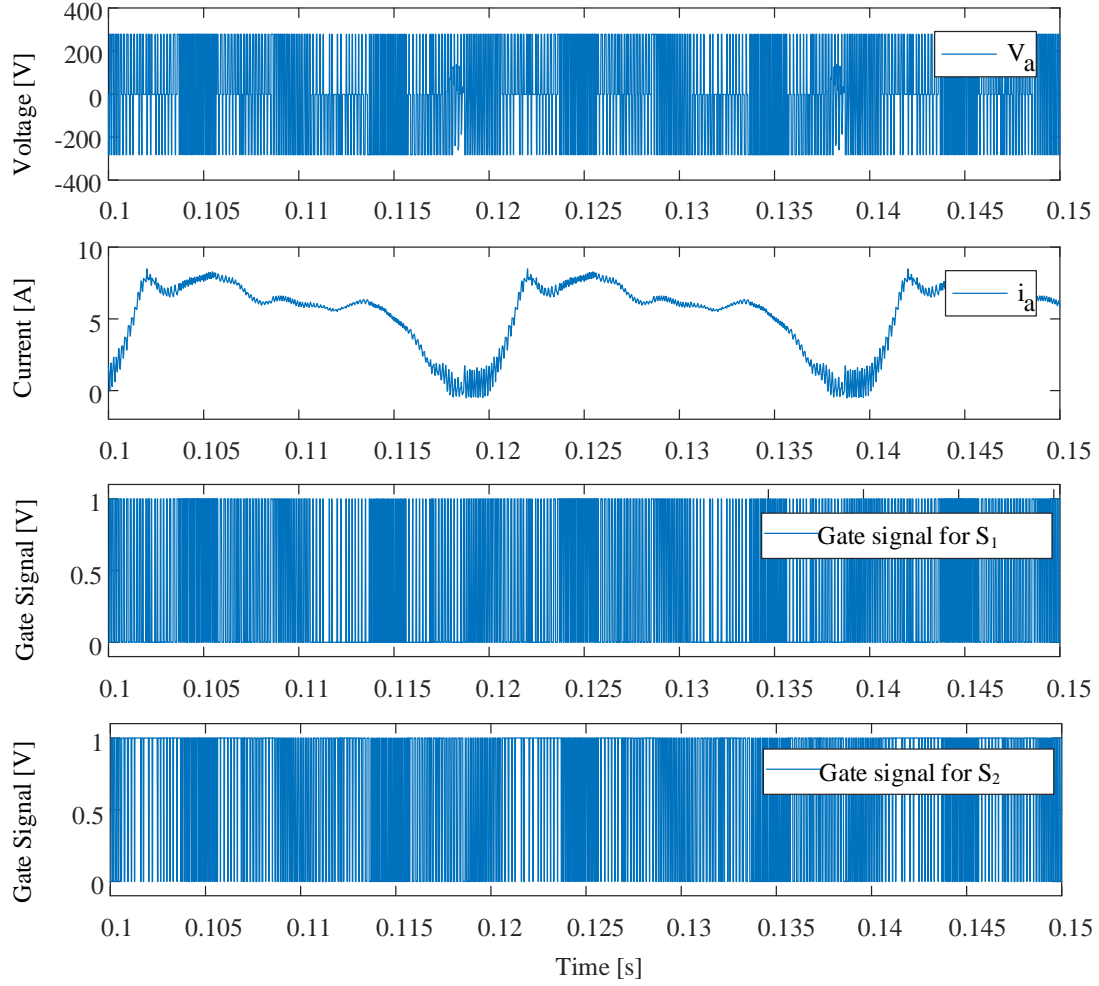


Figure 2.10: Simulation results of phase voltage  $V_a$ , phase current  $i_a$  and corresponding gate signals of  $S_1$ ,  $S_2$  for Conventional DTC at  $N = 500$  rpm

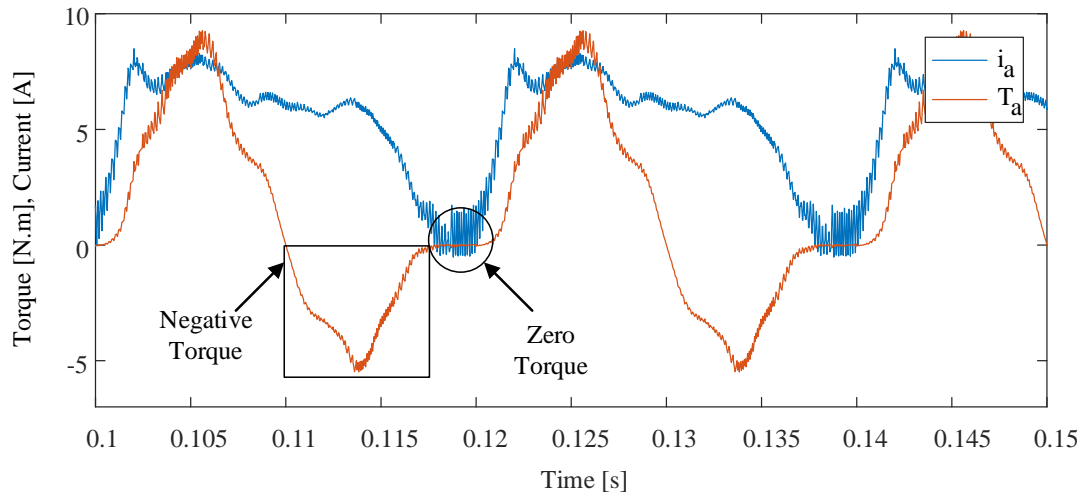


Figure 2.11: Interpretation of zero and negative torque regions in conventional DTC

## 2.5 Summary

In this chapter, the mathematical modeling of four phase SRM using electrical and mechanical equations is presented and the experimental determination of magnetic and torque characteristics is described in detail. Further, the implementation of DTC algorithm for SRM is elaborated. Further, MATLAB simulations are carried out, the simulation results shows that the existence of phase current in the negative torque region and zero torque region results in negative torque generation. Therefore, conventional DTC draws more current from supply, thereby reduces the T/A.



## Chapter 3

# Proposed Direct Torque Control Algorithms

### 3.1 Introduction

The conventional DTC switching pattern does not follow the phase inductance variation. As a result it generates high torque ripple and draws high source current to generate the required electromagnetic torque, that lowers the efficiency of the drive. To address this issues, a DTC with sector reformation and optimized voltage vector selection is proposed in this chapter.

### 3.2 Proposed DTC - 8 Vector 16 Sector Partition Method

The existence of current in any phase during dead zones leads to reduction of T/A in the conventional DTC. In order to avoid this problem, the conventional DTC scheme is modified to enhance T/A by maintaining the current at zero level during dead zones by dividing into 16 sectors and voltage vector selection as shown in Figure [3.1](#). In the conventional DTC scheme described in Chapter 2, the selected vector for the simultaneous increase of torque and flux is the vector existing in the next sector, which is  $67.5^\circ$  ahead of the stator flux vector and the same vector is maintained up to  $45^\circ$  of stator flux vector rotation. In conventional method, as the flux vector is moving, the angle difference between stator flux vector and selected voltage vector decreases from  $67.5^\circ$  to  $22.5^\circ$  at the instant of reaching the next sector. This improper selection voltage vector increase the torque ripple and reduces the T/A ratio. However, the most appropriate voltage vector which is right angles to the stator flux vector and ahead of it, can be selected in order to increase both torque as well as flux for faster dynamic response in the proposed scheme. In the same way, the most appropriate voltage vector which is right

angles to the stator flux vector and lags behind it, can be selected in order to decrease both torque as well as flux. This appropriate selection is realised in the proposed method so that the phase difference between stator flux vector and selected voltage vector at all rotor positions is maintained at  $90^\circ$  approximately under simultaneous decrease or increase in flux and torque. To achieve this, the total  $360^\circ$  space is divided into 16 sectors (each sector of  $22.5^\circ$ ) and voltage vector selection is performed as shown in Table 3.1.

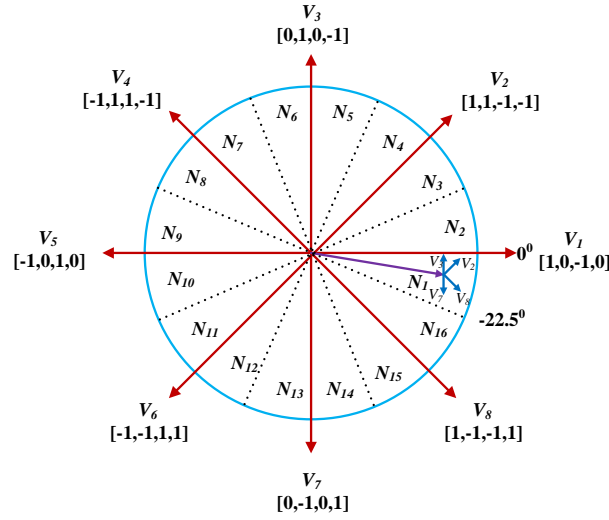


Figure 3.1: Definition of voltage vectors and partition of sectors for proposed 16-sector 8-vector DTC

Table 3.1: Voltage vector selection for proposed 8 vector 16 sector DTC method

Sector	$T \uparrow \psi \uparrow$	$T \uparrow \psi \downarrow$	$T \downarrow \psi \uparrow$	$T \downarrow \psi \downarrow$
$N_1$	$V_2$	$V_3$	$V_8$	$V_7$
$N_2$	$V_3$	$V_4$	$V_1$	$V_8$
$N_3$	$V_3$	$V_4$	$V_1$	$V_8$
$N_4$	$V_4$	$V_5$	$V_2$	$V_1$
$N_5$	$V_4$	$V_5$	$V_2$	$V_1$
$N_6$	$V_5$	$V_6$	$V_3$	$V_2$
$N_7$	$V_5$	$V_6$	$V_3$	$V_2$
$N_8$	$V_6$	$V_7$	$V_4$	$V_3$
$N_9$	$V_6$	$V_7$	$V_4$	$V_3$
$N_{10}$	$V_7$	$V_8$	$V_5$	$V_4$
$N_{11}$	$V_7$	$V_8$	$V_5$	$V_4$
$N_{12}$	$V_8$	$V_1$	$V_6$	$V_5$
$N_{13}$	$V_8$	$V_1$	$V_6$	$V_5$
$N_{14}$	$V_1$	$V_2$	$V_7$	$V_6$
$N_{15}$	$V_1$	$V_2$	$V_7$	$V_6$
$N_{16}$	$V_2$	$V_3$	$V_8$	$V_7$

### 3.2.1 Simulation Results

To validate the performance and effectiveness of the proposed DTC scheme, detailed simulation studies have been carried out on 4-kW four-phase SRM. The simulation studies of the proposed 8 vector 16 sector partition method are performed at torque reference ( $T_{ref}$ ) of 5 Nm, flux linkage  $\psi_{ref} = 0.6$  volt seconds and 500 rpm speed. The electromagnetic torque  $T_{em}$ , phase currents  $i_a$ ,  $i_b$ ,  $i_c$  and  $i_d$ , phase torques  $T_a$ ,  $T_b$ ,  $T_c$  and  $T_d$ , and sectors are shown in Figure 3.2. The phase voltage  $V_a$ , phase current  $i_a$  along with the gate signals for  $S_1$ ,  $S_2$  are shown in Figure 3.3. From Figure 3.4, it can be observed that the current is maintained at zero during zero torque region, thereby the proposed method improves the T/A ratio. The dynamic response comparison of conventional and proposed DTC schemes are presented in Figure 3.5. The proposed DTC has fast dynamic response compared to conventional DTC.

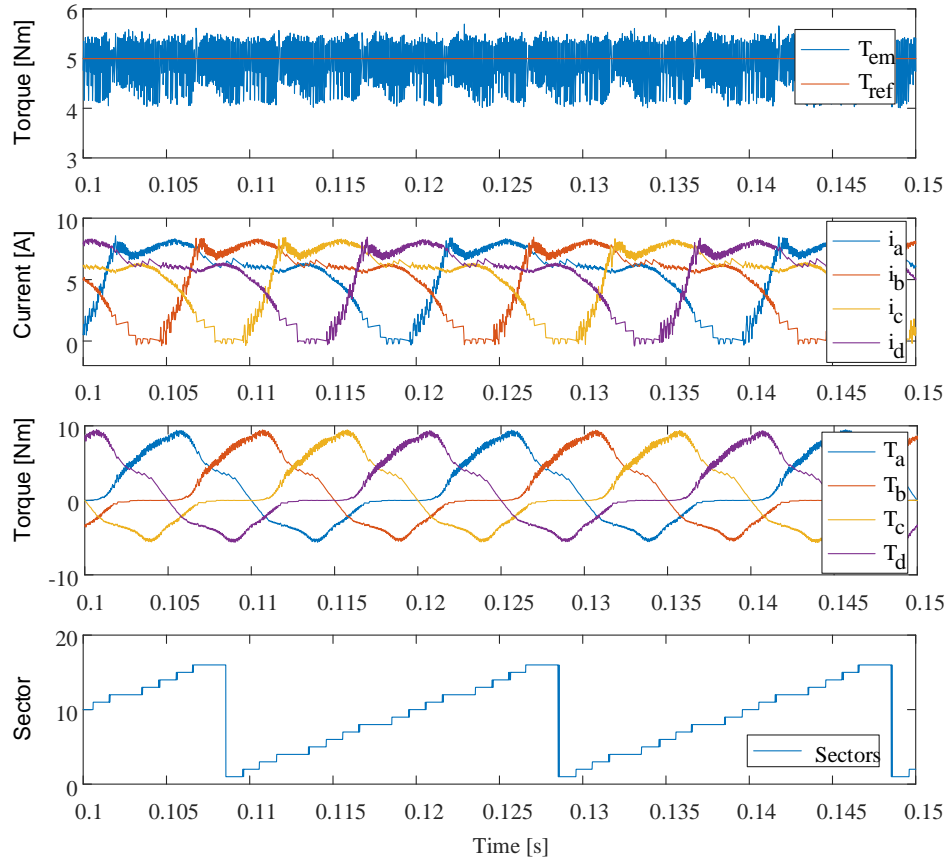


Figure 3.2: Simulation results of electromagnetic torque  $T_{em}$ , phase currents  $i_a$ ,  $i_b$ ,  $i_c$  and  $i_d$ , phase torques  $T_a$ ,  $T_b$ ,  $T_c$  and  $T_d$ , and sectors for proposed 16-sector 8-vector DTC at  $N = 500$  rpm



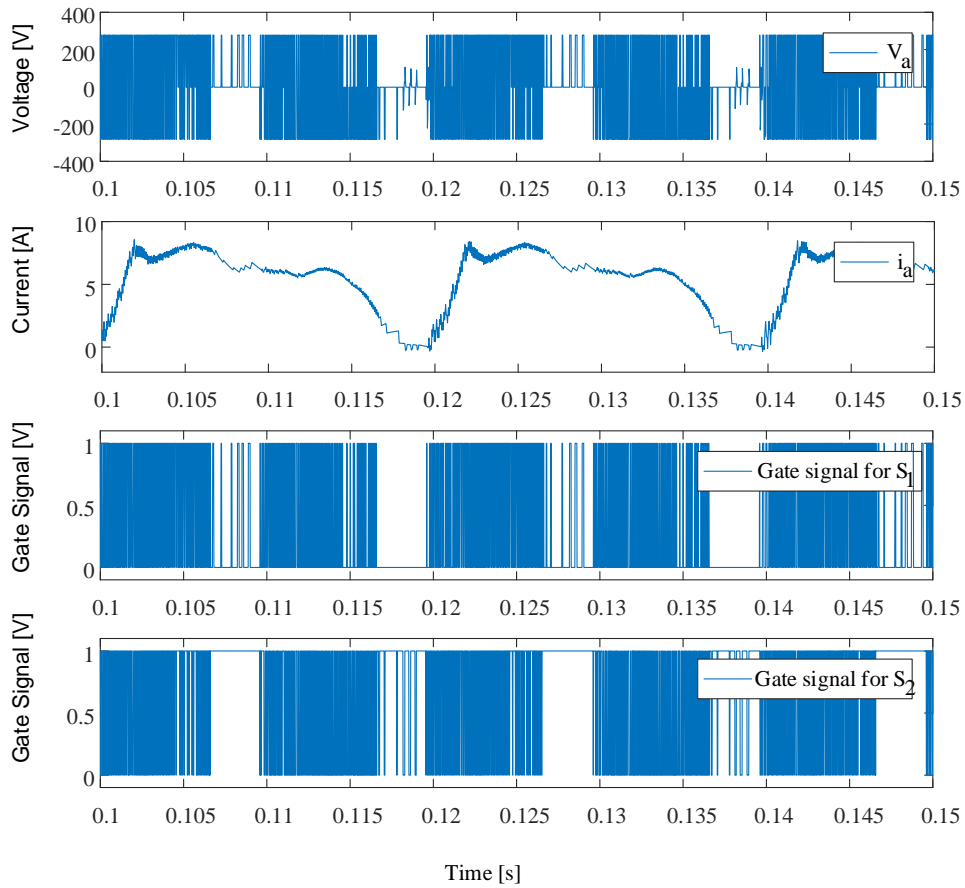


Figure 3.3: Simulation results of the phase voltage  $V_a$ , phase current  $i_a$  and the gate signals of  $S_1$ ,  $S_2$  for proposed DTC at  $N = 500$  rpm

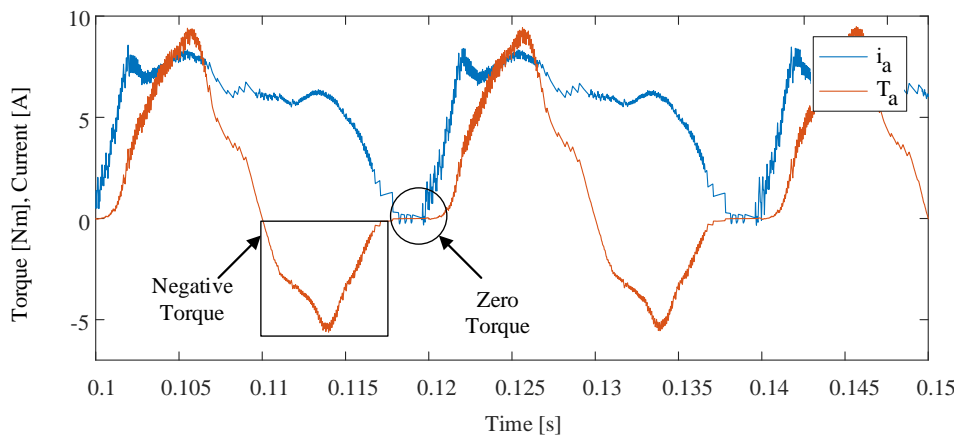


Figure 3.4: Interpretation of zero and negative torque regions in proposed DTC

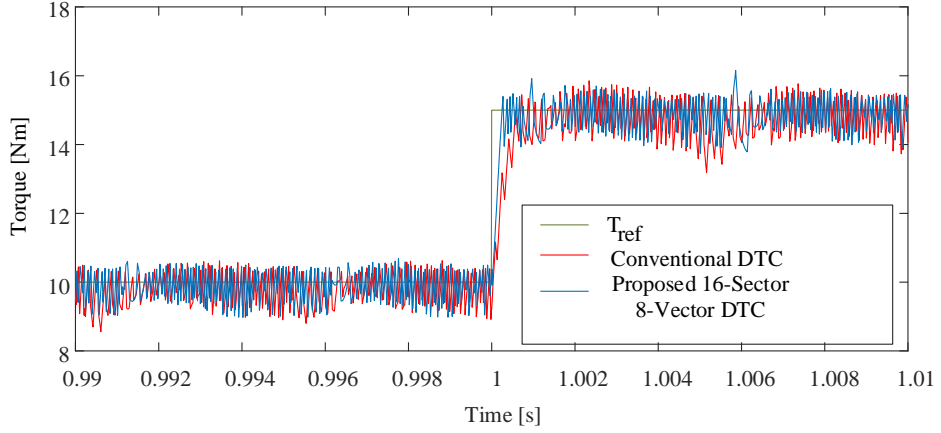


Figure 3.5: Dynamic response comparison of conventional DTC and proposed DTC

The performance of the proposed scheme is compared with the conventional DTC scheme to show the improvement. Figure 3.6 shows the real time results obtained from the real time digital simulator OPAL-RT platform at same operating conditions as MATLAB simulations. It is observed that both the torque and flux are well regulated at their nominal values in the proposed scheme and performs better in minimizing torque ripple as well as improving T/A. In Figure 3.6b(ii), it is shown that the phase current is maintained at zero-level during dead zone (DZ), thereby reducing the source current using the proposed scheme. This is achieved by applying a freewheeling/demagnetizing mode of either an active phase or an incoming phase under positive slope inductance region. As a result, torque ripple is reduced with enhanced T/A ratio compared to the conventional DTC scheme. This scheme does not allow the magnetization state of any phase in the DZ region. Thus, it is observed in Figure 3.6b(iii) that the number of switching of the active switches  $S_1$  and  $S_2$  for ‘A’ phase are less using the proposed DTC, thereby reducing switching frequency as well as switching losses. The comparison of the proposed scheme with the conventional scheme in terms of torque ripple and T/A ratio is listed in Table 3.2. From the analysis, it is concluded that the proposed scheme offers better performance in terms of minimizing torque ripple with enhanced T/A ratio.

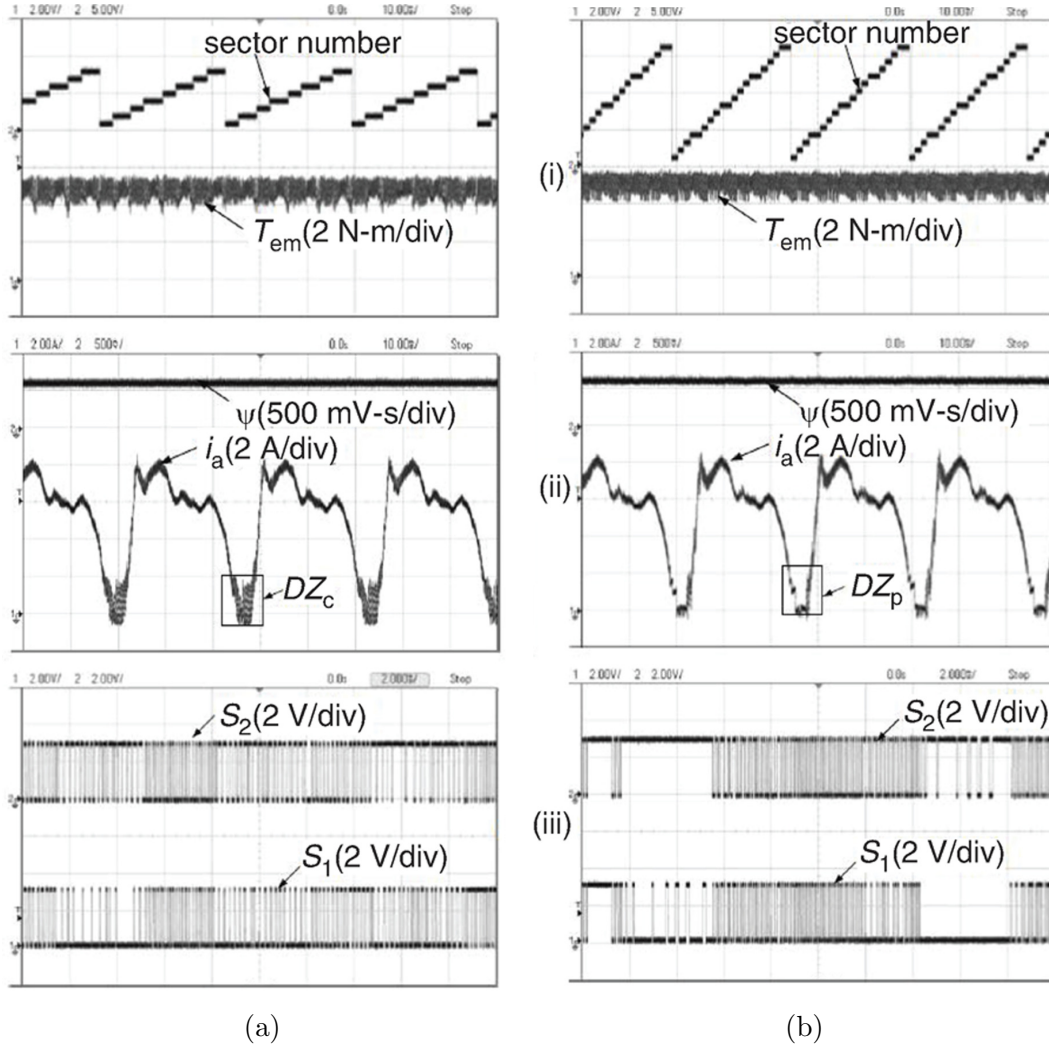


Figure 3.6: Results at 500 rpm (a) Conventional DTC, (b) Proposed 8-vector 16-sector DTC. **Scope i:** CH1: Torque (Nm) and CH2: Sector number; **Scope ii:** CH1:Phase-A current (A) and CH2: Flux linkage; **Scope iii:** CH1: Gate signal for  $S_1$  and CH2: Gate signal for  $S_2$

Table 3.2: Comparison of conventional & proposed 8 vector 16 sector DTC methods

Speed (rpm)	Torque ripple (%)		T/A (Nm/A)	
	Conventional DTC	Proposed DTC	Conventional DTC	Proposed DTC
100	26.8	25.1	0.8107	1.2041
250	31.1	28.1	0.8289	1.1804
500	38.4	33.1	0.8321	1.1071

Even though proposed 8 vector 16 sector DTC eliminates existence of phase

current in zero torque region, The T/A is still low due to generation of negative torque by each phase. This negative torque is produced due to magnetization of outgoing phase in negative inductance slope region.

### 3.3 Proposed DTC – 16 Vectors 16 Sectors Partition Method

In order to avoid the generation of negative torque, 16 vector 16 sector partition method is proposed. In conventional DTC method, the torque can be increased by accelerating the flux linkage vector causing the incoming phase to conduct in the positive torque region, so that the requirement can be fulfilled. Similarly, the torque can be decreased by magnetizing the outgoing phase, which is in the negative torque region, which is at the cost of increased commutations, lower T/A and more switching losses. Furthermore, large input power pulsations occur which is undesirable, especially for applications such as battery-powered electric vehicles.

To address all these issues, in this proposed method eight new vectors are defined for torque decreasing condition as shown in Figure 3.7b. These new eight vectors are proposed such that magnetization of out going phase during negative torque region is completely eliminated thereby improves the efficiency and minimize the torque ripple. The definition of voltage vectors and sector partition is shown in Figure 3.7 and corresponding switching table is listed in Table 3.3. The transition of the phase from demagnetizing mode to magnetizing mode results low T/A for conventional DTC, which can be observed in Figure 3.8. The selection of the voltage vectors using the proposed DTC scheme is presented in Figure 3.9. The proposed method utilizes the new vectors for decrease in torque by replacing all magnetization (1) modes with freewheeling modes (0), thus eliminating the negative torque production. Furthermore, the proposed DTC scheme avoids all (-1) to (+1) switching transitions, i.e. the switching of the phase from demagnetization mode (-1) to magnetization mode (+1) involves switching of both switches of a particular phase, whereas magnetization to freewheeling transition involves only one switch. Therefore, soft chopping with single switch transition can also be achieved using the proposed method.

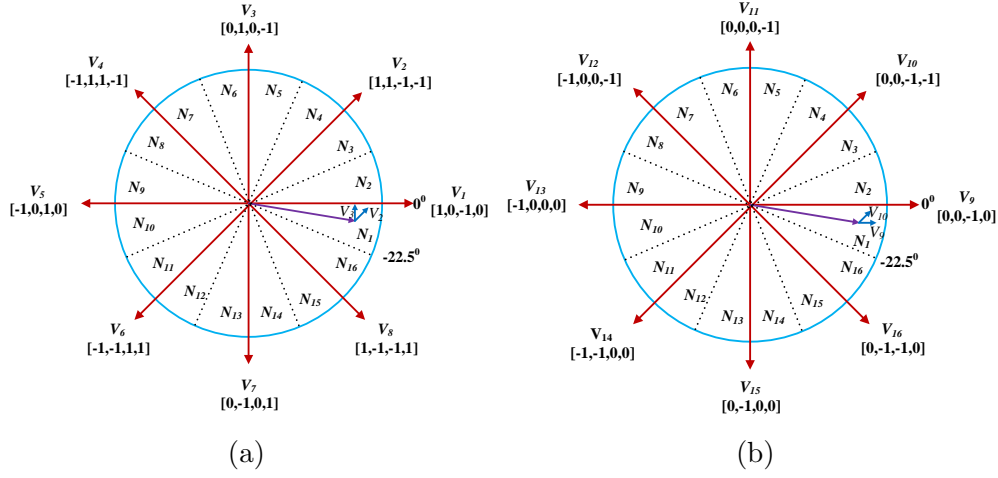


Figure 3.7: Definition of voltage vectors and partition of sectors for proposed 16 vector 16 sector DTC (a) Torque increasing condition, (b) Torque decreasing condition

Table 3.3: Voltage vector selection for proposed 16 vector 16 sector DTC method

Sector	$T \uparrow \psi \uparrow$	$T \uparrow \psi \downarrow$	$T \downarrow \psi \uparrow$	$T \downarrow \psi \downarrow$
$N_1$	$V_2$	$V_3$	$V_{10}$	$V_9$
$N_2$	$V_3$	$V_4$	$V_{11}$	$V_{10}$
$N_3$	$V_3$	$V_4$	$V_{11}$	$V_{10}$
$N_4$	$V_4$	$V_5$	$V_{12}$	$V_{11}$
$N_5$	$V_4$	$V_5$	$V_{12}$	$V_{11}$
$N_6$	$V_5$	$V_6$	$V_{13}$	$V_{12}$
$N_7$	$V_5$	$V_6$	$V_{13}$	$V_{12}$
$N_8$	$V_6$	$V_7$	$V_{14}$	$V_{13}$
$N_9$	$V_6$	$V_7$	$V_{14}$	$V_{13}$
$N_{10}$	$V_7$	$V_8$	$V_{15}$	$V_{14}$
$N_{11}$	$V_7$	$V_8$	$V_{15}$	$V_{14}$
$N_{12}$	$V_8$	$V_1$	$V_{16}$	$V_{15}$
$N_{13}$	$V_8$	$V_1$	$V_{16}$	$V_{15}$
$N_{14}$	$V_1$	$V_2$	$V_9$	$V_{16}$
$N_{15}$	$V_1$	$V_2$	$V_9$	$V_{16}$
$N_{16}$	$V_2$	$V_3$	$V_{10}$	$V_9$

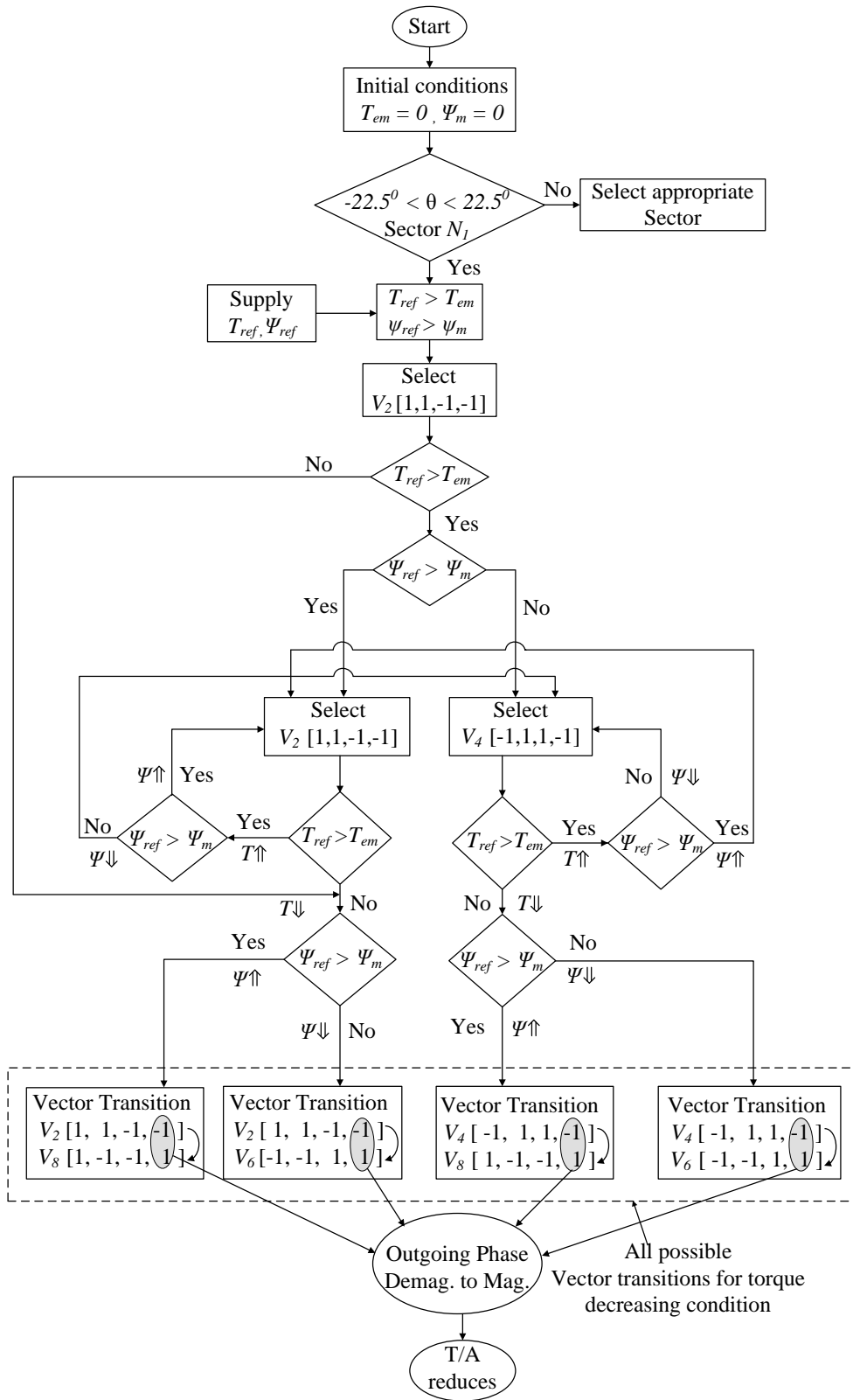


Figure 3.8: Flowchart of the conventional DTC

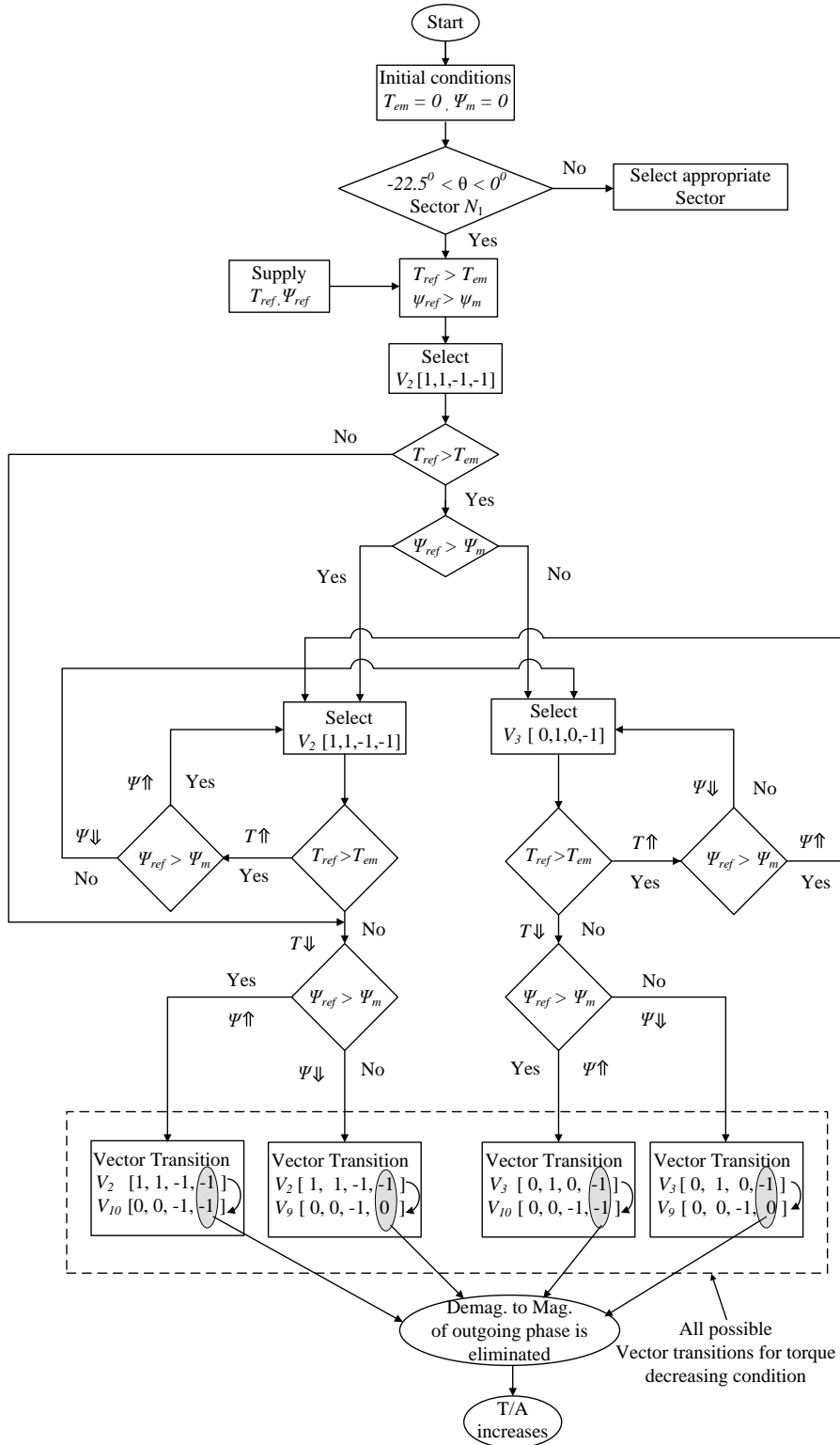


Figure 3.9: Flowchart of the proposed 16 vector 16 sector DTC

### 3.3.1 Simulation Results

The results obtained using the proposed scheme under steady-state as well as dynamic conditions are illustrated and compared with the conventional DTC. Here, waveforms of only two phases ‘A’ & ‘C’ are plotted for clear understanding and visualization. Figures 3.10 and 3.11 show the simulated waveforms of the conventional DTC strategy for a reference torque of 15 Nm at 250 and 750 rpm respectively. From these results, we can observe the extension of the phase current and negative phase torque existence in conventional DTC. This phase negative torque can be completely eliminated in the SRM drive using the proposed DTC strategy as shown in Figures 3.12 and 3.13.

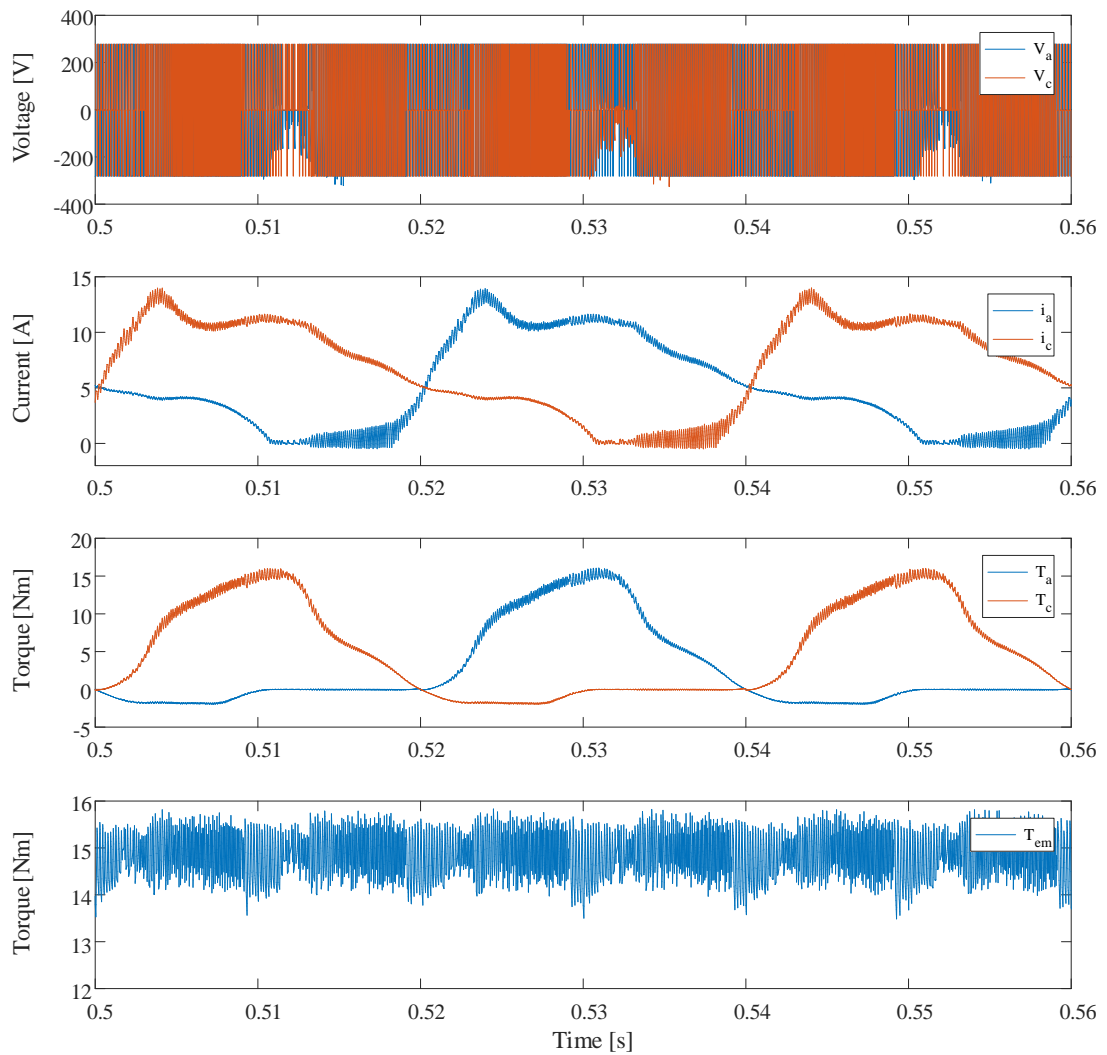


Figure 3.10: Steady-state simulation results of phase voltages  $V_a$  &  $V_c$ , phase currents  $i_a$  &  $i_c$ , phase torques  $T_a$  &  $T_c$ , and total electromagnetic torque  $T_{em}$  for conventional DTC at 250 rpm



The torque dips observed during the phase commutation in the conventional DTC are shown in Figures 3.10 and 3.11. These torque dips are reduced using the proposed DTC as depicted in Figures 3.12 and 3.13. Thus, the desired torque is well regulated at their reference value with an improved T/A ratio using the proposed DTC strategy and outperforms the conventional DTC strategy in terms of torque ripple and T/A ratio under low and high speeds.

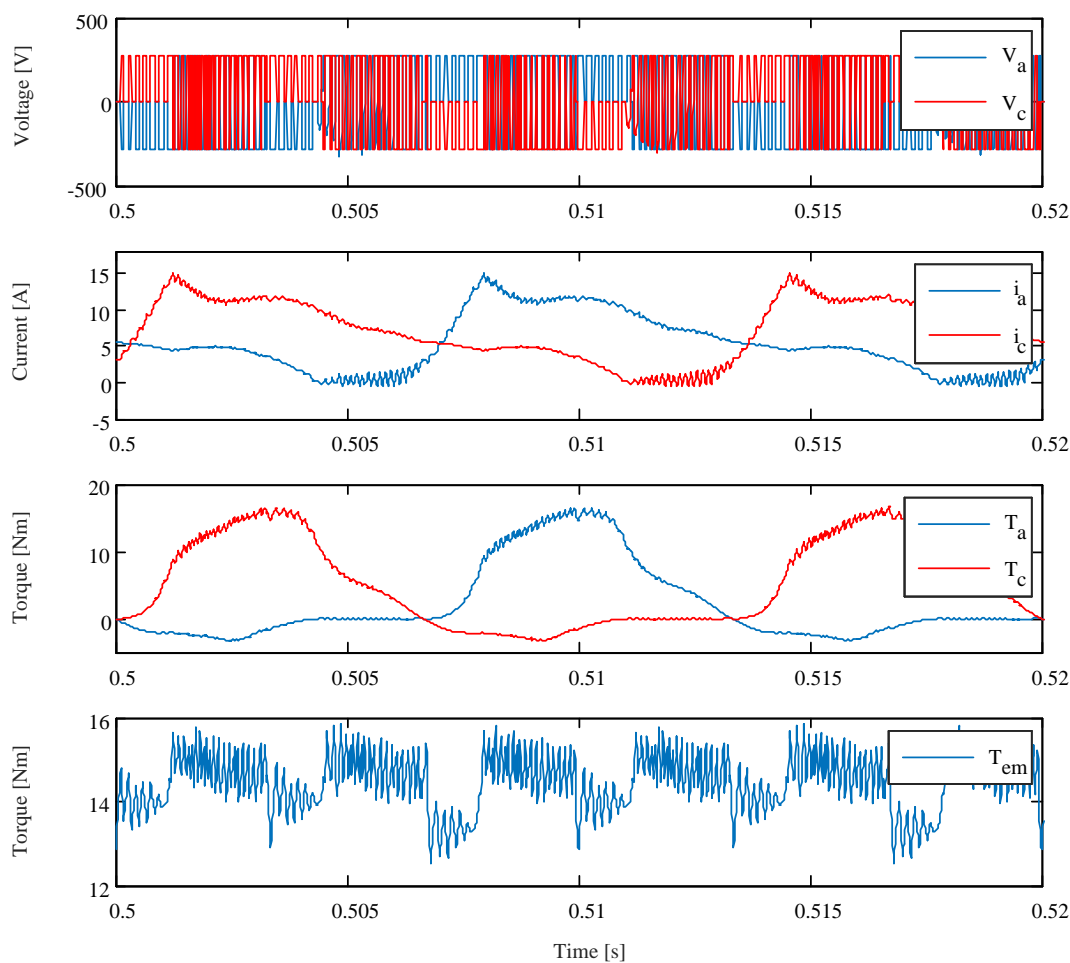


Figure 3.11: Steady-state simulation results of phase voltages  $V_a$  &  $V_c$ , phase currents  $i_a$  &  $i_c$ , phase torques  $T_a$  &  $T_c$ , and total electromagnetic torque  $T_{em}$  for conventional DTC at 750 rpm

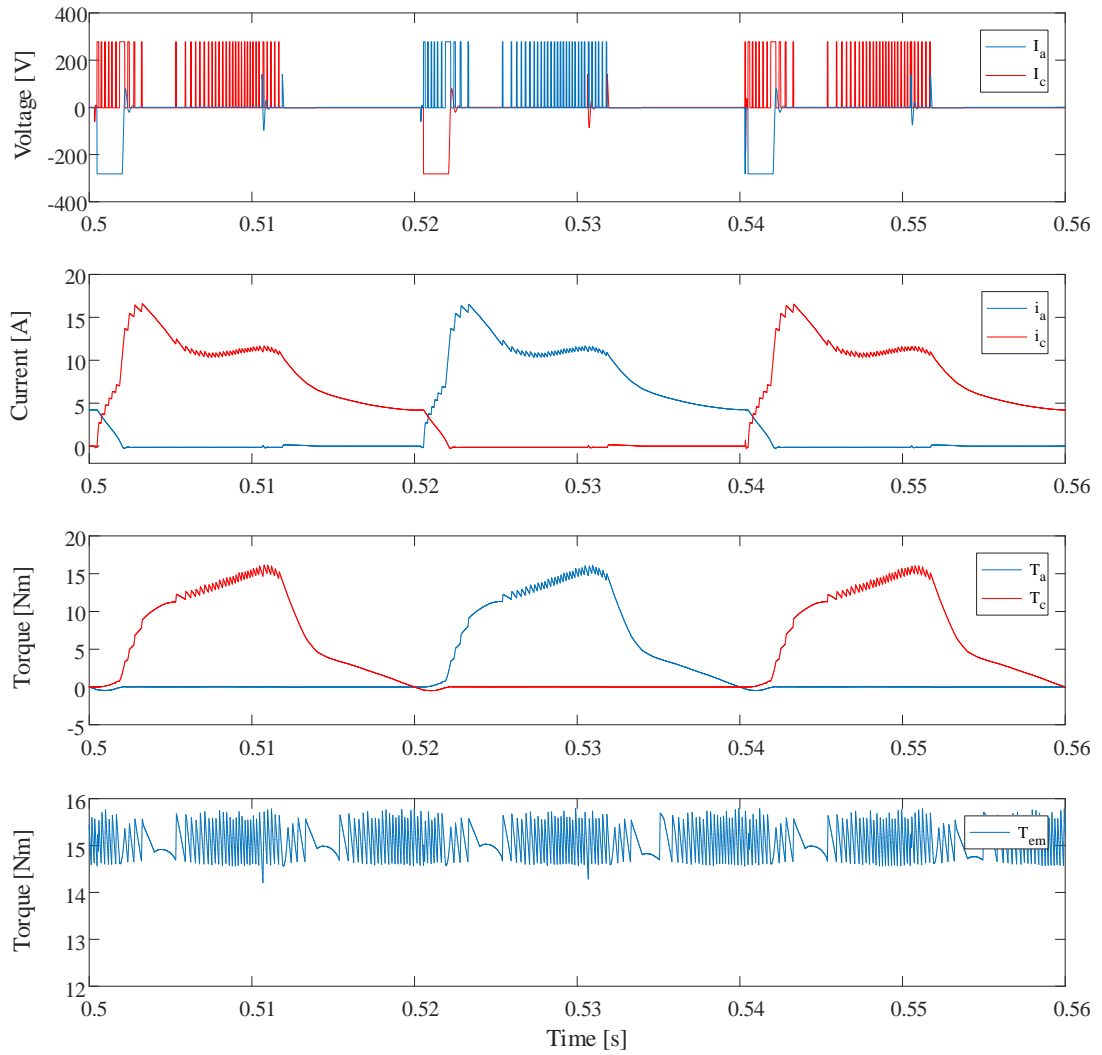


Figure 3.12: Steady-state simulation results of phase voltages  $V_a$  &  $V_c$ , phase currents  $i_a$  &  $i_c$ , phase torques  $T_a$  &  $T_c$ , and total electromagnetic torque  $T_{em}$  for proposed 16 vector 16 sector DTC at 250 rpm

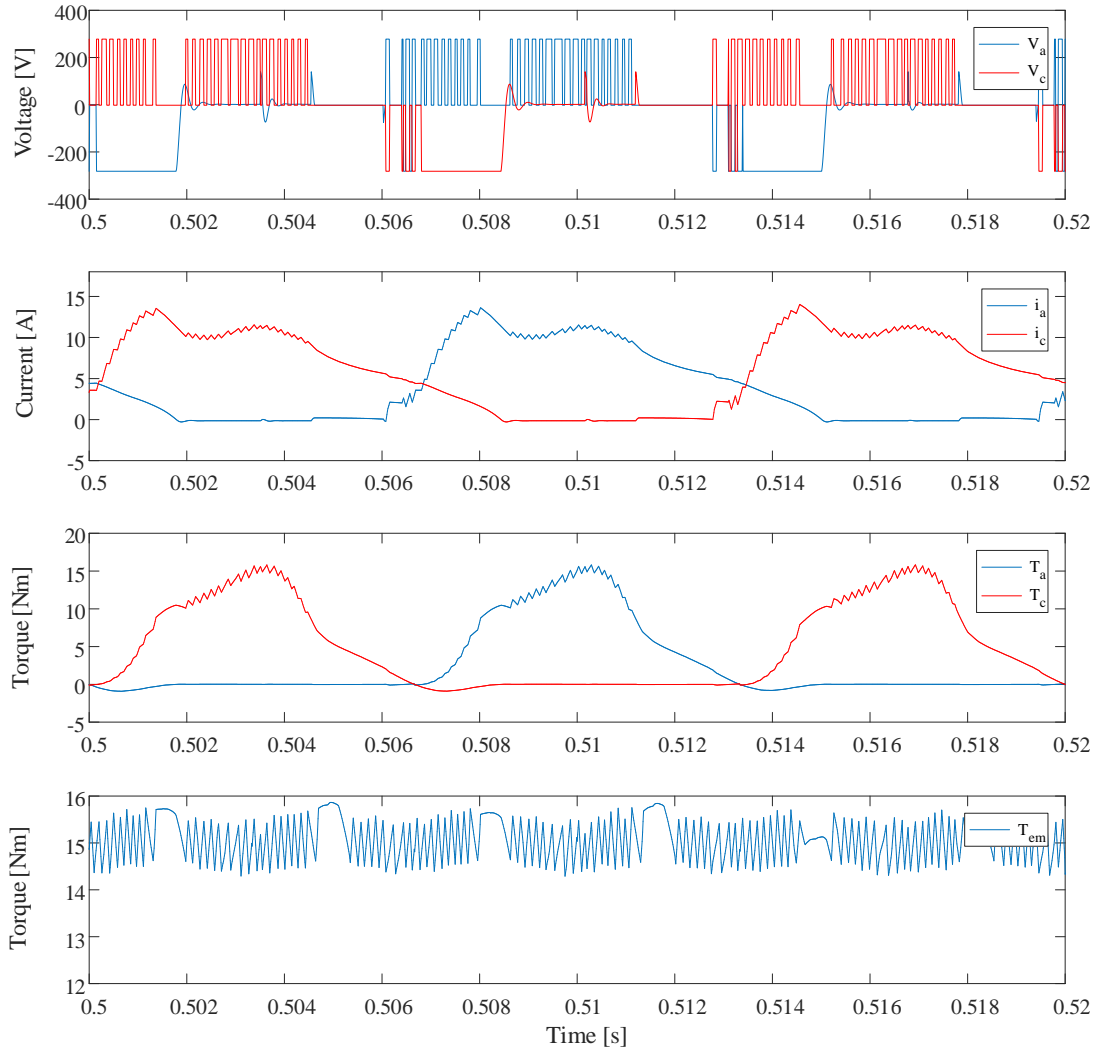


Figure 3.13: Steady-state simulation results of phase voltages  $V_a$  &  $V_c$ , phase currents  $i_a$  &  $i_c$ , phase torques  $T_a$  &  $T_c$ , and total electromagnetic torque  $T_{em}$  for proposed 16 vector 16 sector DTC at 750 rpm

The dynamic performance of the SRM drive with the proposed DTC scheme is validated by changing the torque reference during acceleration and deceleration modes. To validate the dynamic performance, torque reference ( $T_{ref}$ ) is changed from 10 to 15 Nm at 1 s and from 15 to 5 Nm at 1.2 s. It is observed that, the proposed 16 sector 16 vector DTC is able to track the  $T_{ref}$  effectively in comparison to the conventional DTC, as shown in Figures 3.14 and 3.15. This is due to selecting vectors which are orthogonal to the stator flux linkage vector. The dynamic response of conventional DTC has a delay in settling as well as the undershoots at the new reference torques. Therefore, the proposed DTC strategy exhibits fast dynamic performance with reduced torque pulsations under different

torque references.

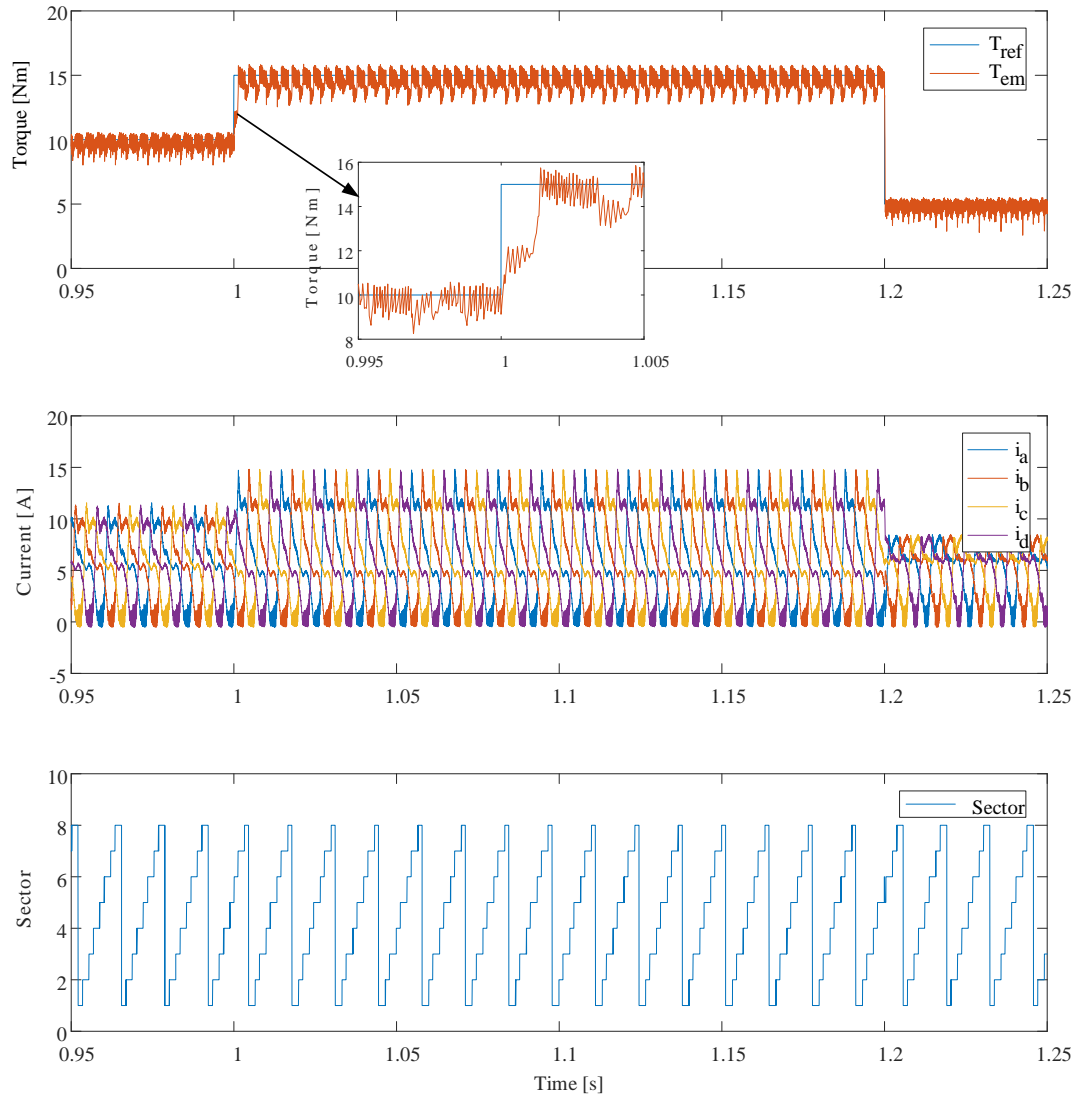


Figure 3.14: Dynamic performance of conventional DTC at 750 rpm

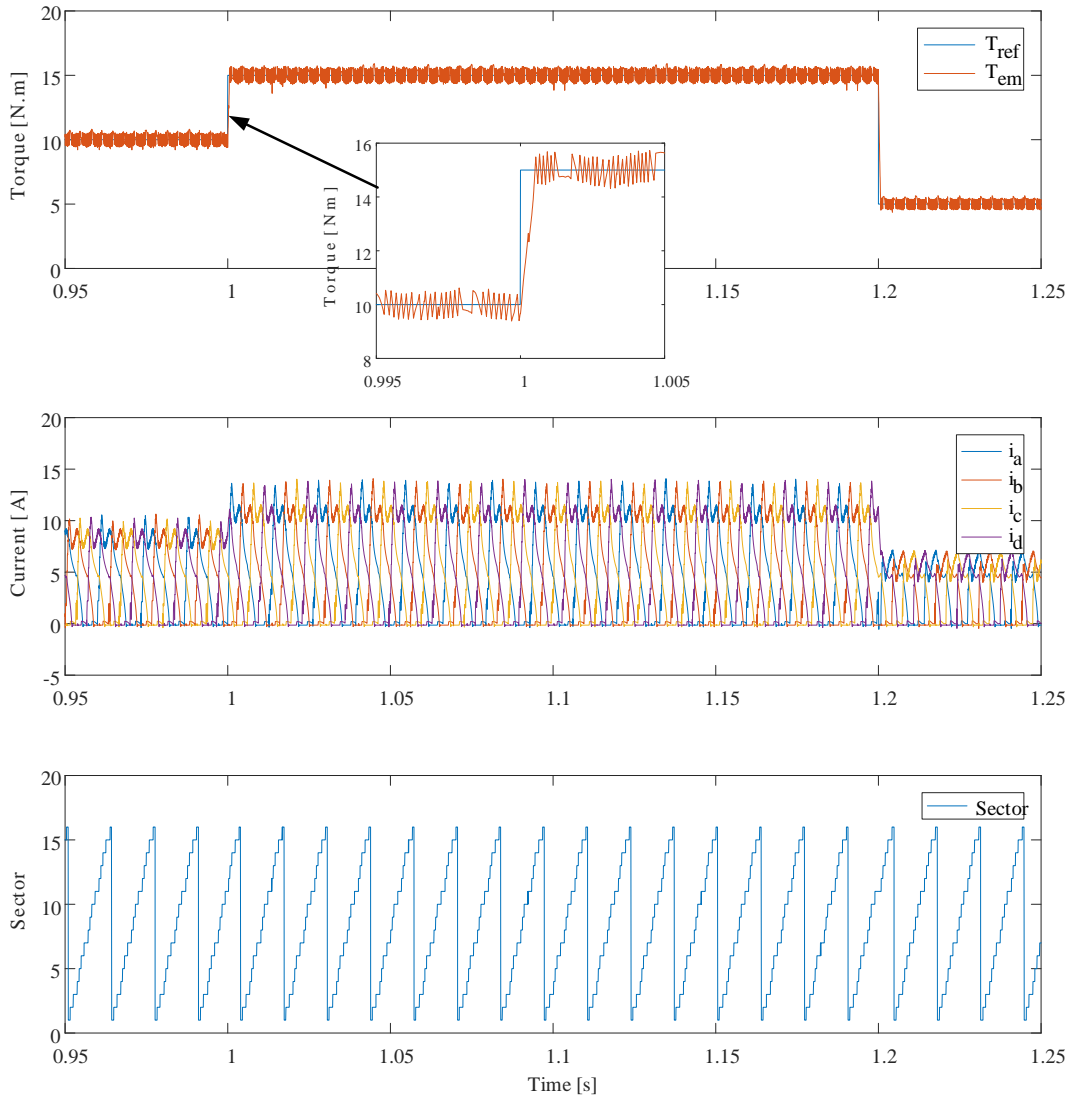


Figure 3.15: Dynamic performance of proposed DTC at 750 rpm

### 3.3.2 Real Time Simulations with OPAL-RT

The proposed DTC strategy is also verified through real-time studies. The proposed and conventional DTC schemes are implemented on an OPAL-RT-based digital controller (OP5142) with  $50 \mu\text{sec}$  sampling time. The motor parameters and the testing conditions of a real-time system are similar to the simulation studies. The real-time results shown in Figures [3.16a](#) and [3.16b](#) are found to be in concurrence with the corresponding MATLAB simulation results in terms of electro-magnetic torque, phase torque, phase current and rotor angle. As shown in Figure [3.16b\(i\)](#), the extension of the phase current and phase negative torque are completely eliminated under the negative inductance

slope region. Thus, the proposed drive improves T/A in the SRM drive, thereby enhancing the drive efficiency.

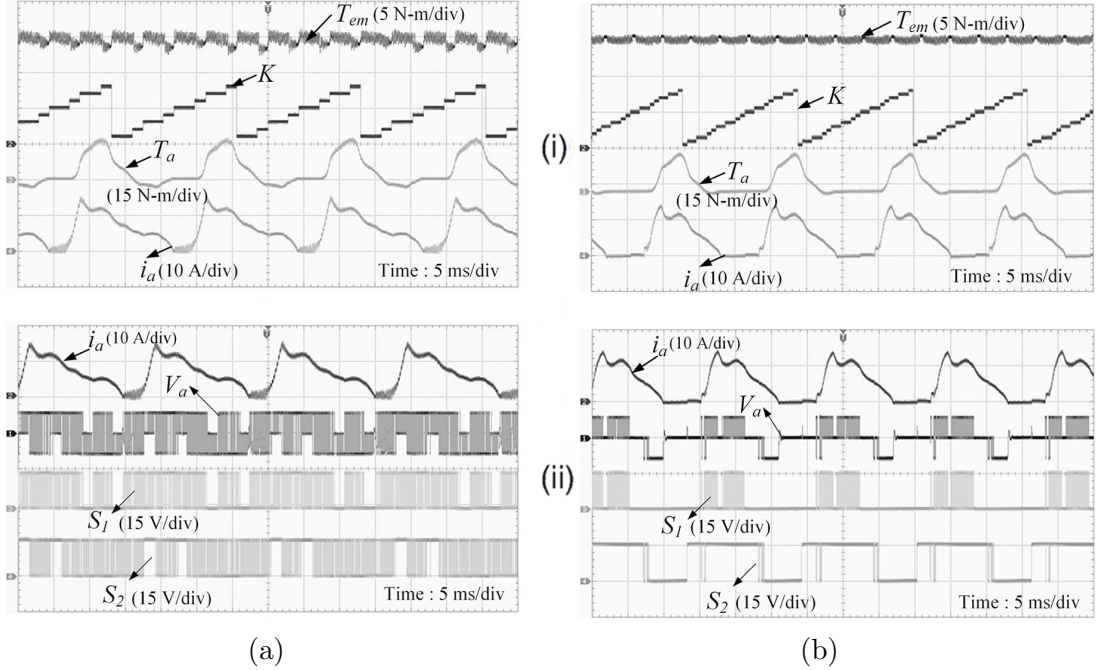


Figure 3.16: Real-time results at 750 rpm (a) Conventional DTC, (b) Proposed DTC : **Scope i**: CH1: Total torque (Nm), CH2: Sector number, CH3: Phase torque (Nm) and CH4: Phase current (A); **Scope ii**: CH1: Phase current (A), CH2: Phase voltage (V), CH3: Gate signal for  $S_1$  and CH4: Gate signal  $S_2$ .

## 3.4 Performance Analysis of DTC Schemes

### 3.4.1 Torque Ripple Analysis

Torque dip occurs at the point of overlap during phase commutation, which is usually expressed in the form of torque ripple.

Torque ripple is evaluated using equation 1.8 under both the DTC schemes at low and high speeds. With the application of the proposed DTC scheme, torque dips are reduced significantly during phase commutation as depicted in Figures 3.12, 3.13 and 3.16b. It is also observed that, the torque ripple is reduced by 32% and 36% in proposed DTC at 250 rpm and 750 rpm respectively when compared with conventional DTC.

### 3.4.2 T/A and Copper Loss

The magnitude of the phase current in the inductance decreasing region determines the amount of generated negative phase torque. The proposed DTC scheme completely eliminates the phase current in the negative torque region,

thereby improves the drive efficiency. In the case of SRM drives, it is usually expressed in terms of T/A.

It is observed that the proposed DTC scheme improves T/A ratio by 71.91% and 4.73% at 250 and 750 rpm respectively. The copper losses can be evaluated as follows:

$$P_c = \sum_{j=1}^m (i_{j\text{rms}}^2 \cdot r_j) \quad (3.1)$$

where  $r_j$  is the phase AC resistance and  $i_{j\text{rms}}$  is the rms value of the  $j^{\text{th}}$  phase current. Copper losses are determined using the Equation 3.1 for both schemes under different speeds. The performance analysis of both schemes in terms of copper losses is shown in Figure 3.17. It is noticed that the copper losses are reduced by 11.56% and 15.92% using the proposed drive at 250 and 750 rpm, respectively.

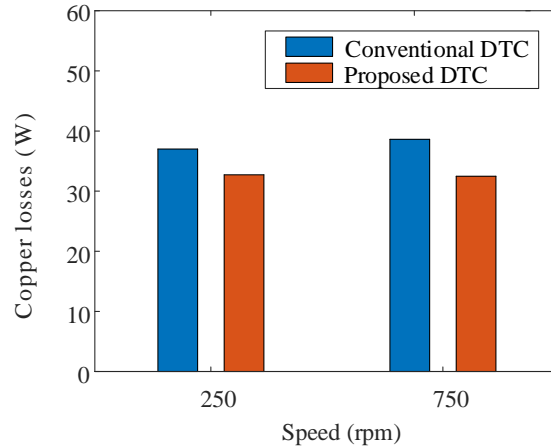


Figure 3.17: Comparison of per-phase copper losses under the conventional and proposed DTC schemes

### 3.4.3 Current Stress on Power Devices and the Number of Commutations

Power devices have been found to be the most fragile components and are prone to failure due to varying current and voltage stress. Therefore, it is essential to analyze the stress on the devices that are subjected to different control strategies. Figure 3.18 and Figure 3.19 shows the current distribution on each device of AHBC per phase under the conventional and proposed DTC strategies at 750 rpm respectively.

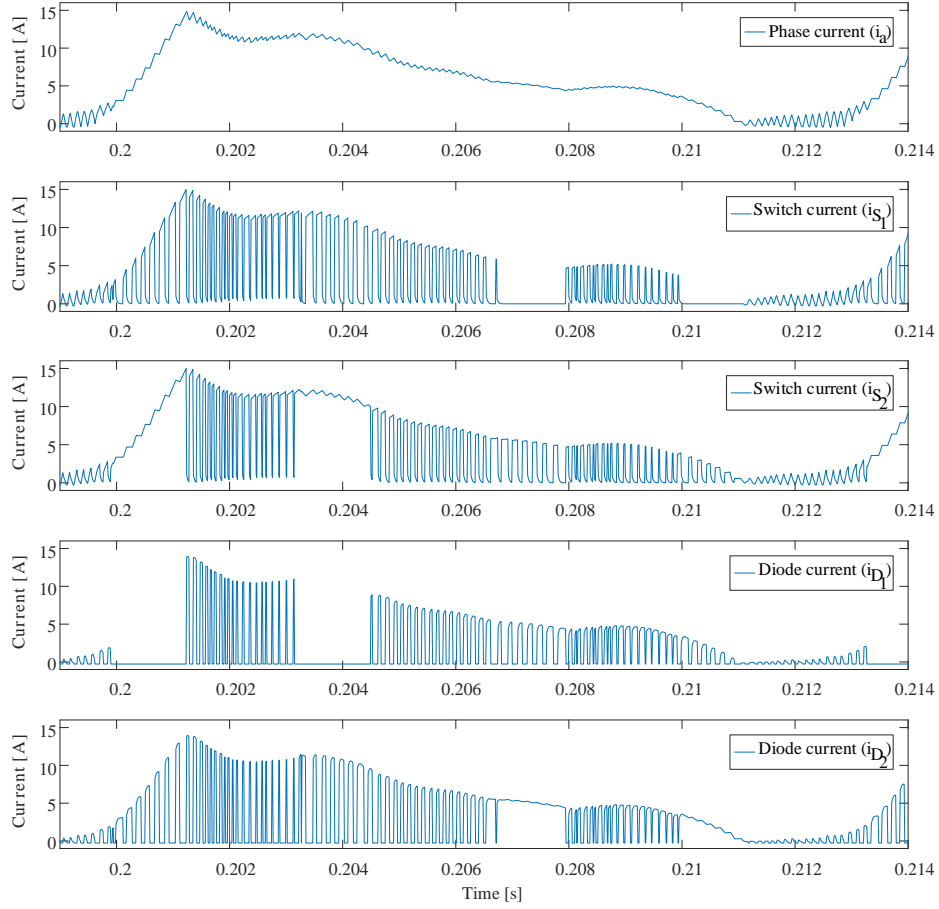


Figure 3.18: Device stress under the conventional DTC scheme

It is observed that the switching of the devices is significantly reduced in proposed DTC compared with conventional DTC. Alternatively, it can also be analyzed through the number of commutations in one electrical period. The number of commutations of the switch for one electrical cycle can be calculated using a digital counter circuit. In this method, the counter is incremented by one whenever the rising edge of the gate signal is detected. The difference between the counter count at the starting point and endpoint of the cycle gives the number of commutations. The block diagram of the digital counter to evaluate the number of commutations per switch is shown in Figure 3.20. Both per-phase active devices ( $s_1$  and  $s_2$ ) are switched at 43 and 32 times in one-fundamental cycle of the proposed DTC method, whereas in the conventional DTC, both devices are switched at 587 and 177 times at 250 and 750 rpm respectively. The lesser number of commutations implies lower switching losses of the converter, which is observed in both simulation and real-time results. Therefore, average switching frequency of the proposed SRM drive is significantly reduced in



comparison to the conventional DTC-based drive.

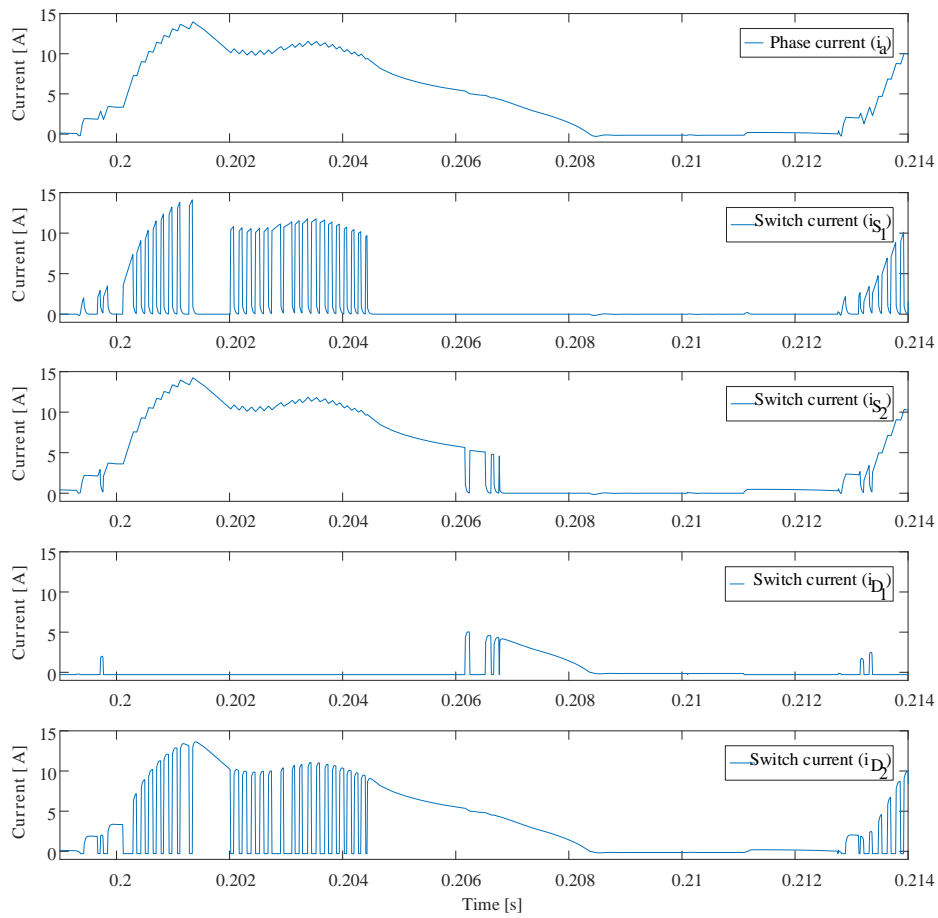


Figure 3.19: Device stress under the proposed DTC scheme

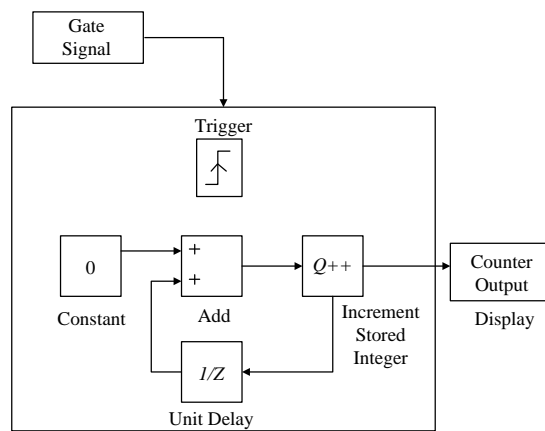


Figure 3.20: Block diagram for evaluating the number of commutations

### 3.4.4 Power Loss Analysis

It is shown that the number of commutations is limited using the proposed DTC scheme by eliminating the magnetization of the phase in the negative torque region. Even though the number of commutations is reduced, the conduction time of power diodes increases. As already discussed, the reduction in RMS current to generate same electromagnetic torque reduces the converter conduction losses. Therefore, it is required to evaluate the power loss of the AHBC. The total power losses  $P_{Total}$  of per phase AHBC are given by

$$P_{Total} = P_{L-S_1} + P_{L-D_1} + P_{L-S_2} + P_{L-D_2} \quad (3.2)$$

where  $P_{L-S_1}$ ,  $P_{L-D_1}$ ,  $P_{L-S_2}$  and  $P_{L-D_2}$  are the power losses of the upper switch, upper diode, lower switch and lower diode, respectively. The total power loss of a power switching device (S) and diode (D) is the sum of conduction losses and switching losses (turn-on loss and turn-off loss/recovery loss). The conduction loss of the switch/diode can be given by

$$P_{cond, S/D} = \frac{1}{T} \int_0^T V_{on, S/D} \times i(t) dt \quad (3.3)$$

The conduction loss of ( $P_{cond, S/D}$ ) switch and diode can be calculated from their forward voltage drop ( $V_{on, S/D}$ ) and their instantaneous current  $i(t)$ . The device characteristics are developed using the curve-fitting tool in the MATLAB by considering the electrical and thermal characteristics of Semikron IGBT SKM75GAL123D/SKM75GAR123D for one phase of AHBC. The derived conduction loss equations of the switch (S) and diode (D) from the curve fitting analysis ( [Drofenik and Kolar, 2005](#), [Venkataramanaiah and Suresh, 2018](#) ) are listed as

$$P_{S, 25^\circ C} = 0.02365 * i_S(t)^2 + 1.551 * i_S(t) - 0.8995 \quad (3.4)$$

$$P_{S, 125^\circ C} = 0.02876 * i_S(t)^2 + 1.914 * i_S(t) - 2.452 \quad (3.5)$$

$$P_{D, 25^\circ C} = 0.01521 * i_D(t)^2 + 1.245 * i_D(t) - 0.2321 \quad (3.6)$$

$$P_{D,125^{\circ}\text{C}} = 0.01485 * i_D(t)^2 + 1.06 * i_D(t) - 0.8451 \quad (3.7)$$

The second-order polynomial equations are developed for conduction power losses at temperatures (T) are given by

$$P_S(i_c, T) = (0.0224 + 0.000058 * T) * i_S(t)^2 + (1.46025 + 0.00363 * T) * i_S(t) - (0.511375 + 0.015525 * T) \quad (3.8)$$

$$P_D(i_D, T) = 0.0153 * i_D(t)^2 + (1.2913 - 0.0019 * T) * i_D(t)(0.0789 + 0.0061 * T) \quad (3.9)$$

The conduction losses are calculated using the Equations [3.3](#) - [3.9](#) as per methodology shown in Figure [3.23a](#). The switching losses of the switch (S) and diode (D) are

$$P_{\text{Sw-S}} = \frac{1}{T} \sum_{j=1}^N [E_{\text{on}}(j) + E_{\text{off}}(j)] \quad (3.10)$$

$$P_{\text{Rec-D}} = \frac{1}{T} \sum_{j=1}^N [E_{\text{rec}}(j)] \quad (3.11)$$

where  $E_{\text{on}}$  and  $E_{\text{off}}$  are the turn-on and turn-off energies of switch, respectively.  $E_{\text{rec}}$  represents the recovery energy of the diode. The data sheet provides  $E_{\text{on}}$ ,  $E_{\text{off}}$  and  $E_{\text{rec}}$  losses versus switch/diode current curves that describe the current dependency of switching losses. Other dependent factors of switching losses are blocking voltage and junction temperature. The switching loss factor can be obtained by dividing total energy losses with switch/diode current represented as

$$K_{S/D} = \frac{E_{\text{total}}}{I_{S/D}} (\mu\text{Ws/A}) \quad (3.12)$$

The derived polynomial equations for switching loss factor from the selected switch data sheet are expressed as

$$K_S(i_S) = 0.0001487 * i_S(t)^3 - 0.03366 * i_S(t)^2 + 3.224 * i_S(t) + 170.3 \quad (3.13)$$

$$K_D(i_D) = -0.0007726 * i_D(t)^2 - 0.436 * i_D(t) + 65.53 \quad (3.14)$$

$K_S(i_S)$  is the switching loss factor of IGBT and  $K_D(i_D)$  is the switching loss factor of a diode. The switching loss evaluation methodology adopted is shown in Figure 3.23b. Once the conduction and switching losses are calculated, then the total losses for all devices are evaluated as shown in Figure 3.23c. The converter loss distribution comparison of the conventional and the proposed DTC strategies at 250 and 750 rpm are shown in Figures 3.21 and 3.22.

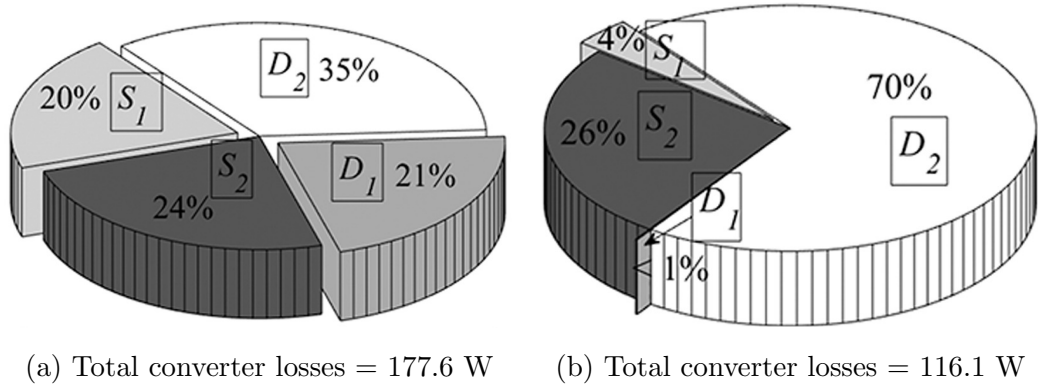


Figure 3.21: Converter power loss analysis (a) Conventional DTC at 250 rpm, (b) Proposed DTC at 250 rpm

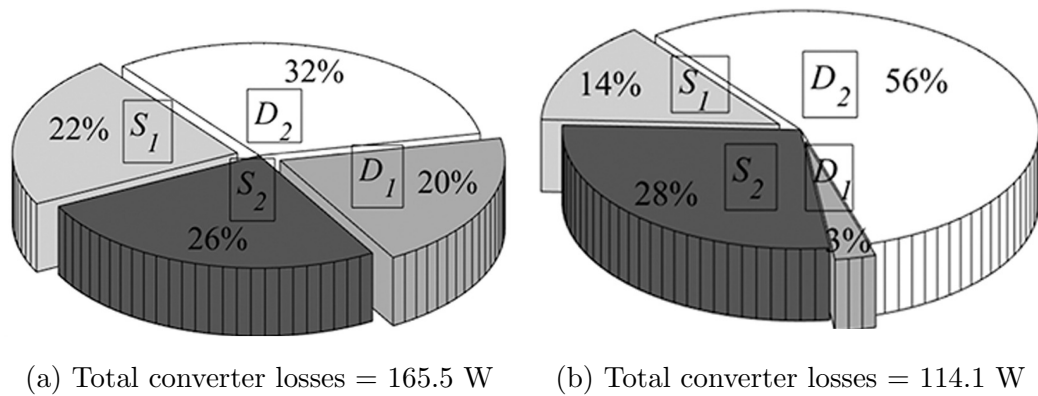


Figure 3.22: Converter power loss analysis (a) Conventional DTC at 750 rpm, (b) Proposed DTC at 750 rpm

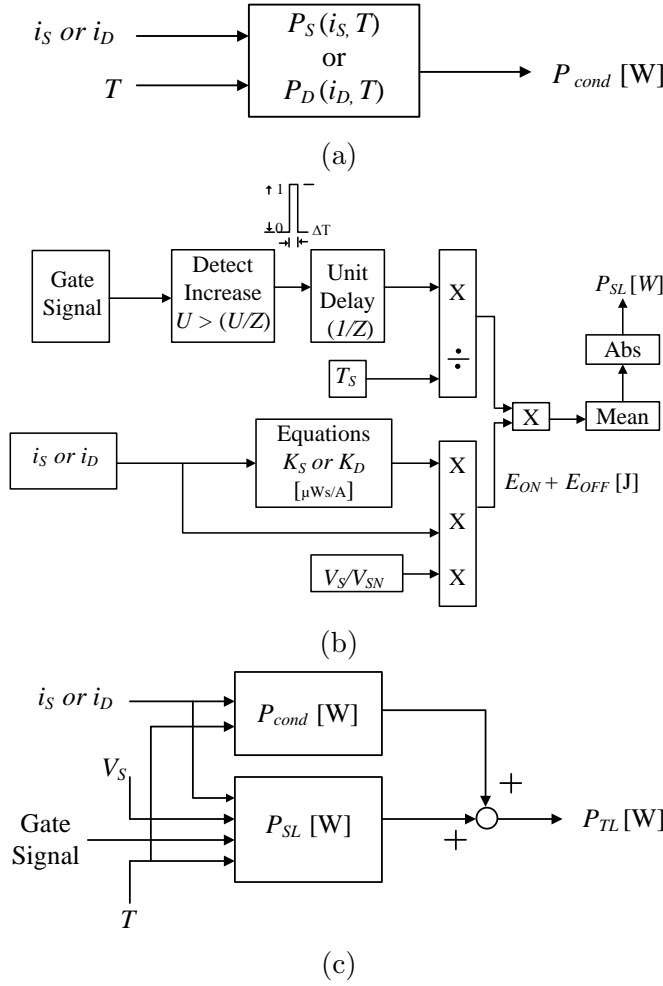
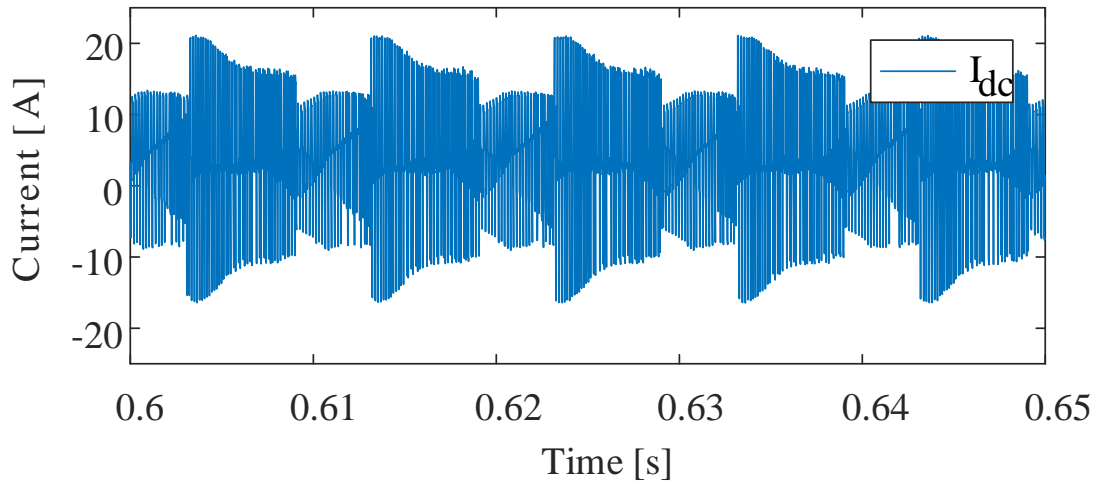


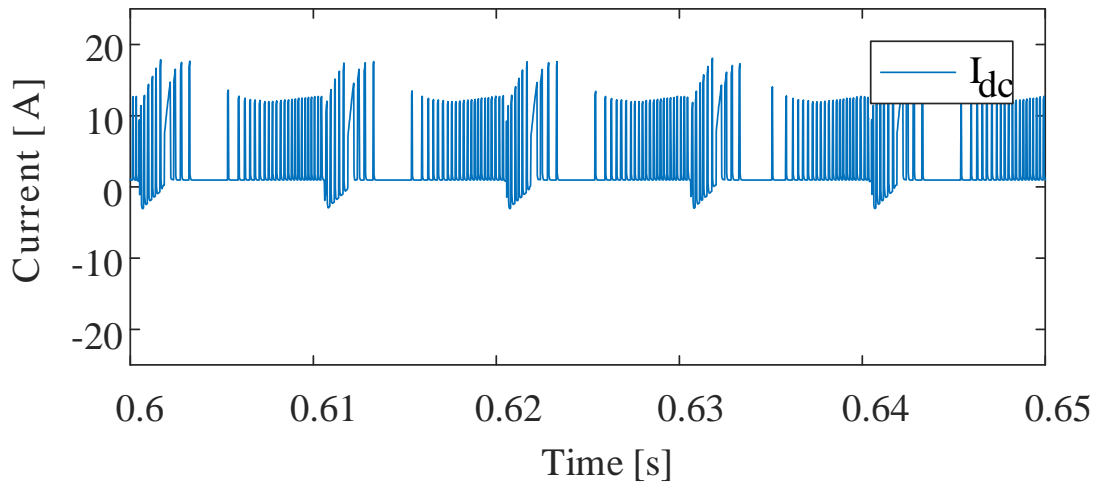
Figure 3.23: Block diagram of power loss evaluation methodology (a) Conduction losses, (b) Switching losses, (c) Total losses

### 3.4.5 Input Power Fluctuations

Due to non-linear characteristics and phase commutation of SRM, there are large input power fluctuations when transferring energy from the *dc* source to the SRM. Therefore, large current fluctuations occur at the input side considering the stiff *dc* source. In battery-powered electric vehicles, the battery lifetime is highly influenced by the ripple current. One way to avoid such power fluctuations, is the use of large capacitors parallel to the battery. In order to compare the performance of both the schemes, same capacitor value is considered and their results at 250 rpm are shown in Figure 3.24. It is observed that the proposed method reduces fluctuations in the source current, which improves the life of the battery in the battery-powered electrified vehicles.



(a)



(b)

Figure 3.24: Comparison of source current at 250 rpm (a) Conventional DTC, (b) Proposed DTC

### 3.4.6 Comparison Summary of the Proposed DTC Scheme with Conventional DTC

The comparison summary between these methods in terms of torque ripple, torque per ampere, source current and number of commutations are listed in Table 3.4. Overall, the proposed DTC method outperforms the conventional DTC method especially at lower speeds. The comparative analysis between the proposed DTC and the conventional DTC are summarized in Table 3.5.

Table 3.4: Comparison of conventional & proposed 16 vectors 16 sectors DTC methods

Speed (rpm)	Torque ripple (%)		T/A (Nm/A)		Supply Current(rms)(A)		Number of commutations	
	Conventional DTC	Proposed DTC	Conventional DTC	Proposed DTC	Conventional DTC	Proposed DTC	Conventional DTC	Proposed DTC
250	15.66	10.66	1.570	2.699	9.454	5.611	587	43
500	19.20	13.66	1.529	2.057	9.627	7.311	309	39
700	21.93	14.02	1.578	1.647	9.15	9.129	177	32

Table 3.5: Summary of comparative analysis of proposed and conventional DTC scheme

Scheme attributes	Conventional DTC	Proposed DTC
sector partition method	eight	sixteen
voltage vector used	eight	sixteen
torque ripple	high	low
T/A ratio	low	high
source current ripple	high	low
copper losses	high	low
switching losses	high	low
number of commutations	high	low
device current stress	high	low
device voltage stress	high	low
battery life	low	high
capacitor requirement	high	low
efficiency	low	high

### 3.5 Summary

In this chapter, a new DTC algorithm for a four-phase SRM drive with improved efficiency is proposed. In this scheme, a sixteen sector partition method is employed and the most appropriate voltage vectors are selected to regulate the desired torque with minimal torque pulsations. The proposed strategy effectively eliminates the instantaneous negative torque generated by the outgoing phase during phase commutation. Thus, the net T/A ratio is significantly increased and the torque ripple is minimized. The real-time results show that the proposed DTC scheme improves the drive efficiency in comparison to the conventional DTC scheme.

# Chapter 4

## Proposed Phase Current Reconstruction Algorithm

### 4.1 Introduction

Acquiring the phase currents is critical to protect and estimate flux in DTC controlled SRM drives. The conventional phase current measurement scheme is shown in Figure 4.1. One current sensor per phase, analog-to-digital channels and the corresponding signal-conditioning circuits are required for digital control, consequently increasing the system cost with an increased phase number. Hence, it entails to reconstruct phase currents using reduced number of current sensors to enhance reliability as well as to reduce the cost.

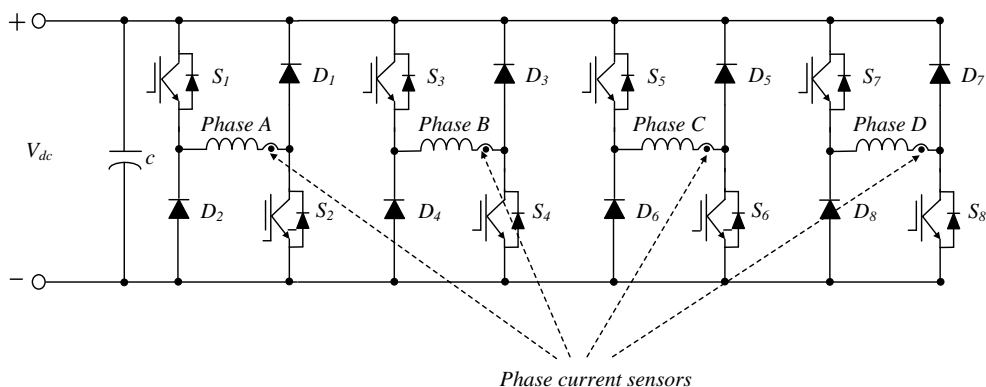


Figure 4.1: Conventional current measurement scheme with individual hall-effect sensors

Several advanced phase current detection and reconstruction methods have been proposed in the literature, which are basically classified as with and without pulse injection methods. ( [Gan et al., 2014], [Gan et al., 2017], [Sun et al., 2017], [Sun et al., 2018], [Kjaer and Gallegos-Lopez, 1998], [Gan et al., 2015], [Gan et al., 2016b], [Gan et al., 2016a], [Han et al., 2017], [Cheng et al., 2021], [Gan



et al., 2018], [Ronanki et al., 2020]). Most of these approaches are developed using one or two current sensors under current chopping control (CCC) technique. The detailed discussions on the methodology of the major phase current reconstruction methods are provided in the following sections.

## 4.2 Phase Current Reconstruction Methods

### 4.2.1 Phase Current Reconstruction from DC-Link Current using High-Frequency Pulse Injection

In this phase current detection scheme ([Gan et al., 2014]), a *dc*-link current sensor is used. As shown in Figure 4.2, all the positive poles of down side diodes are connected to the down *dc*-link and all the sources of the down switches are connected to the down *dc*-link through a current sensor. As the diodes are not connected to *dc*-link, demagnetization currents are eliminated in the measurement and only excitation currents of all the phases are measured by sampled *dc*-link current sensor.

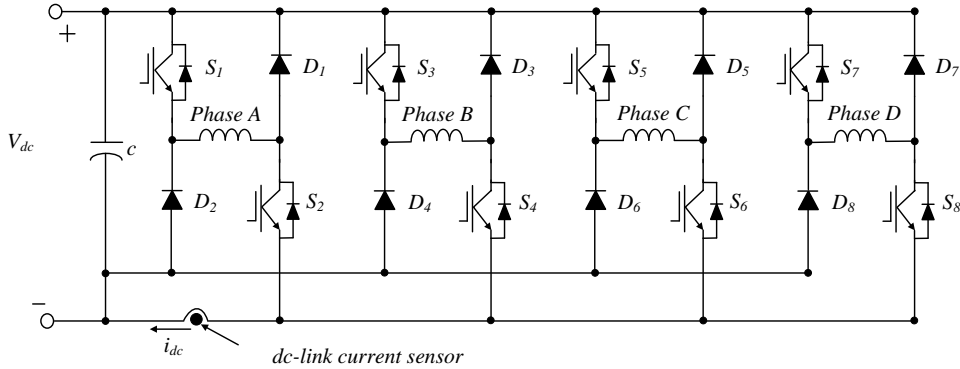


Figure 4.2: Single sensor based phase current measurement scheme

The *dc*-link current can be expressed in terms of phase currents and switching functions as

$$i_{dc} = i_a S_2 + i_b S_4 + i_c S_6 + i_d S_8 \quad (4.1)$$

The relationship between the *dc*-link current and the converter switching states in the phase excitation sequence is given in Table 4.1. If the two phase currents are not overlapped as shown in Figure 4.3, the *dc*-link current is same as phase excitation current in the phase turn-on region and all phase currents can

be obtained by multiplying the  $dc$ -link current with the driving gate signal of exciting phase without any pulse injection. Generally, two phase currents are overlapped at phase commutation region to avoid high torque pulsation in current controlled SRM drives.

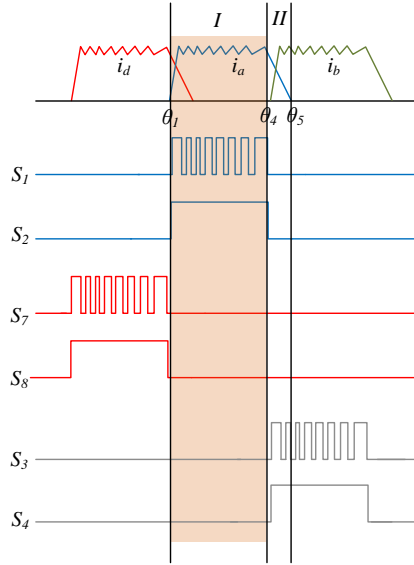


Figure 4.3: Two phase currents non overlap in the turn-on region

From the Figure 4.4, it is shown that phase currents A & D are overlapped in the region I. Therefore, the  $dc$ -link current in the region I is the sum of the phase A and phase D currents. In this region, if down switch of phase A is off, the  $dc$ -link current is only the phase D current and the dc link current is only phase A current, if down switch of phase D is off. Therefore the  $dc$ -link current in the overlapped region of  $\theta_1 - \theta_4$  can be expressed as

$$i_{dc} = i_a \text{ if } S_2 = 1, S_8 = 0 \quad (4.2)$$

$$i_{dc} = i_d \text{ if } S_2 = 0, S_8 = 1 \quad (4.3)$$

In this pulse injection method, The phase A current can be reconstructed by injecting high frequency pulse with large duty cycle in down switches of phases D & phase B in the overlapping regions I & III respectively. The injected high frequency signal denoted as PWM<sub>1</sub>. Similarly, phase D current in region I and phase B current in region III can be reconstructed by injecting another phase shifted high frequency pulse with same duty cycle into down switch of phase A. This phase shifted high frequency signal is denoted as PWM<sub>2</sub>. The phase shift

between the PWM<sub>1</sub> and PWM<sub>2</sub> is defined as half period of PWM<sub>1</sub> and denoted as  $t_{shift}$ . The method leads to voltage penalty due to pulse injection.

$$t_{shift} = \frac{(t_{on} + t_{off})}{2} \quad (4.4)$$

Where  $t_{on}$  and  $t_{off}$  are the turn-on and turn-off times of high frequency pulse.

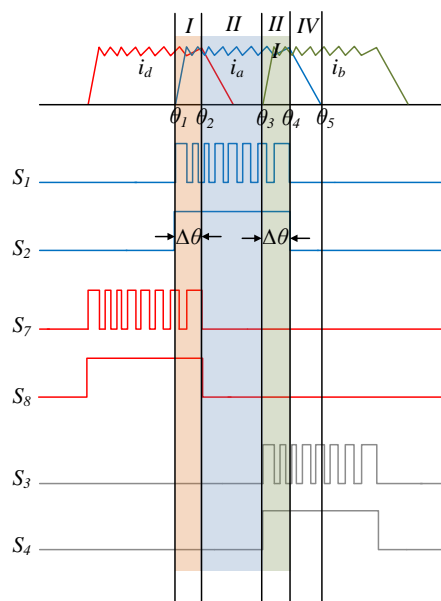


Figure 4.4: Two phase currents overlap in the turn-on region

Table 4.1: Relationship between dc-link current and switching states

$S_2$	$S_4$	$S_2$	$S_4$	$i_{dc}$
1	0	0	0	$i_a$
1	1	0	0	$i_a + i_b$
0	1	0	0	$i_b$
0	1	1	0	$i_b + i_c$
0	0	1	0	$i_c$
0	0	1	1	$i_c + i_d$
0	0	0	1	$i_d$
1	0	0	1	$i_d + i_a$

## 4.2.2 Split Dual Bus Method for Phase Current Detection

In this method ( [Gan et al., 2017](#)), instead of using individual current sensor in each phase, only two sensors are used for phase current detection using split dual bus system as shown in Figure [4.5](#).

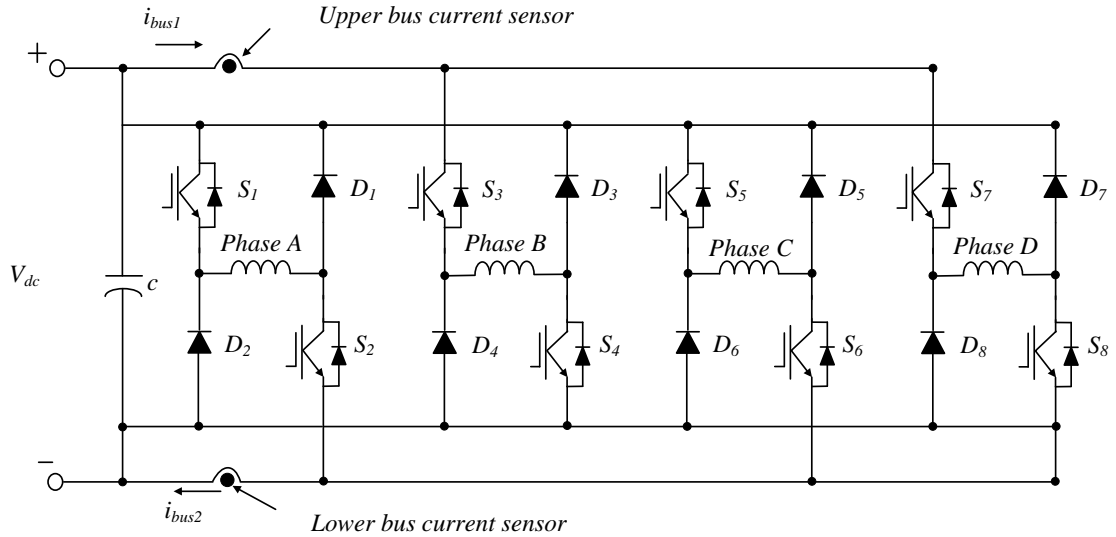


Figure 4.5: Two sensor based current measurement scheme with split dual bus line

In this method, upper and lower bus lines are split into two parts. One current sensor is placed in split upper DC bus which connects the collectors of the upper switches of phase B and D, another current sensor is placed in the split lower DC bus which connects the emitters of the lower switches of phases A and C and kept the other connections remains same as shown in Figure [4.5](#). In this topology, only bus lines are split without any additional components and utilizes only two sensors to detect the phase currents which not only reduces the number of current sensors required compared with traditional method but also provides prominent solution for voltage penalty problem. Furthermore, the need of pulse injection is eliminated in this method compared to one sensor method. In this method, demagnetization current of each phase are not flowing through the current sensors, thereby sensors detect only magnetizing and freewheeling current, which makes the current measurement and separation much easier. Current regulation doesn't require demagnetizing current. Therefore, this method effectively reconstruct the phase currents only with two current sensors. The relationship between phase currents and bus currents is shown in below Table [4.2](#).

Table 4.2: Relationship between bus currents and switching states

$S_1$	$S_3$	$S_5$	$S_7$	$i_{bus1}$	$i_{bus2}$
1	0	0	0	0	$i_a$
1	1	0	0	$i_b$	$i_a$
0	1	0	0	$i_b$	0
0	1	1	0	$i_b$	$i_c$
0	0	1	0	0	$i_c$
0	0	1	1	$i_d$	$i_c$
0	0	0	1	$i_d$	0
1	0	0	1	$i_d$	$i_a$

As per the connection, the currents of phases B & D always go through the upper bus sensor where as lower bus sensor always carries phase currents A & C. However, current controlled SRM drive allows the overlapping of any two phase currents at any time. For example phase currents A & B are overlapped for a certain duration, the phase A current directly obtained from lower bus sensor and phase B current is same as upper bus sensor current. Similar way, any phase current can be determined at any time from two bus current sensors. The upper and lower bus currents can be expressed in terms of phase currents as given in equations [4.5](#) & [4.6](#).

$$i_{bus1} = i_b \cdot S_3 + i_d \cdot S_7 \quad (4.5)$$

$$i_{bus2} = i_a \cdot S_2 + i_c \cdot S_6 \quad (4.6)$$

The reconstructed phase currents  $i_{a,re}$ ,  $i_{b,re}$ ,  $i_{c,re}$ ,  $i_{d,re}$  can be obtained from relationship between bus currents and switching signals as per the equations given below.

$$i_{a,re} = i_{bus2} \cdot S_2 \quad (4.7)$$

$$i_{b,re} = i_{bus1} \cdot S_3 \quad (4.8)$$

$$i_{c,re} = i_{bus2} \cdot S_6 \quad (4.9)$$

$$i_{d,re} = i_{bus1} \cdot S_7 \quad (4.10)$$

### 4.2.3 Phase Current Reconstruction using Improved Converter Topology

In hysteresis current control method, only conduction of consecutive phases are overlapping. Phase currents A & C never conduct simultaneously. Therefore the switches  $S_1$  &  $S_3$ , diode  $D_2$  commonly used for phases A & C as shown in Figure 4.6. Similarly, the switches  $S_5$  &  $S_7$ , diode  $D_5$  commonly used for phases B & D. In this method (Sun et al., 2017), phase currents are reconstructed by using single dc link current sensor with advanced PWM pulse injection without voltage penalty.

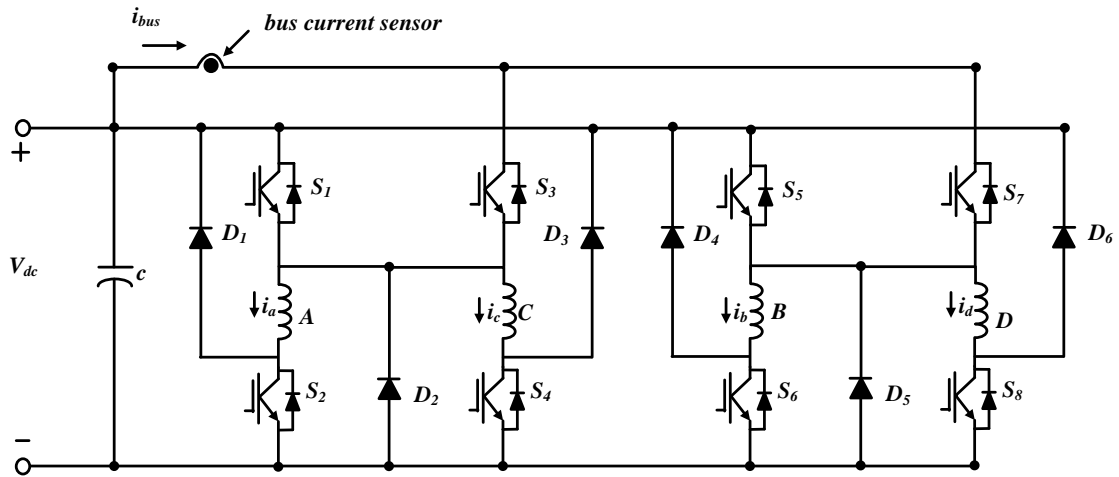


Figure 4.6: Single sensor based phase current measurement system with improved converter topology

This topology excludes the demagnetization current from  $dc$  link current by connecting the cathode terminals of all the upper diodes to upper  $dc$  link. When there is no overlap between adjacent phases, the phase currents are directly measured by sampling the  $dc$  link current during the corresponding conduction region. PWM pulse injection technique is used to separate the phase currents when phase currents are overlapping. During the excitation mode of phase A & B, phase A current is separated from the  $dc$  link current by changing the conduction from switch  $S_7$  to  $S_5$ . Similarly, the phase B current is separated from the  $dc$  link current by changing the conduction from  $S_3$  to  $S_1$ . Similarly during one phase is conducting and other one is freewheeling, the phase currents are separated by changing conduction between  $S_7$  and  $S_5$  for phase A current reconstruction and changing the conduction between switches  $S_3$  and  $S_1$  for phase B current reconstruction.

## 4.2.4 Multiplexed Current Sensors Based Phase Current Detection Scheme

Multiplexed current sensor based phase current detection scheme is shown in Figure 4.7. (Sun et al., 2018). In this multiplexing current sensor scheme, phases A & C currents measured by single current sensor by multiplexing both in same sensor as phase currents A & C will not overlap as shown in Figure 4.8. Similarly, Phase currents B & D can be measured using single sensor by multiplexing into single sensor. The relationship between sensor currents and phase currents in all four regions are given in Table 4.3. This method doesn't require any converter modifications and pulse injection.

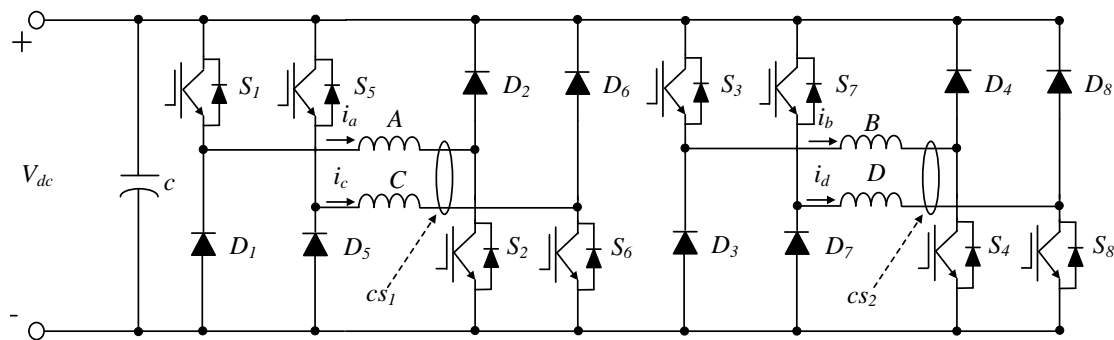


Figure 4.7: Multiplexed current detection scheme for four-phase SRM

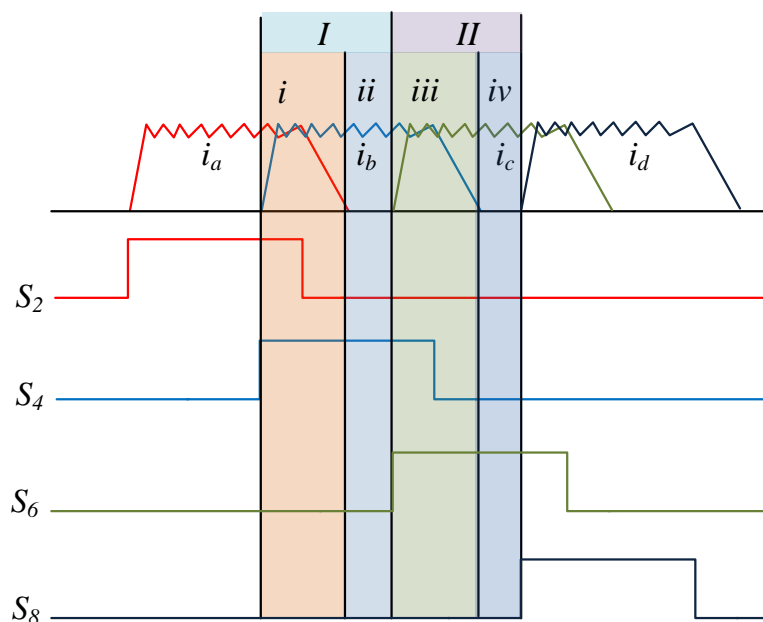


Figure 4.8: Two phase currents overlap in the turn-on region

Table 4.3: Relationship between sensor currents and phase currents

Region	$I_1$	$I_2$	$i_a$	$i_b$	$i_c$	$i_d$
i	$i_a$	$i_b$	$I_1$	$I_2$	0	0
ii	0	$i_b$	0	$I_2$	0	0
iii	$i_c$	$i_b$	0	$I_2$	$I_1$	0
iv	$i_c$	0	0	0	$I_1$	0

### 4.3 Proposed Phase Current Reconstruction Algorithm

The block diagram of the proposed phase current reconstruction algorithm for four-phase SRM drive, as shown in Figure 4.9 consists of an SRM, power converter, drive circuit, position measurement unit, current and voltage measuring circuits. Each phase conducts for all eight sectors in conventional DTC as shown in Figure 4.10a due to long-tail currents. Due to simultaneous conduction of all phases over the eight-sector region, phase current detection from the dc-link current is not possible. The elimination of tail current in the proposed 16 vector 16 sector DTC creates the scope for reduction of current sensors instead of using one sensor per phase. To identify the region, the 16 sectors are divided into four regions such that at least one phase current should be zero in each region as illustrated in Figure 4.10b. It can be seen that three phase currents are overlapping at any given time i.e., each phase current is maintained at zero for at least four sectors. The remaining three phase currents can be extracted from three sensors output using a simple algebraic equations. The output of the three sensors in the four regions is listed in Table 4.4.



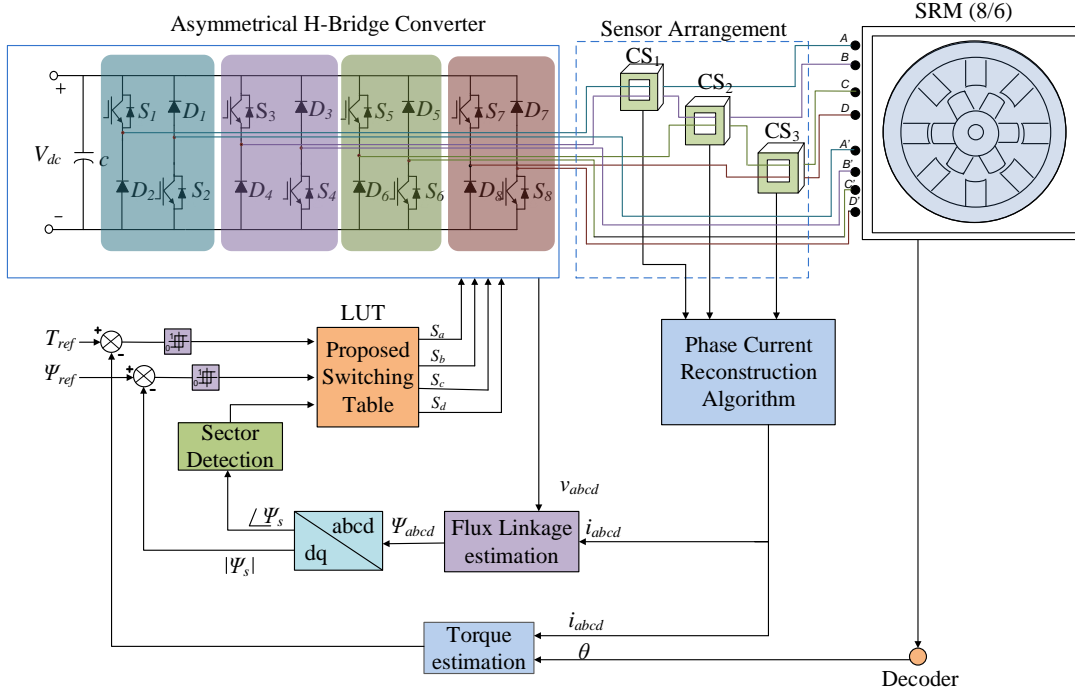


Figure 4.9: Block diagram of proposed phase current reconstruction algorithm

Table 4.4: Current sensor outputs corresponding to regions

Region	Sectors	$I_{CS1}$	$I_{CS2}$	$I_{CS3}$
$(R_1)$	11, 12, 13, and 14	$i_a$	$i_c$	$i_c + i_d$
$(R_2)$	15, 16, 1, and 2	$i_a + i_b$	$i_b$	$i_d$
$(R_3)$	3, 4, 5, and 6	$i_a + i_b$	$i_b + i_c$	$i_c$
$(R_4)$	7, 8, 9, and 10	$i_b$	$i_b + i_c$	$i_c + i_d$

The flowchart of the proposed phase current reconstruction algorithm based on sectors ( $N_{1-16}$ ) and regions ( $R_1-R_4$ ) is shown in Figure 4.11. For instance, if the angle lies in sector 11-16, then it corresponds to region-1 and phase currents are estimated through measured currents from sensors and algebraic logic. Once the phase currents are estimated, then it is used for flux linkage vector estimation for closed-loop of DTC. The flux linkage vector can be estimated as

$$\psi_j = \int (v_j - r_j \cdot i_j) \cdot dt \quad (4.11)$$

Where  $\psi_j$ ,  $v_j$ ,  $i_j$ , and  $r_j$  are the respective flux linkages, voltage, current and resistance of the phase 'j'. The proposed method operates the drive at high

performance and also detects the phase currents by using only three sensors without any additional requirements. Furthermore, it does not require any converter change and pulse injection. As a consequence, there will not be any voltage penalty and further it is easy to implement when compared to existing phase detection techniques.

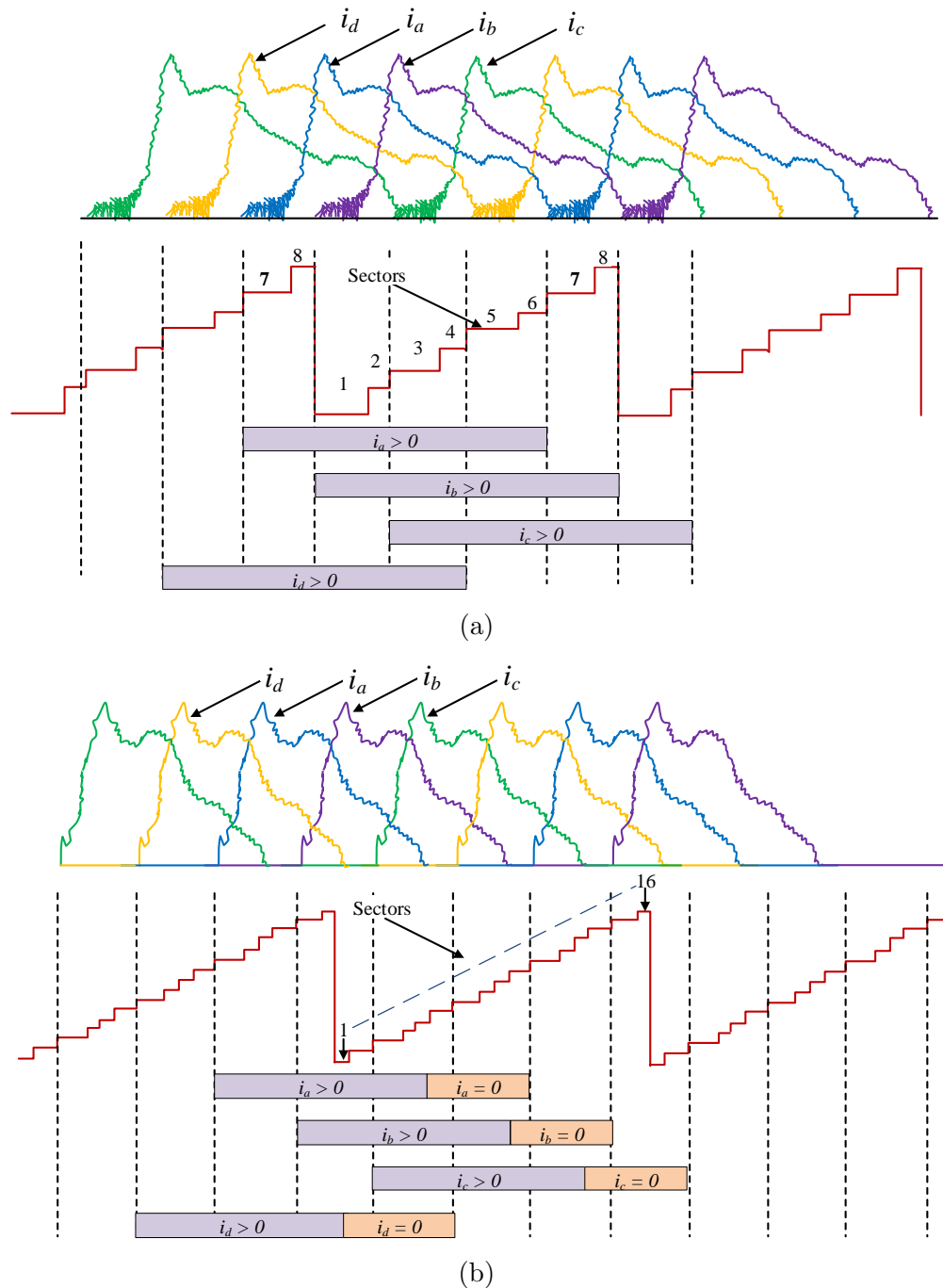


Figure 4.10: Illustration of phase currents overlap in (a) Conventional DTC, (b) Proposed DTC

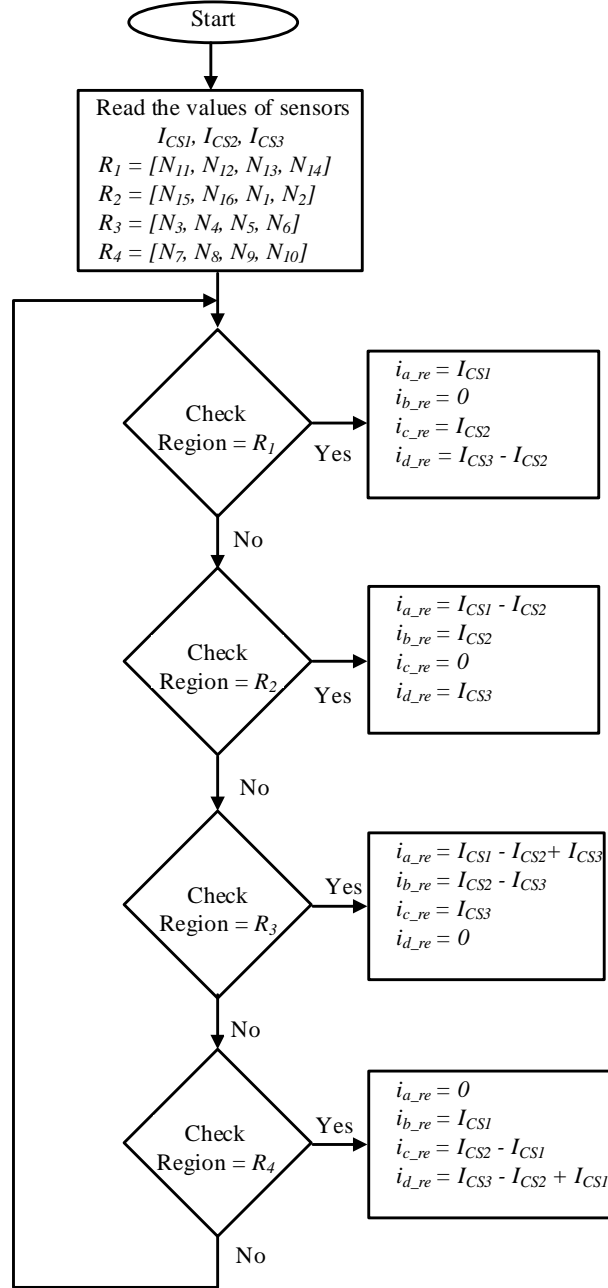


Figure 4.11: Flowchart of the proposed phase current reconstruction algorithm.

## 4.4 Results and Discussions

To demonstrate and verify the performance of the proposed DTC with phase current reconstruction strategy, a MATLAB/Simulink model of a 8/6 4-kW four-phase SRM with the proposed control structure is developed. The simulation studies of the proposed scheme have been carried out at different operating conditions with 15 Nm reference torque. The actual phase currents  $i_a$ ,

$i_b$ ,  $i_c$ , and  $i_d$  when the motor is running at 750 rpm are shown in Figure 4.12. The sensor currents  $I_{CS1}$ ,  $I_{CS2}$ , and  $I_{CS3}$  are shown in Figure 4.13. The reconstructed phase currents  $i_{a,re}$ ,  $i_{b,re}$ ,  $i_{c,re}$ , and  $i_{d,re}$  obtained from the sensor currents  $I_{CS1}$ ,  $I_{CS2}$ , and  $I_{CS3}$  using the proposed current detection method are shown in Figure 4.14. The results show that the reconstructed phase currents are the same as actual currents obtained by one sensor per phase. The estimated phase currents are utilized for flux estimation for closed-loop DTC control. The error between the actual and reconstructed phase currents is shown in Figure 4.15.

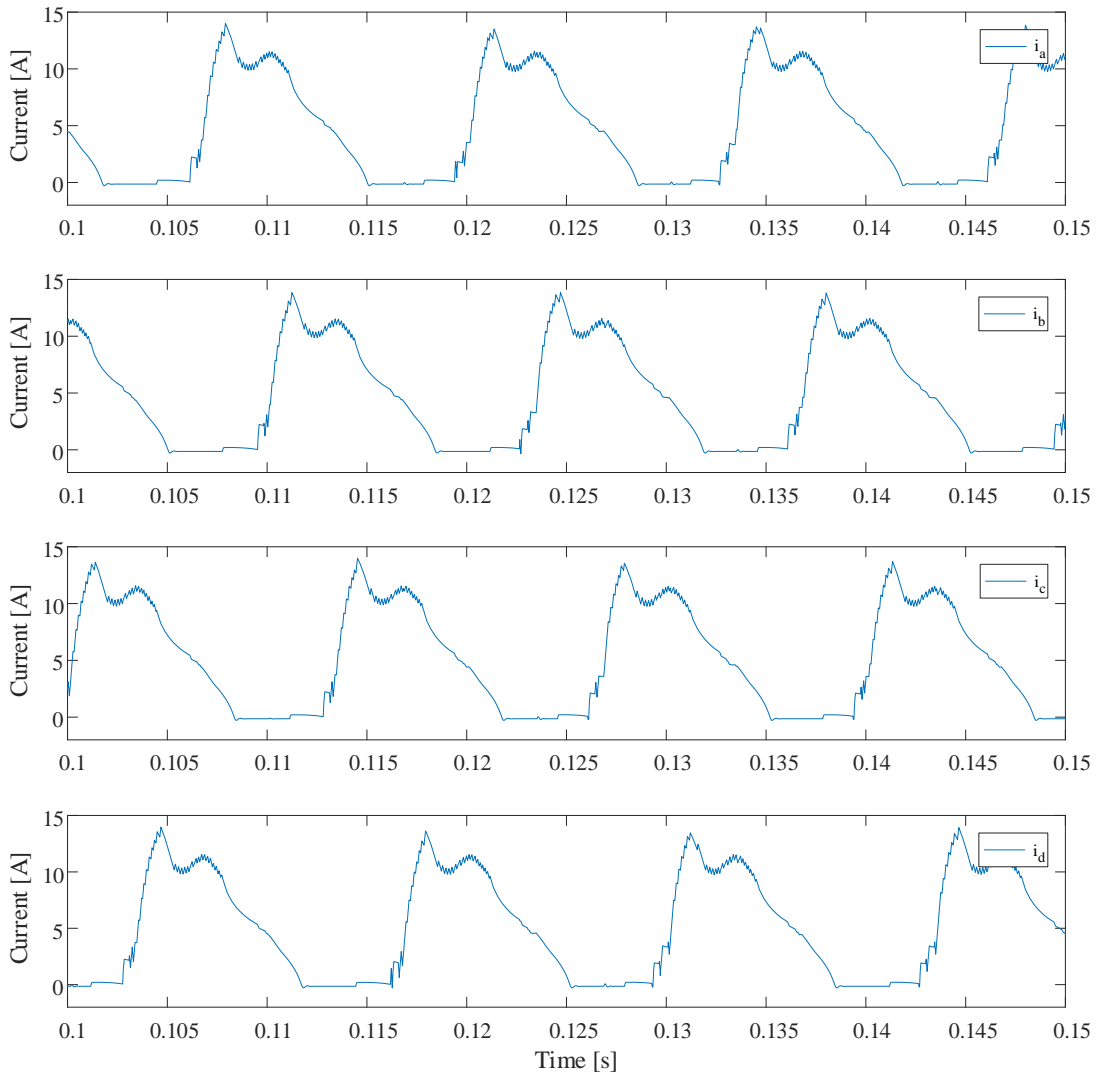


Figure 4.12: Actual phase currents  $i_a$ ,  $i_b$ ,  $i_c$ , and  $i_d$  measured by sensor per phase at 750 rpm

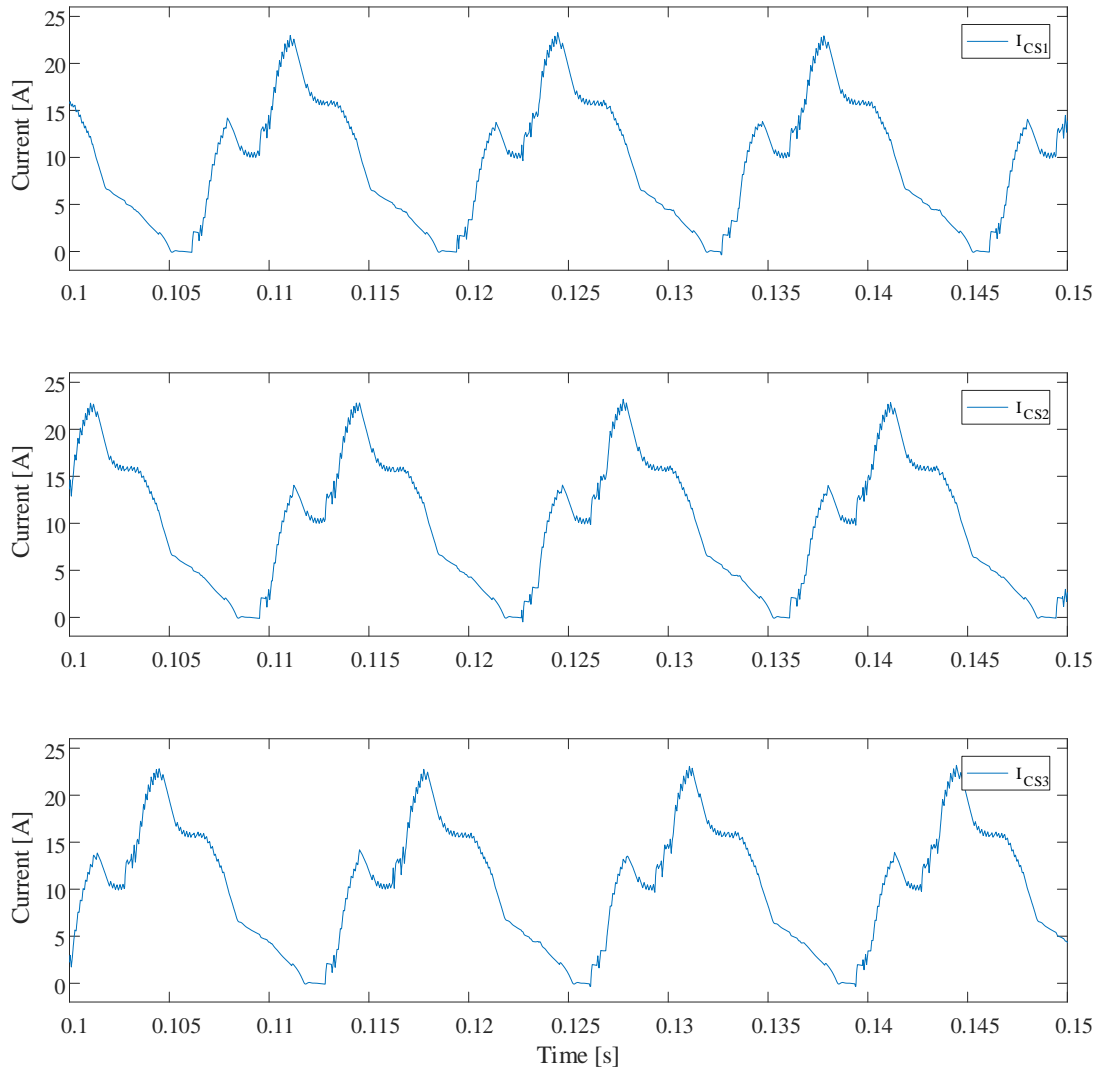


Figure 4.13: Sensor currents  $I_{CS1}$ ,  $I_{CS2}$ , and  $I_{CS3}$  at 750 rpm

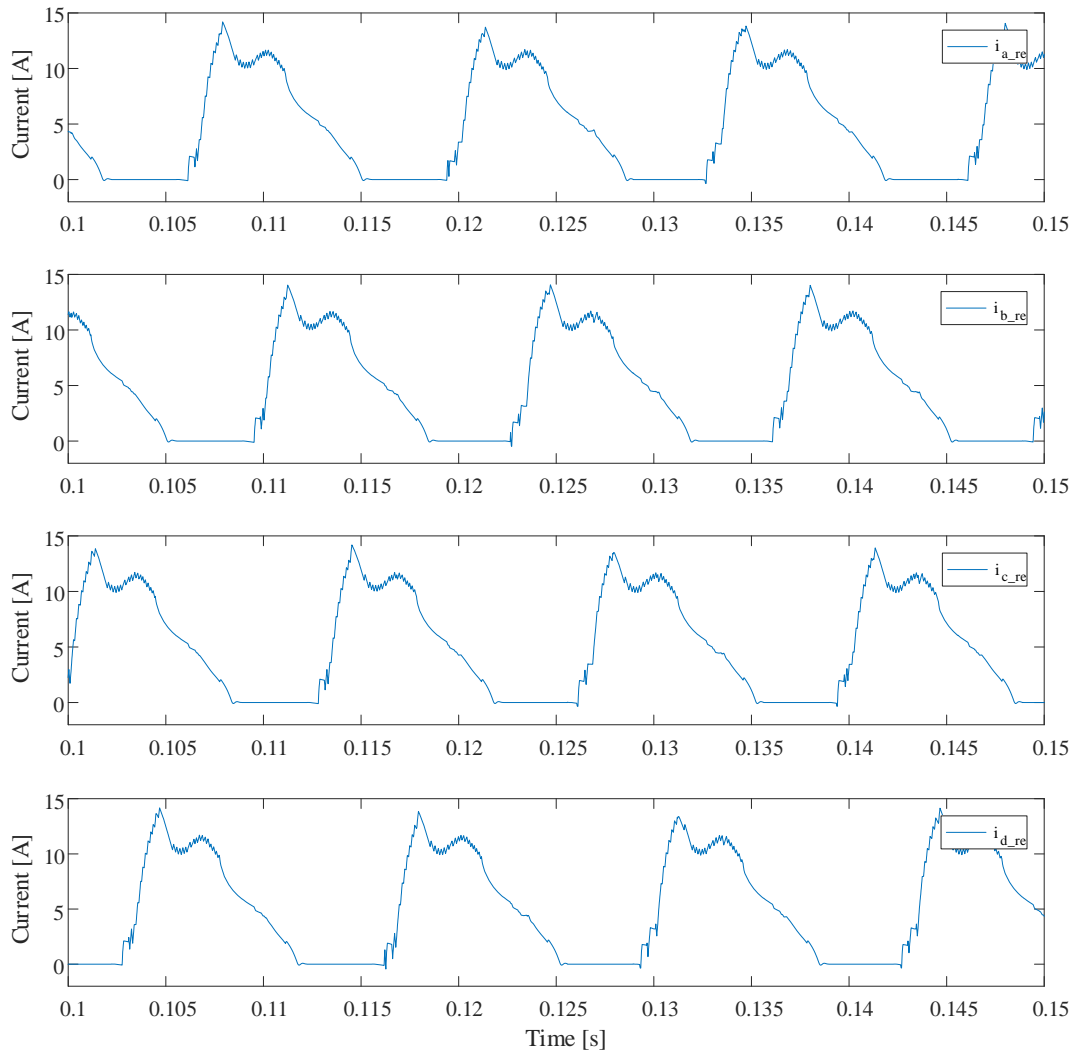


Figure 4.14: Reconstructed phase currents  $i_{a.re}$ ,  $i_{b.re}$ ,  $i_{c.re}$ , and  $i_{d.re}$  at 750 rpm

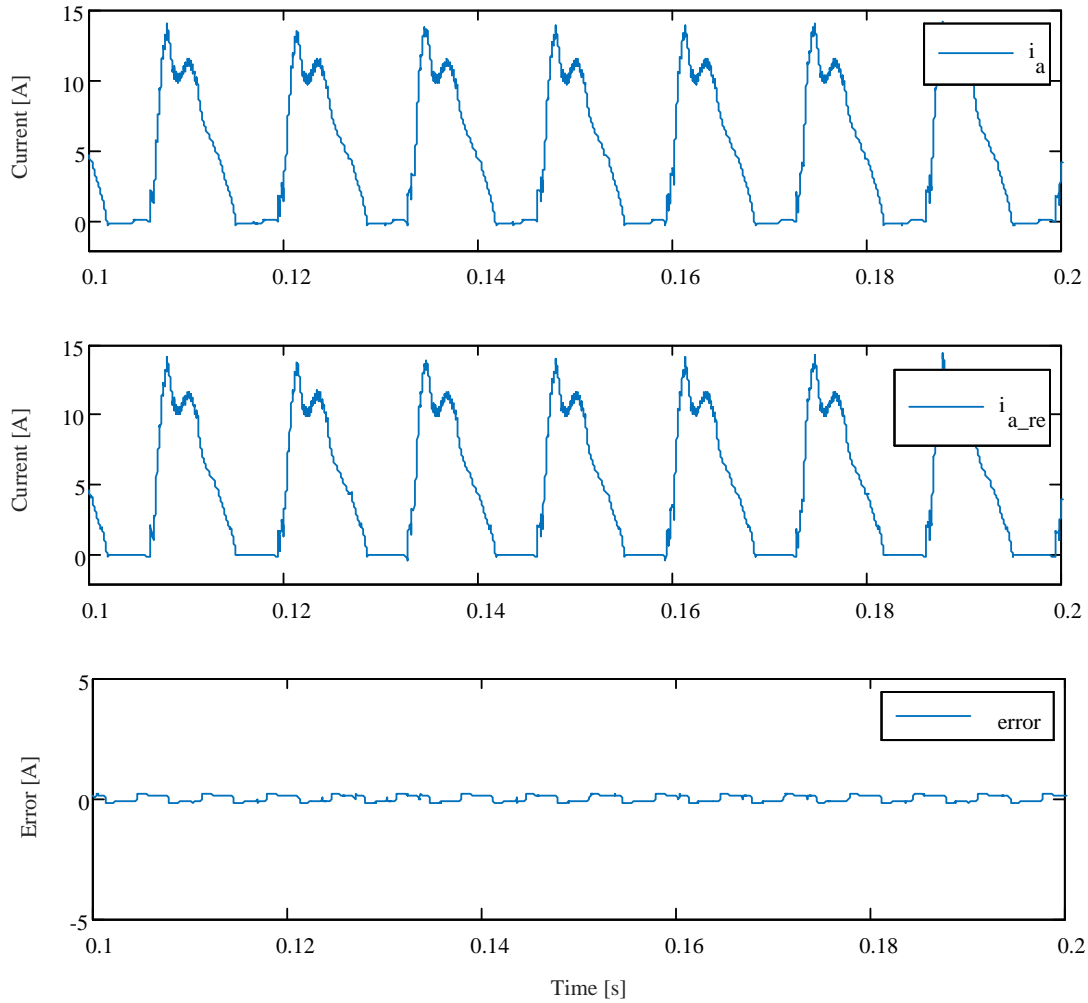


Figure 4.15: Actual phase current  $i_a$ , reconstructed current  $i_{a\_re}$  and  $error$  at 750 rpm

## 4.5 Real-Time Validation

The proposed scheme is further validated on the OPAL-RT based real-time platform under various operating conditions. The phase currents over the 16 sector region is shown in Figure 4.16. The actual phase current, reconstructed phase current and the corresponding error under both steady-state and dynamic conditions are shown in Figure 4.17a and Figure 4.18 respectively. The three sensor currents and the corresponding reconstructed phase current as shown in Figure 4.17b coincide well with the simulation results, which verifies the effectiveness of the approach. It can be observed that phase currents are reconstructed with high accuracy. The reconstructed four-phase currents are used for flux estimation and closed-loop DTC control of an SRM drive. Figure

4.18 shows the real-time results of the actual, reconstructed phase currents and the corresponding errors during the acceleration and deceleration process. It is noticed that, the estimation process achieves high accuracy, which shows its effectiveness under dynamic conditions.

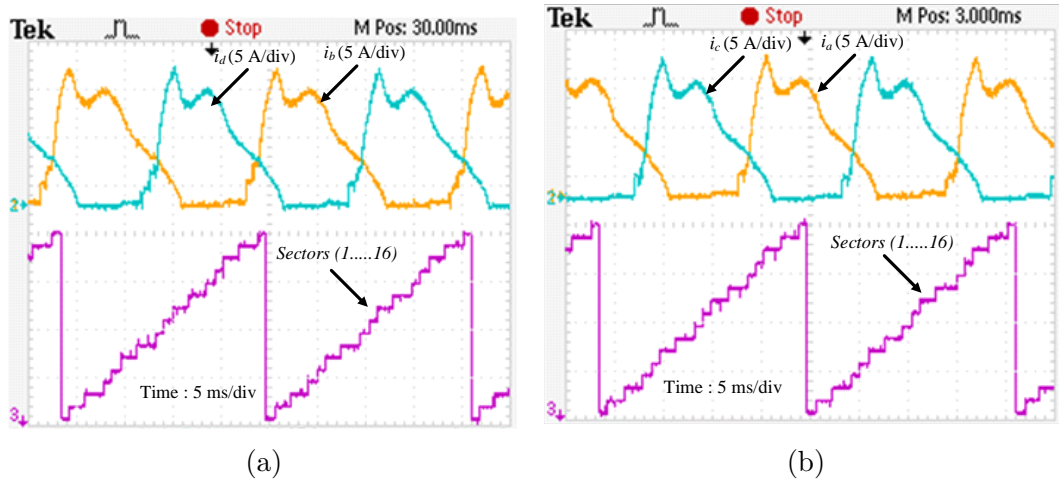


Figure 4.16: Phase currents vs. sectors: (a) Phases B & D, (b) Phases A & C

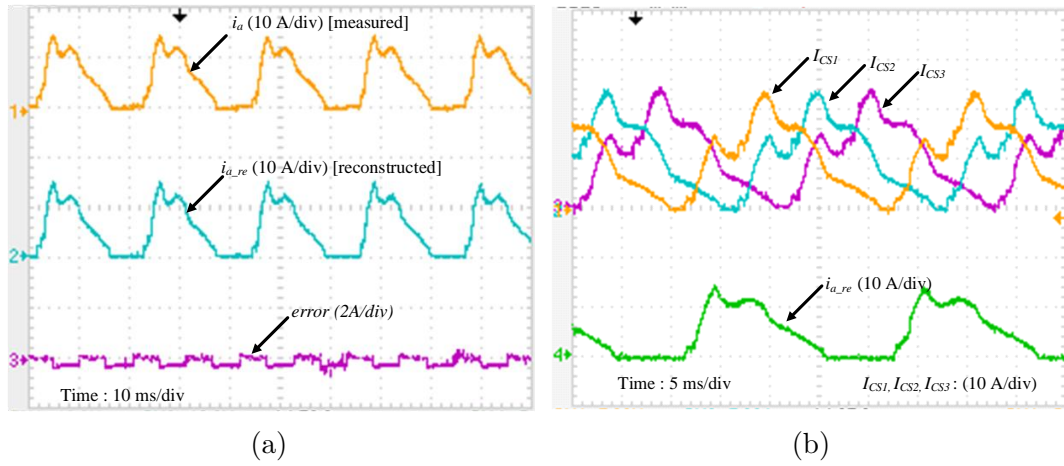


Figure 4.17: Test results of the proposed current reconstruction scheme: (a) Actual phase current  $i_a$ , reconstructed phase current  $i_{a\_re}$  and error at 750 rpm, (b) Sensor currents  $I_{CS1}$ ,  $I_{CS2}$ , and  $I_{CS3}$  and corresponding reconstructed phase current  $i_{a\_re}$



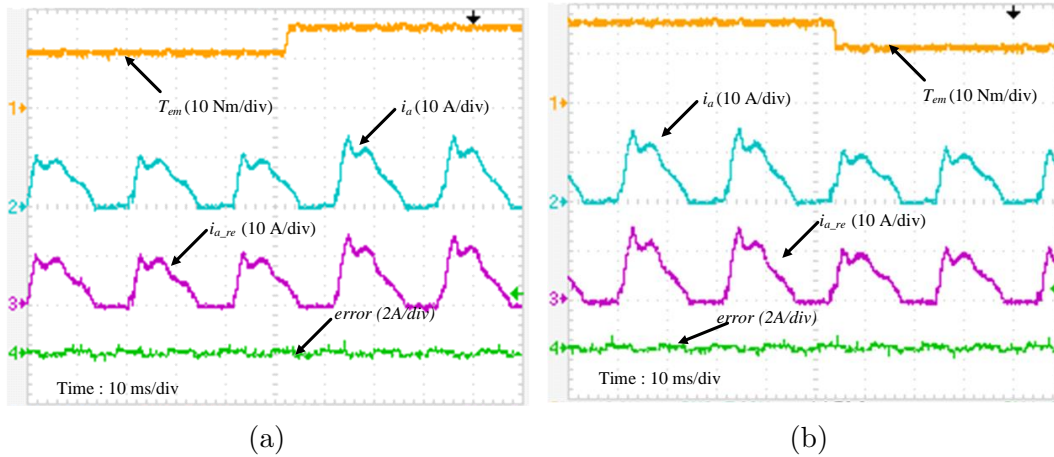


Figure 4.18: Test results of actual phase current  $i_a$ , reconstructed phase current  $i_{a\_re}$  and error at dynamic conditions during: (a) Acceleration, (b) Deceleration

## 4.6 Summary

A simple phase current reconstruction scheme is developed for four-phase SRM without the need for power converter change, switching state modification and pulse injection & therefore no voltage penalty. In this proposed method, a closed-loop flux estimation approach is developed using the proposed phase current detection scheme for four-phase SRM based on the sixteen-sector segregation and corresponding optimal voltage vector selection. A 4-kW 8/6-pole four-phase SRM drive system is used to verify the effectiveness of the proposed DTC with a phase current detection scheme through MATLAB simulations and real-time test studies. The reconstructed phase currents are verified with general phase current sampling with a single sensor per phase approach to check the correctness of the proposed approach. The real-time results confirm that the proposed control scheme provides a simple and cost-effective solution for phase current measurement.

# Chapter 5

## Hardware Implementation of Hysteresis Current Control for Four-Phase SRM Drive

### 5.1 Introduction

A four phase SRM drive test setup is built with 2.2 kW SRM coupled with 2.2 kW eddy current brake capable of applying 14 Nm load torque on the motor. The test setup consists of SRM, eddy current brake, AHBC, Programmable DC power supply, 3-Phase auto transformer, voltage and current sensor modules, STM-32 Microcontroller, DSO and host PC. Voltage control and hysteresis current control algorithms are developed in accordance with phase inductance variation.

### 5.2 Phase Inductance Profile Relative to position Sensor Output

The phase inductance ( $L$ ) cycle of four-phase 8/6 SRM repeats for every  $60^\circ$  mechanical rotation of rotor. The variation of  $L$  with the rotor position exhibits positive  $\frac{dL}{d\theta}$  for half of the period and negative  $\frac{dL}{d\theta}$  for remaining half period at constant current. However, the conduction of any phase during the negative  $\frac{dL}{d\theta}$  region produces the negative torque which reduces the T/A. This undesirable negative torque generation can be overcome by developing phase inductance based control algorithm which excites the phase, only during positive  $\frac{dL}{d\theta}$  region.

To develop the commutation algorithm, phase winding inductance is measured for one electrical cycle with LCR meter. One electrical cycle is divided into eight regions ( $R_1, \dots, R_8$ ) such that each region has a different state of position sensor signal ( $P_1, P_2, P_3,$  and  $P_4$ ) as shown in Figure 5.1. The corresponding phase winding inductance variation with respect to eight regions is shown in Figure

5.2 Therefore, the positive  $\frac{dL}{dt}$  region of each phase is identified and excited to generate positive torque. Hence, the developed algorithm effectively commutates each phase, thereby avoiding the negative torque generation.

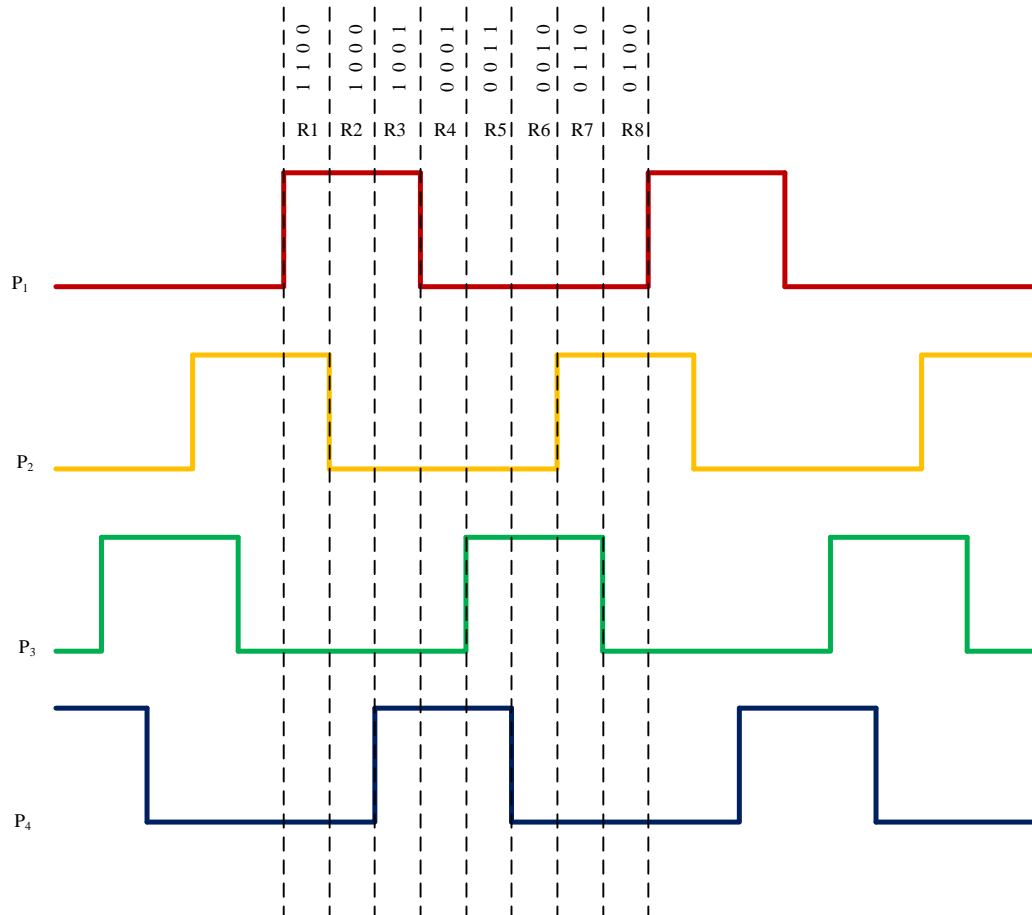


Figure 5.1: Rotor position sensor signals

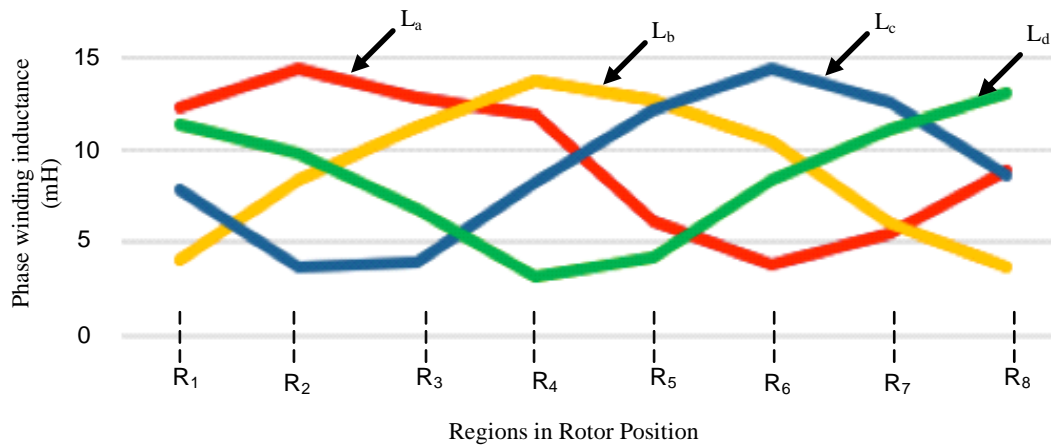


Figure 5.2: Phase inductance profile at eight different regions in one electric cycle.

## 5.3 Hardware Implementation

### 5.3.1 Voltage Control Algorithm

The schematic block diagram of voltage control algorithm is shown in Figure 5.3. In this scheme, rotor position is identified from sensor output ( $P_1...P_4$ ) and corresponding positive  $\frac{dL}{dt}$  phase is excited. The gate pulses for IGBT switches of AHBC are generated from STM32 microcontroller. The detailed specification of microcontroller is given in Appendix A.5. The general purpose input output (GPIO) pins of STM32 microcontroller are used to generate the gate pulses with the help of CUBEMX and Keil  $\mu$ Vision software.

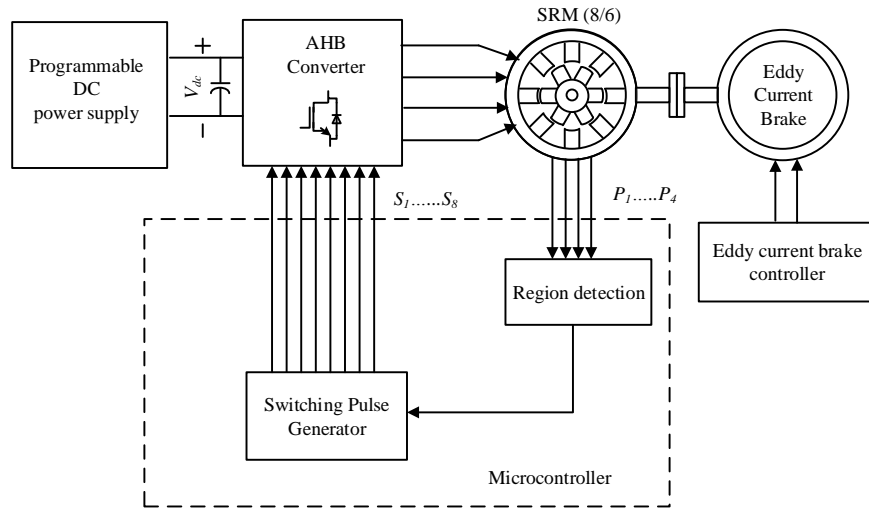


Figure 5.3: Block diagram of voltage control implementation

To validate the efficacy of the developed voltage algorithm, experiments are conducted on 2.2 kW four-phase SRM under no-load and load conditions. The experimental setup is shown in Figure 5.4. Eddy current brake is used for loading the motor. Figure 5.5a shows the phase voltage, current and corresponding gate signals of upper and lower switches AHBC for phase A when the motor is running at 500 rpm under no-load. In this method, motor speed is increased to 2000 rpm by increasing input  $dc$  voltage which is depicted in Figure 5.5b. The application of 2 Nm load torque by maintaining input voltage as constant, which brings the motor speed from 2000 rpm to 1000 rpm is shown in Figure 5.5c. The load torque can be varied by varying the  $dc$  excitation of eddy current brake. The variation of speed with input voltage is shown in Table 5.1.

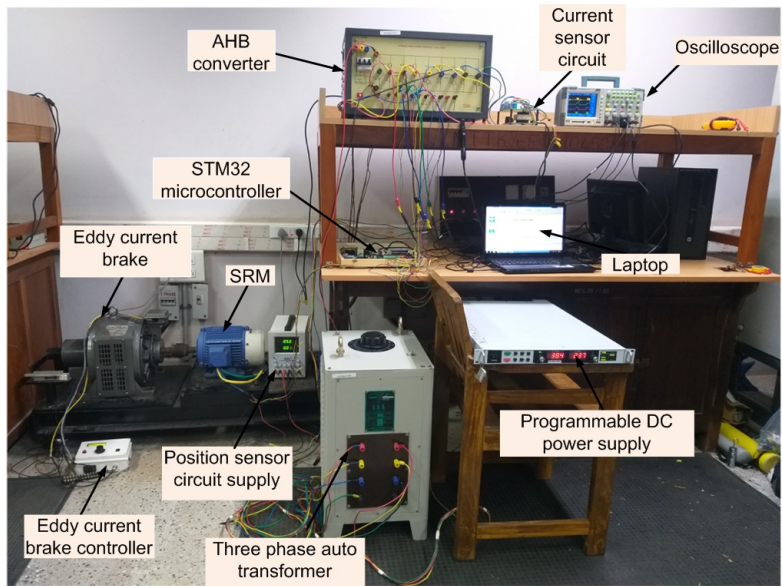


Figure 5.4: Experimental system of 2.2 kW SRM drive

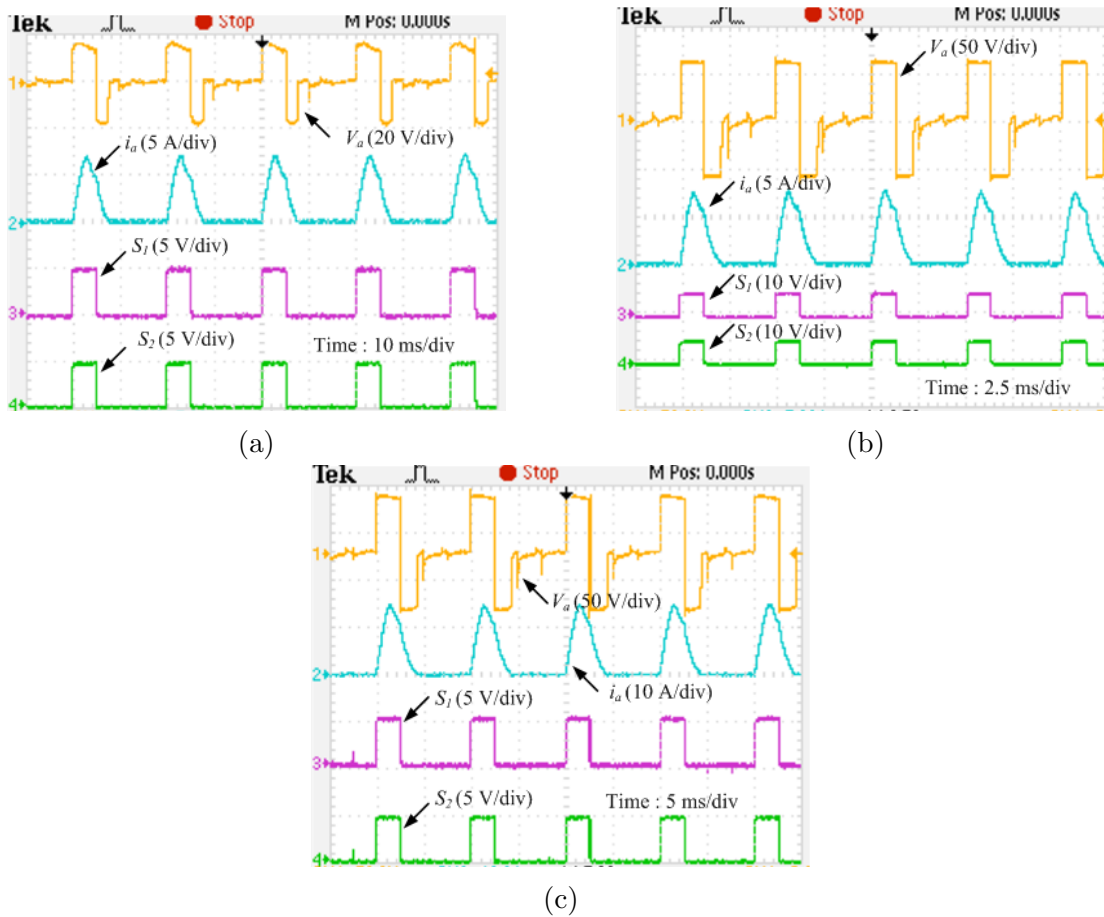


Figure 5.5: Voltage control : (a) No-load at 500 rpm, (b) No-load at 2000 rpm, and (c) 1000 rpm at 2 Nm load.

Table 5.1: Voltage vs. speed for voltage control method

$V_{DC}$ (volts)	$I_{ph,rms}$ (A)	Speed (rms)	Load Torque (Nm)
16.3	2.68	500	
27.4	2.74	1000	No-load
46.2	3.09	1500	
58.8	3.18	2000	
58.8	4.59	1300	1
58.8	5.81	1000	2

### 5.3.2 Hysteresis Current Control Algorithm

The block diagram of the hysteresis current control algorithm is shown in Figure 5.6. The gating signals for the switches of AHBC are developed from rotor position sensor signals and current chopping is applied to lower switches of AHBC by comparing actual and reference phase currents.

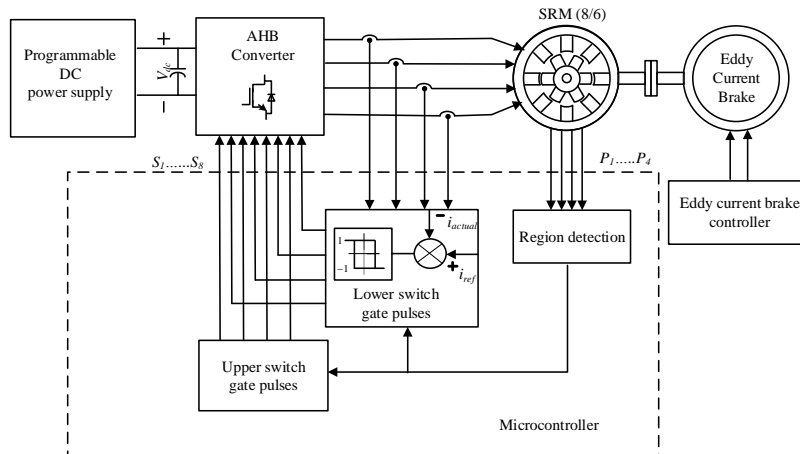


Figure 5.6: Block diagram of hysteresis current control implementation

The hysteresis current control is implemented at 330 rpm by controlling the lower switch within the positive inductance slope region. Phase current are measured and processes to 12-bit Analogue-Digital Converters (ADC). General purpose timers are used for implementing hysteresis control. Therefore, the bandwidth of the hysteresis can be controlled by changing timer interrupt rate. The syntax code for hysteresis implementation is shown below.

1. Initialize four analog pins (Ex. PC0, PC1, PC2, PC3) for ADC and get actual value of current with proper scaling.

2. Initialize four GPIO pins (Ex. PD12, PD13, PD14, PD15) to generate gate pulses for lower switches.
3. Initialize one general purpose timer (Ex. Timer 4) for generating interrupt.
4. The embedded code for hysteresis implementation for one phase is shown below.

---



---

```

Algorithm for hysteresis current control
if (htim → Instance == TIM4)
{
  if ( $I_{a\_actual} > I_{a\_ref}$ )
  {
    HAL_GPIO_WritePin(GPIOD, GPIO_PIN_12, GPIO_PIN_RESET);
  }
  else
  {
    HAL_GPIO_WritePin(GPIOD, GPIO_PIN_12, GPIO_PIN_SET);
  }
}

```

---



---

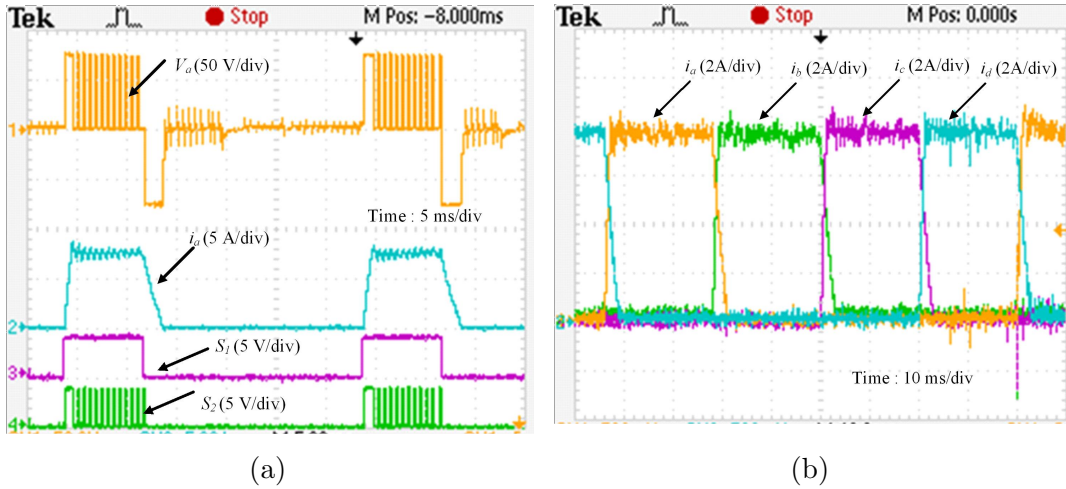


Figure 5.7: Hysteresis current control: (a) Hysteresis current control at  $i_{ref} = 8A$ , (b) Phase currents at 10 kHz timer interrupt rate.

Phase voltage, current and gate signals for hysteresis current control at reference current of  $i_{ref} = 8A$  are presented in Figure 5.7a. The phase currents at 10 kHz timer interrupt rate are shown in Figure 5.7b.

## 5.4 Summary

The phase winding inductance of 2.2 kW SRM with respect to rotor position is measured with LCR meter. The commutation logic for voltage control is

developed to excite the phase, which is under positive inductance slope region, thereby produces only positive torque. The hysteresis current control is developed by applying hysteresis to lower switches of AHBC converter. The algorithms are implemented with STM32 microcontroller by using CUBEMX and Keil  $\mu$ Vision software.





# Chapter 6

## Conclusion & Future Scope

### 6.1 Conclusion

This chapter discuss about the chapter wise conclusion of the research work presented in this Thesis. In this research work, two variations of voltage vector selection in DTC algorithm for SRM are proposed to minimize torque ripple and improve T/A. In addition to that a novel phase current reconstruction algorithm for four phase SRM operating under DTC is proposed. The chapter wise conclusions are as follows.

In Chapter 1, the construction and operating principle of SRM are studied. The origin of torque ripple is studied and review of torque ripple minimization algorithms is carried out. It is observed that torque ripple can be minimized either by design modifications or by using optimized control algorithms. Different control algorithms such as current profile techniques, angle optimization techniques, TSF based control algorithms and DTC algorithms are analyzed to understand the merits and demerits. Out of these algorithms, the DTC scheme draws more attention which utilizes the principle of DTC applied to traditional AC machines. This method offers advantages such as automatic control (no turn-on/off angle control), fast dynamic response, insensitivity to motor parameters and does not require rotor position information. Moreover, this method can be easily extended to multi-phase SRMs. In addition to this, the literature on phase current reconstruction algorithms is carried out. The phase current information is required for developing current control, flux linkage calculations as well as for protection. The phase current reconstruction algorithms are broadly classified as with and without pulse injection methods. Pulse injection methods results in voltage penalty. The phase current detection from dc link sensor needs converter modifications. To avoid the drawbacks of these methods, multiplexed phase current reconstruction scheme is proposed in

the literature, it doesn't require converter modifications and pulse injection. Therefore, it is evident that multiplexed scheme provides simple and cost effective solution for phase current reconstruction.

In Chapter 2, mathematical modeling of the four phase SRM is developed in lookup table approach using magnetization and torque characteristics. The characteristics obtained from the experimental studies are used in the modeling. The conventional DTC algorithm is developed and it is observed that conventional DTC exhibits poor performance in terms of high torque ripple and low T/A. This is due to the inappropriate voltage vector selection. In conventional DTC, the active phase has to develop more torque to compensate for the negative torque generated by the outgoing phase due to an extension of phase current in the negative inductance slope region. Therefore, it draws more current from the source, thereby reducing net T/A and the drive efficiency. Moreover, the large input power pulsations occur, which demands a larger DC-link capacitor.

In Chapter 3, a 16-sector 8-vector DTC is proposed to reduce the torque ripple and improve T/A. In this method, vector selection will change for every  $22.5^\circ$  instead of  $45^\circ$  as in the conventional DTC. This will help to select optimized voltage vectors to improve the dynamic performance of the drive. Further, MATLAB simulations & OPAL-RT real-time simulation studies are carried out to verify the effectiveness of the proposed control algorithm. The proposed method eliminates the existence of current in the zero torque region thereby improve the T/A. Even though this method eliminates the current in zero torque region, the negative phase torque still existing due to long tail current in the phase. Further, 16-sector 16-vector approach is proposed by defining 8 new vectors for torque decreasing condition. The simulation studies are carried out and performance studies are conducted. The performance of the proposed DTC is compared with and conventional DTC to validate the efficacy of the proposed algorithm.

In Chapter 4, a simple phase current reconstruction scheme is developed for a four-phase SRM without any power converter change, switching state modification or/and pulse injection, thereby no voltage penalty. In this proposed method, a closed loop flux estimation approach is developed using the proposed phase current detection scheme for a four-phase SRM based on the sixteen-sector segregation and corresponding optimal voltage vector selection. A 4 kW

four-phase 8/6-pole SRM drive system is used to verify the effectiveness of the proposed DTC with a phase current detection scheme through MATLAB simulations and real-time test studies. The reconstructed phase currents are verified with general phase current sampling with a single sensor per phase approach to check the correctness of the proposed approach.

In Chapter 5, voltage control and hysteresis current control algorithms are developed for four phase SRM using STM32 microcontroller. The commutation logic for phases is developed from the phase inductance profile.

## 6.2 Research Contributions of the Thesis

1. Dynamic model of four phase SRM is developed in look table approach using flux linkage and torque characteristics.
2. Conventional direct torque control algorithm is developed and analyzed with respect to torque ripple, T/A, source current ripple. The reasons behind the negative torque generation are studied.
3. 16-sector 8-vector DTC method is proposed to avoid the existence of phase current in the zero torque region. Even though this method improves the performance of drive, the negative phase torque still exists that results in low T/A. To overcome this, 16-sector 16-vector DTC is proposed to completely eliminate the negative torque generation, thereby improves T/A and reduces the torque ripple.
4. The existing phase current reconstruction methods are studied. The existing methods can't be applied to DTC due to the simultaneous conduction of all phases. A new phase current reconstruction method is developed for DTC controlled SRM drive with reduced number of sensors.
5. Voltage control and hysteresis current control algorithms are implemented in hardware based on phase inductance profile with STM32 microcontroller.

## 6.3 Future Scope

Based on the research carried out in this thesis, the recommendations for future research are as follows:

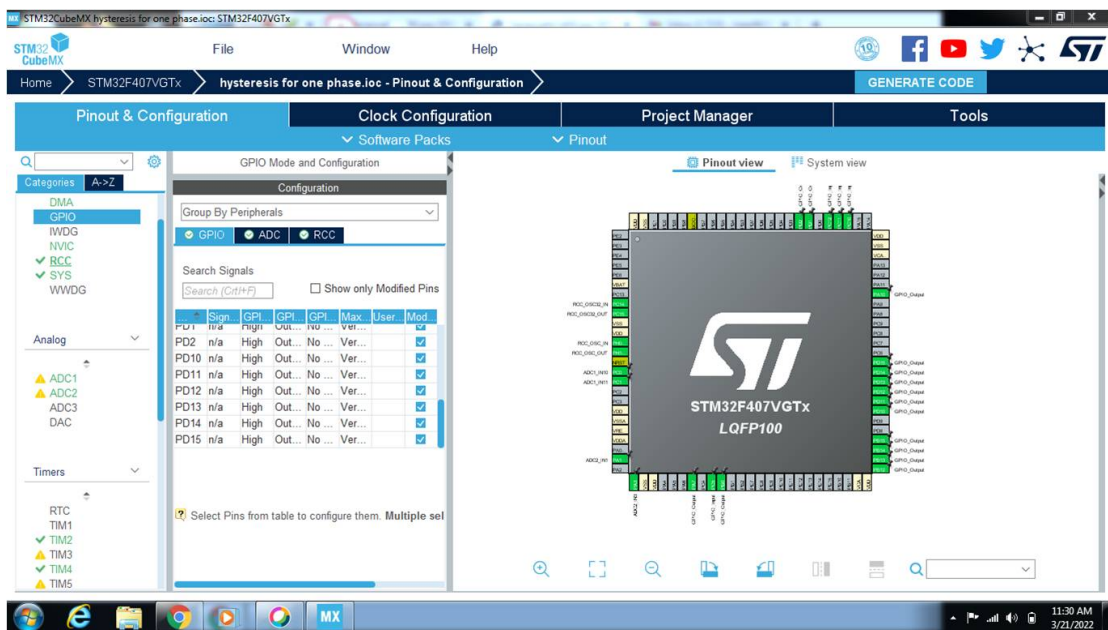
- To investigate the performance of the proposed DTC algorithms for variable flux linkage reference in SRM drives.

- To investigate the performance of the proposed control algorithms with unequal sector partition.
- To investigate the performance of the proposed DTC algorithms for EV applications.
- To investigate further, to limit the number of current sensors required to either 'one' or 'two' under DTC controlled four phase SRM drive.

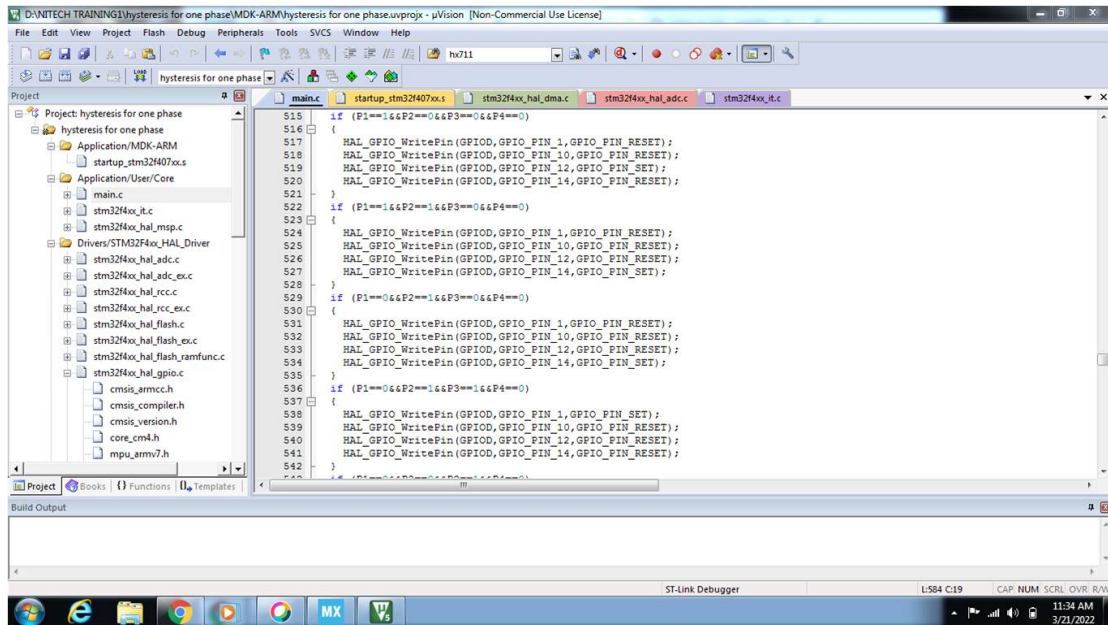
# Appendix A

## Software Details

### A.1 STM32 microcontroller Pin Configuration using CUBEMX Software



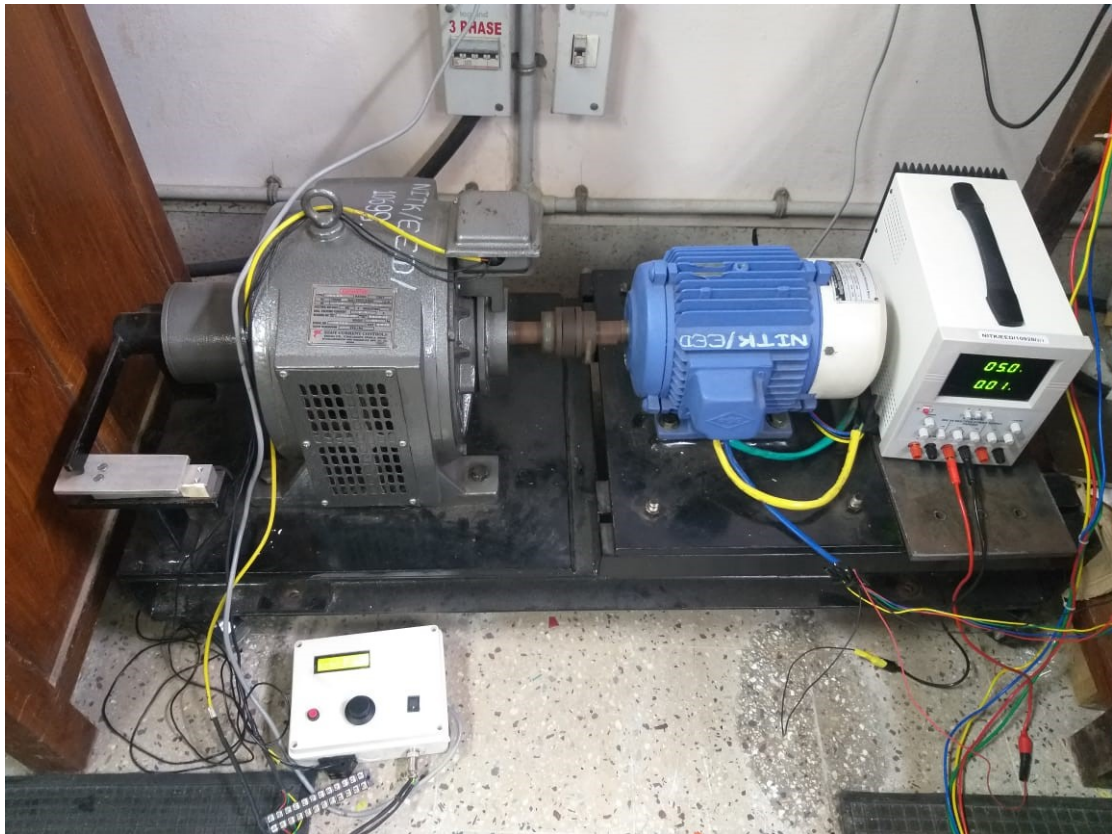
## A.2 Embedded Code Development using Keil $\mu$ Vision software



# Appendix B

## Hardware Specifications

### B.1 Specification of SRM



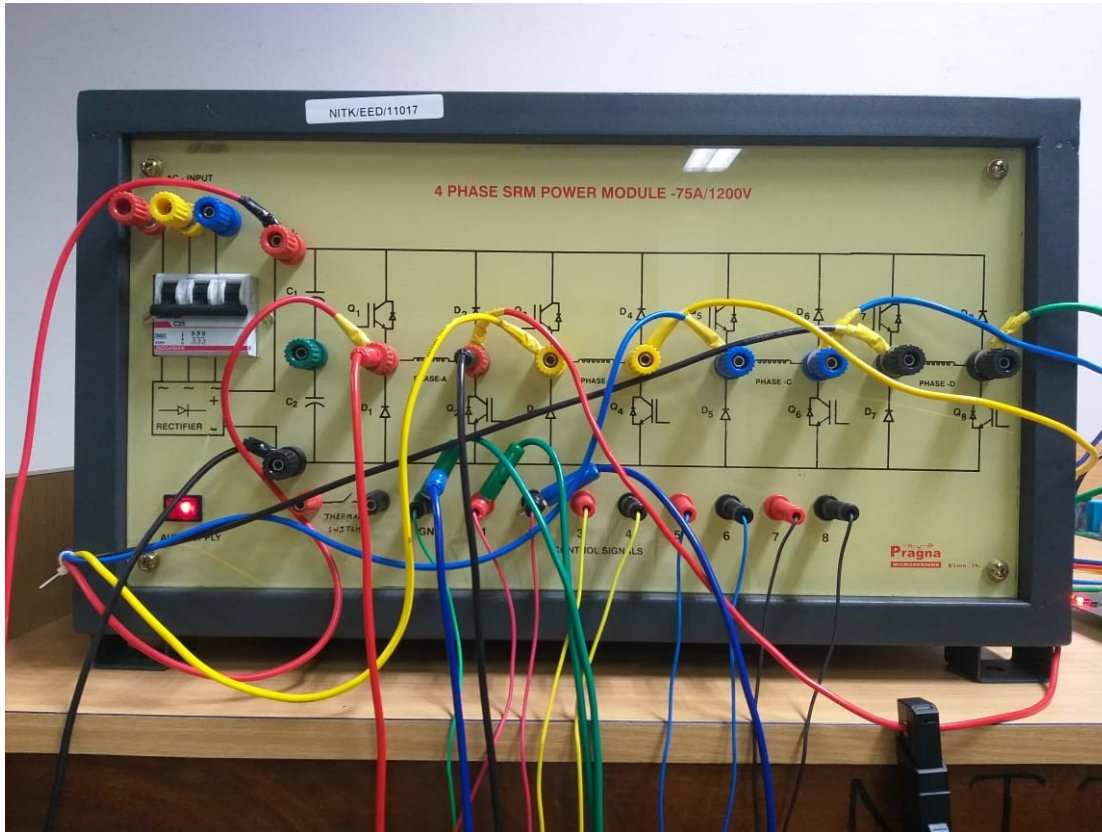
Power = 2.2 kW, Phase = 4, Stator poles/Rotor poles = 8/6, DC Voltage ( $V_{dc}$ ) = 230 V, Line current = 11 A, Speed = 3000 rpm,

### B.2 Specification of Eddy Current Brake

Frequency = 50 Hz, Torque = 1.4 kg.m, Speed range = (120 – 1200) rpm, Exciting Voltage = 80 V, Maximum Exciting Current = 2.5 A, Weight = 90 kg.



## B.3 Specification of Rectifier and Asymmetric H- Bridge Converter



### 1. Rectifier Specifications

- Configuration: Three-phase uncontrolled, six pulse
- Input AC: 415 V (L-L)
- Output DC: 600 V
- DC output Current: 50 A (RMS)
- Filtering Capacitor: 4700  $\mu$ F, 450 V

### 2. Asymmetric H- Bridge

- Configuration: 4-phase
- DC Input Voltage: 1200 V
- AC output Voltage: 415 V

- AC Output Current: 75 A
- Switch Model: SKM150GAL12T4/ SKM150GAR12T4

## B.4 Specification of Power Supplies

### 1. Three Phase Auto Transformer



- Max kVA = 22.793 kVA
- Primary Voltage = 415 V
- Secondary Max Voltage = (0-470) V
- Output Current = 28 A

### 2. Programmable DC Power Supply

- Input AC voltage = (187 – 229) V
- Input AC Current = 11 A
- Input Frequency = (50 – 400) Hz
- Supply Connection = Three Phase

- Output DC voltage = (0 – 300) V
- Output Current = (0 – 8.6) A
- Output Power rating = (0 - 2.6) kW



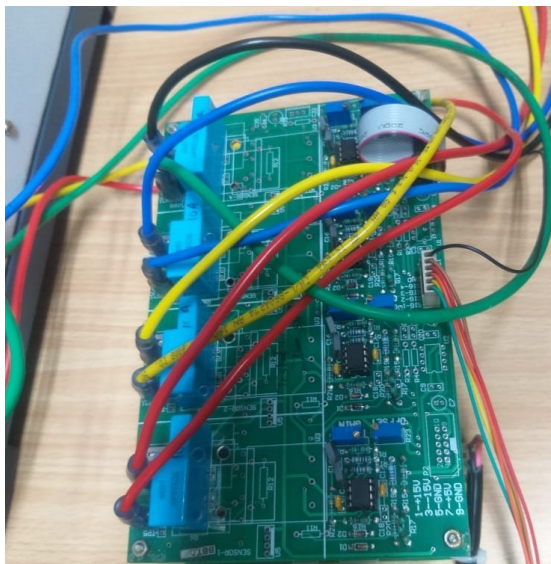
## B.5 Specification of ARM Cortex M4 32-bit Microcontroller Development Board

- STM32F407VGT6 microcontroller featuring 32-bit ARM Cortex-M4F core, 1 MB Flash, 192 KB RAM in an LQFP100 package.
- Microcontroller running at 168 MHz
- On-board ST-LINK/V2 for programming and debugging.
- Board power supply: through USB bus or from an external 12V AC supply.
- LIS302DL, ST MEMS motion sensor, 3-axis digital output accelerometer.
- MP45DT02, ST MEMS audio sensor, Omni-directional digital microphone
- CS43L22, audio DAC with integrated class D speaker driver
- All pins have 5V tolerance.
- GPIO ports are routed to header on mother board for easy connection
  - 8 General purpose input lines, 8 General purpose output lines
  - 16X2 LCD interface, 5 keys interface.

- 3 High speed digital outputs and 2 High speed digital input lines.
  - 6 PWM outputs, 3 QEI inputs.
  - SPI bus for SPI slave interface.
  - 9 Analog inputs.
  - 2 Analog Universal outputs: 0 to 10V or 4-20mA.
  - 9-pin D-type connector for RS232 interfaces.
- Eight LED
    - LD1 (red/green) for USB communication, LD2 (red) for 3.3 V power on.
    - Four user LEDs, LD3 (orange), LD4 (green), LD5 (red) and LD6 (blue)
    - 2 USB OTG LEDs LD7 (green) VBus and LD8 (red) over-current
  - USB OTG FS with micro-AB connector.

## B.6 Specification of Voltage and Current Sensor Boards

### 1. Four Channel Hall Current Sensor Card

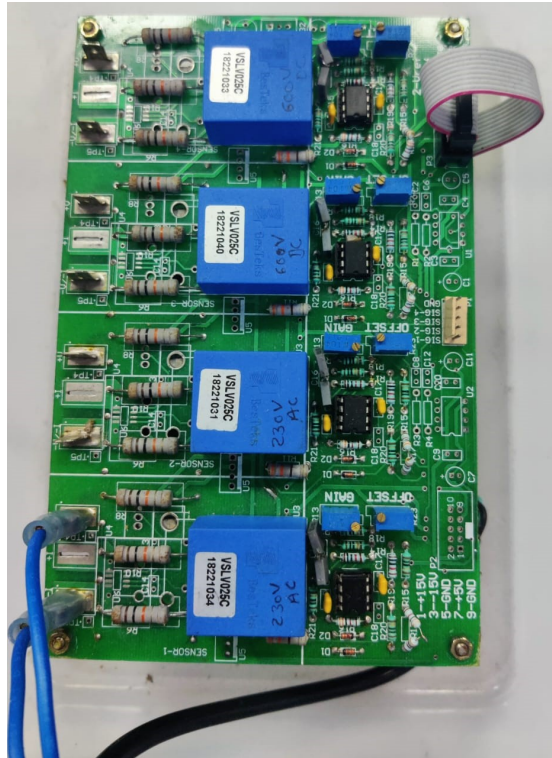


- One AC/DC current measurement
  - Isolated measurement

- One current sensing using Hall-Current Sensor
- 0-3V (peak-peak) output
- Unipolar output with DC offset
- Suitable for interfacing with unipolar ADC channel
- Two or more cards can be cascaded together with expansion connectors when necessary.
- Hall-current Sensor Specifications
  - Output voltage at  $I_r$ ,  $T_A = 25^\circ\text{C}$ : 4 V
  - Output Impedance <150 ohm
  - Load Resistor >10 Kohm
  - $V_{cc}$  Supply Voltage:  $\pm 15\text{V} \pm 5\%$
  - Current Consumption <20mA
  - Accuracy at  $I_r$ ,  $T_A = 25^\circ\text{C}$  (without offset) <1%
  - Linearity from 0 to  $I_r$ ,  $T_A = 25^\circ\text{C}$  <1%
  - Frequency Bandwidth (-3dB) 50 KHz
- Common as well as individual offset setting.
- Auxiliary power supply Board. For providing  $\pm 15\text{ V DC}$ ,  $+5\text{ V}$

## 2. Four Channel Hall Voltage Sensor Card

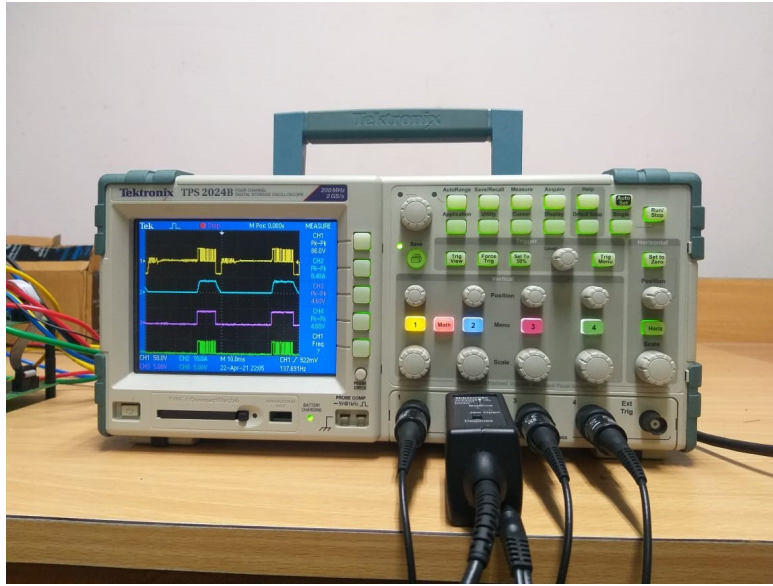
- Four AC/DC voltage measurement.
  - Isolated measurement.
  - Four voltage sensing using Hall-Voltage Sensor
  - 0-3V (peak-peak) output
  - Unipolar output with DC offset
  - Suitable for interfacing with unipolar ADC channel
- Auxiliary power supply and connectors for power connections.
- Two or more cards can be cascaded together with expansion connectors when necessary.
- Hall-voltage Sensor Specifications
  - Primary voltage measuring range  $V_{PN}(\text{V})$ : 10 - 500
  - Primary nominal rms current: 10 mA
  - Primary current, measuring range: 0 -  $\pm 14\text{ mA}$



- Secondary nominal rms current: 25 mA
- Conversion ratio 2500:1000
- $V_c$  supply voltage  $\pm 12 - 15$  V, ( $\pm 5\%$ )
- $I_c$  current consumption  $10(\pm 15V) + I_s$  mA
- Creepage distance: 19.5 mm
- Linearity error  $< 0.2\%$

## B.7 Specification of DSO Tektronix TPS 2024B

- 100 MHz and 200 MHz bandwidths.
- 2 or 4 fully isolated and floating channels, plus impedance isolated external trigger input.
- Sample rates up to 2 GS/s real time on all channels.
- 2.5k point record length on all channels.
- 8 hours of continuous battery operation with two batteries installed, hot swappable for virtually unlimited freedom from AC line power.
- Optional power application software offers the broadest range of power measurements at its price point.



- Quickly document and analyze measurement results with open choice software or integrated compact flash mass storage.
- FFT standard on all models.
- Advanced triggers to quickly capture the event of interest
- Advanced triggers to quickly capture the event of interest traditional, analog-style knobs and multi-language user interface for easy operation.
- Quick setup and operation with auto set menu, auto range, waveform and setup memories, and built-in, context-sensitive help.
- Backlit menu buttons for high visibility.
- 11 of the most critical automatic waveform measurements.

# Bibliography

- [Abdalmagid et al., 2022] Abdalmagid, M., Sayed, E., Bakr, M., and Emadi, A. (2022). Geometry and topology optimization of switched reluctance machines: A review. *IEEE Access*.
- [Ai-de et al., 2018] Ai-de, X., Xianchao, Z., Kunlun, H., and Yuzhao, C. (2018). Torque-ripple reduction of srm using optimised voltage vector in dtc. *IET Electrical Systems in Transportation*, 8(1):35–43.
- [Bilgin and Emadi, 2014] Bilgin, B. and Emadi, A. (2014). Electric motors in electrified transportation: A step toward achieving a sustainable and highly efficient transportation system. *IEEE Power Electronics Magazine*, 1(2):10–17.
- [Bilgin et al., 2018] Bilgin, B., Jiang, J. W., and Emadi, A. (2018). Switched reluctance motor drives: fundamentals to applications. *Boca Raton, FL*.
- [Bostanci et al., 2017] Bostanci, E., Moallem, M., Parsapour, A., and Fahimi, B. (2017). Opportunities and challenges of switched reluctance motor drives for electric propulsion: A comparative study. *IEEE transactions on transportation electrification*, 3(1):58–75.
- [Chancharoensook and Rahman, 2002] Chancharoensook, P. and Rahman, M. (2002). Dynamic modeling of a four-phase 8/6 switched reluctance motor using current and torque look-up tables. In *IEEE 2002 28th Annual Conference of the Industrial Electronics Society. IECON 02*, volume 1, pages 491–496 vol.1.
- [Cheng et al., 2021] Cheng, H., Mi, S., Wang, Z., Shao, D., Wu, H., Yan, W., and Yu, D. (2021). Phase current reconstruction with dual-sensor for switched reluctance motor drive system. *IEEE Access*, 9:114095–114103.
- [Cheok and Fukuda, 2002] Cheok, A. D. and Fukuda, Y. (2002). A new torque and flux control method for switched reluctance motor drives. *IEEE Transactions on Power Electronics*, 17(4):543–557.



- [Choi et al., 2002] Choi, C., Kim, S., Kim, Y., and Park, K. (2002). A new torque control method of a switched reluctance motor using a torque-sharing function. *IEEE Transactions on Magnetics*, 38(5):3288–3290.
- [Choi et al., 2007] Choi, Y. K., Yoon, H. S., and Koh, C. S. (2007). Pole-shape optimization of a switched-reluctance motor for torque ripple reduction. *IEEE transactions on magnetics*, 43(4):1797–1800.
- [Drofenik and Kolar, 2005] Drofenik, U. and Kolar, J. W. (2005). A general scheme for calculating switching-and conduction-losses of power semiconductors in numerical circuit simulations of power electronic systems. In *Proc. IPEC*, volume 5, pages 4–8. Citeseer.
- [Gan et al., 2020] Gan, C., Chen, Y., Sun, Q., Si, J., Wu, J., and Hu, Y. (2020). A position sensorless torque control strategy for switched reluctance machines with fewer current sensors. *IEEE/ASME Transactions on Mechatronics*, 26(2):1118–1128.
- [Gan et al., 2017] Gan, C., Sun, Q., Jin, N., Tolbert, L. M., Ling, Z., Hu, Y., and Wu, J. (2017). Cost-effective current measurement technique for four-phase srm control by split dual bus line without pulse injection and voltage penalty. *IEEE Transactions on Industrial Electronics*, 65(6):4553–4564.
- [Gan et al., 2018] Gan, C., Sun, Q., Wu, J., Shi, C., and Hu, Y. (2018). A universal two-sensor current detection scheme for current control of multiphase switched reluctance motors with multiphase excitation. *IEEE Transactions on Power Electronics*, 34(2):1526–1539.
- [Gan et al., 2015] Gan, C., Wu, J., Hu, Y., Yang, S., Cao, W., and Kirtley, J. L. (2015). Online sensorless position estimation for switched reluctance motors using one current sensor. *IEEE Transactions on Power Electronics*, 31(10):7248–7263.
- [Gan et al., 2016a] Gan, C., Wu, J., Sun, Q., Yang, S., Hu, Y., and Jin, L. (2016a). Low-cost direct instantaneous torque control for switched reluctance motors with bus current detection under soft-chopping mode. *IET Power Electronics*, 9(3):482–490.
- [Gan et al., 2016b] Gan, C., Wu, J., Wang, N., Hu, Y., Cao, W., and Yang, S. (2016b). Independent current control of dual parallel srm drive using a public current sensor. *IEEE/ASME Transactions on Mechatronics*, 22(1):392–401.

- [Gan et al., 2014] Gan, C., Wu, J., Yang, S., and Hu, Y. (2014). Phase current reconstruction of switched reluctance motors from dc-link current under double high-frequency pulses injection. *IEEE Transactions on Industrial Electronics*, 62(5):3265–3276.
- [Han et al., 2017] Han, G., Chen, H., Shi, X., and Wang, Y. (2017). Phase current reconstruction strategy for switched reluctance machines with fault-tolerant capability. *IET Electric Power Applications*, 11(3):399–411.
- [Husain, 2002] Husain, I. (2002). Minimization of torque ripple in srm drives. *IEEE Transactions on Industrial Electronics*, 49(1):28–39.
- [Husain, 2010] Husain, I. (2010). *Electric and hybrid vehicles: design fundamentals*. CRC press.
- [Husain and Ehsani, 1996] Husain, I. and Ehsani, M. (1996). Torque ripple minimization in switched reluctance motor drives by pwm current control. *IEEE transactions on power electronics*, 11(1):83–88.
- [Inderka and De Doncker, 2003] Inderka, R. B. and De Doncker, R. W. (2003). Dite-direct instantaneous torque control of switched reluctance drives. *IEEE Transactions on Industry Applications*, 39(4):1046–1051.
- [Kjaer and Gallegos-Lopez, 1998] Kjaer, P. C. and Gallegos-Lopez, G. (1998). Single-sensor current regulation in switched reluctance motor drives. *IEEE Transactions on Industry Applications*, 34(3):444–451.
- [Kjaer et al., 1996] Kjaer, P. C., Gribble, J. J., and Miller, T. J. (1996). High-grade control of switched reluctance machines. In *IAS'96. Conference Record of the 1996 IEEE Industry Applications Conference Thirty-First IAS Annual Meeting*, volume 1, pages 92–100. IEEE.
- [Krishnan, 2017] Krishnan, R. (2017). *Switched reluctance motor drives: modeling, simulation, analysis, design, and applications*. CRC press.
- [Le-Huy and Brunelle, 2005] Le-Huy, H. and Brunelle, P. (2005). A versatile nonlinear switched reluctance motor model in simulink using realistic and analytical magnetization characteristics. In *31st Annual Conference of IEEE Industrial Electronics Society, 2005. IECON 2005.*, pages 6 pp.–.
- [Li et al., 2011] Li, G., Ojeda, J., Hlioui, S., Hoang, E., Lecrivain, M., and Gabsi, M. (2011). Modification in rotor pole geometry of mutually coupled

- switched reluctance machine for torque ripple mitigating. *IEEE Transactions on Magnetics*, 48(6):2025–2034.
- [Li et al., 2018] Li, H., Bilgin, B., and Emadi, A. (2018). An improved torque sharing function for torque ripple reduction in switched reluctance machines. *IEEE Transactions on Power Electronics*, 34(2):1635–1644.
- [Mademlis and Kioskeridis, 2003] Mademlis, C. and Kioskeridis, I. (2003). Performance optimization in switched reluctance motor drives with online commutation angle control. *IEEE Transactions on Energy Conversion*, 18(3):448–457.
- [Mikail et al., 2013] Mikail, R., Husain, I., Sozer, Y., Islam, M. S., and Sebastian, T. (2013). Torque-ripple minimization of switched reluctance machines through current profiling. *IEEE Transactions on Industry Applications*, 49(3):1258–1267.
- [Rajesh and Singh, 2014] Rajesh, M. and Singh, B. (2014). Analysis, design and control of single-phase three-level power factor correction rectifier fed switched reluctance motor drive. *IET power Electronics*, 7(6):1499–1508.
- [Ramanarayanan et al., 1996] Ramanarayanan, V., Venkatesha, L., and Panda, D. (1996). Flux-linkage characteristics of switched reluctance motor. In *Proceedings of International Conference on Power Electronics, Drives and Energy Systems for Industrial Growth*, volume 1, pages 281–285 vol.1.
- [Ronanki et al., 2020] Ronanki, D., Dekka, A., and Beig, A. R. (2020). Comprehensive evaluation of phase current reconstruction strategies for four-phase switched reluctance motor drives. In *2020 IEEE Industry Applications Society Annual Meeting*, pages 1–6. IEEE.
- [Ronanki and Williamson, 2017] Ronanki, D. and Williamson, S. S. (2017). Comparative analysis of ditc and dtfc of switched reluctance motor for ev applications. In *2017 IEEE International Conference on Industrial Technology (ICIT)*, pages 509–514. IEEE.
- [Song et al., 2017] Song, S., Xia, Z., Fang, G., Ma, R., and Liu, W. (2017). Phase current reconstruction and control of three-phase switched reluctance machine with modular power converter using single dc-link current sensor. *IEEE Transactions on Power Electronics*, 33(10):8637–8649.

- [Sun et al., 2018] Sun, Q., Wu, J., Gan, C., and Guo, J. (2018). A multiplexed current sensors-based phase current detection scheme for multiphase srms. *IEEE Transactions on Industrial Electronics*, 66(9):6824–6835.
- [Sun et al., 2017] Sun, Q., Wu, J., Gan, C., Hu, Y., Jin, N., and Guo, J. (2017). A new phase current reconstruction scheme for four-phase srm drives using improved converter topology without voltage penalty. *IEEE Transactions on Industrial Electronics*, 65(1):133–144.
- [Sun et al., 2016] Sun, Q., Wu, J., Gan, C., Hu, Y., and Si, J. (2016). Octsf for torque ripple minimisation in srms. *IET Power electronics*, 9(14):2741–2750.
- [Venkataramanaiah and Suresh, 2018] Venkataramanaiah, J. and Suresh, Y. (2018). Performance verification of a new cascaded transformer based multilevel inverter using modified carrier spwm strategy. In *2018 International Conference on Power, Instrumentation, Control and Computing (PICC)*, pages 1–6. IEEE.
- [Vujičić, 2011] Vujičić, V. P. (2011). Minimization of torque ripple and copper losses in switched reluctance drive. *IEEE transactions on power electronics*, 27(1):388–399.
- [Xue et al., 2009] Xue, X., Cheng, K. W. E., and Ho, S. L. (2009). Optimization and evaluation of torque-sharing functions for torque ripple minimization in switched reluctance motor drives. *IEEE transactions on power electronics*, 24(9):2076–2090.
- [Yang et al., 2015] Yang, Z., Shang, F., Brown, I. P., and Krishnamurthy, M. (2015). Comparative study of interior permanent magnet, induction, and switched reluctance motor drives for ev and hev applications. *IEEE Transactions on Transportation Electrification*, 1(3):245–254.
- [Ye et al., 2015] Ye, J., Bilgin, B., and Emadi, A. (2015). An offline torque sharing function for torque ripple reduction in switched reluctance motor drives. *IEEE Transactions on energy conversion*, 30(2):726–735.



## List of Publications Based on Research Work Papers in Refereed Journals

1. **P. Krishna Reddy**, Deepak Ronanki, P. Parthiban, “Direct Torque and Flux Control of Switched Reluctance Motor with Enhanced Torque per Ampere Ratio and Torque Ripple Reduction”, *IET Electronics Letters* (2019), 55 (8):477-478 [SCI], DOI: [10.1049/el.2018.8241](https://doi.org/10.1049/el.2018.8241)
2. **Pittam Krishna Reddy**, Deepak Ronanki, P.Parthiban, “Efficiency Improvement and Torque Ripple Minimisation of Four- Phase Switched Reluctance Motor Drive using New Direct Torque Control Strategy” *IET Electric Power Applications* (2019) , 14 (1): 52-62 [SCI], DOI:[10.1049/iet-epa.2019.0432](https://doi.org/10.1049/iet-epa.2019.0432)
3. Deepak Roanaki, **Pittam Krishna Reddy**, Apparao Dekka, Parthiban Perumal, Abdul R. Beig, “Phase Current Reconstruction With an Improved Direct Torque Control of SRM Drive for Electric Transportation Applications”, *IEEE Transactions on Industry Applications*, (2022), 58 (6): 7648-7657 [SCI], DOI:[10.1109/TIA.2022.3196329](https://doi.org/10.1109/TIA.2022.3196329)

## Book Chapters

1. **Pittam Krishna Reddy**, Parthiban Perumal, Kalpana R ”Motor Drive Selection for EV with Emphasis on Switched Reluctance Motor Drive” for the book titled ” *Power Electronics for Electric Vehicles and Energy Storage: Emerging Technologies and Developments*”, Taylor and Francis, CRC Press.

## Papers in Refereed Conference Proceedings

1. **Pittam Krishna Reddy**, Deepak Ronanki, Parthiban Perumal, and Sheldon S. Williamson. ”New Direct Torque and Flux Control with Improved Torque Per Ampere for Switched Reluctance Motor.” *IEEE International Electric Machines and Drives Conference*

- (*IEMDC*), pp. 1792-1797, IEEE, 2019, DOI: [10.1109/IEMDC.2019.8785327](https://doi.org/10.1109/IEMDC.2019.8785327).
2. **Pittam Krishna Reddy**, Deepak Ronanki, Parthiban Perumal, Abdul R. Beig and Sheldon S. Williamson. “Torque Ripple Minimization of Four-Phase Switched Reluctance Motor Using Direct Torque Control with an Innovative Switching Sequence Scheme.” *IEEE Energy Conversion Congress and Expo (ECCE)*, pp. 1810-1815, IEEE, 2019, DOI: [10.1109/ECCE.2019.8912508](https://doi.org/10.1109/ECCE.2019.8912508).
  3. Apparao Dekka, Deepak Ronanki, **Krishna Reddy Pittam**, Parthiban Perumal and Abdul R. Beig. “Modified Direct Torque and Flux Control of Switched Reluctance Motor Drive with Reduced Source Current Ripple for Vehicular Applications” *IEEE Applied Power Electronics Conference and Exposition (APEC)*, pp. 2920-2925. IEEE, 2020, DOI: [10.1109/APEC39645.2020.9124380](https://doi.org/10.1109/APEC39645.2020.9124380).
  4. Deepak Ronanki, **Krishna Reddy Pittam**, Apparao Dekka, Parthiban Perumal and Abdul R. Beig. “Phase Current Reconstruction Algorithm for Four-Phase Switched Reluctance Motor under Direct Torque Control Strategy” *IEEE Applied Power Electronics Conference and Exposition (APEC)*, pp. 1086-1090. IEEE, 2021, DOI: [10.1109/APEC42165.2021.9487250](https://doi.org/10.1109/APEC42165.2021.9487250).

## Bio-data

Name: Pittam Krishna Reddy

Date of Birth: 12-06-1990

Marital Status: Married

E-mail: krishnareddy248@gmail.com

Mobile: 8328550061

### **Permanent Address**

H.No: 5-337, L.P Road,

Darsi, Prakasam District,

Andhra Pradesh - 523247.

### **Education**

- M.Tech. in Power Electronics (2014)  
Institute: Rajeev Gandhi Memorial college of Engineering & Technology (RGM CET), Nandyal  
University: JNTU Anantapur  
Percentage : 83.38%
- B.Tech. in Electrical and Electronics Engineering (2011)  
Institute: Narayana Engineering College, Nellore  
University: JNTU Anantapur  
Percentage : 79.14%